5-2000

Radiolytic effects on fluoride impurities in a U38

Alan Scott Icenhour

Recommended Citation

Icenhour, Alan Scott, "Radiolytic effects on fluoride impurities in a U38. " PhD diss., University of Tennessee, 2000.
https://trace.tennessee.edu/utk_graddiss/8309

To the Graduate Council:

I am submitting herewith a dissertation written by Alan Scott Icenhour entitled "Radiolytic effects on fluoride impurities in a U_{38}." I have examined the final electronic copy of this dissertation for form and content and recommend that it be accepted in partial fulfillment of the requirements for the degree of Doctor of Philosophy, with a major in Nuclear Engineering.

L. F. Miller, Major Professor

We have read this dissertation and recommend its acceptance:

Peter Groer, Larry Townsend, Herschel Godbee, L. Mac Toth

Accepted for the Council:

Carolyn R. Hodges

Vice Provost and Dean of the Graduate School

(Original signatures are on file with official student records.)

To the Graduate Council:

I am submitting herewith a dissertation written by Alan Scott Icenhour entitled "Radiolytic Effects on Fluoride Impurities in a U_3O_8 Matrix." I have examined the final copy of this dissertation for form and content and recommend that it be accepted in partial fulfillment of the requirements for the degree of Doctor of Philosophy, with a major in Nuclear Engineering.

L F Miller

L. F. Miller, Major Professor

We have read this dissertation
and recommend its acceptance:

LW Townsend

Pete C. Groer

Louis M. Toth

Herschel W. Godbee

Accepted for the Council

C W Minkel

Associate Vice Chancellor and
Dean of The Graduate School

RADIOLYTIC EFFECTS ON FLUORIDE IMPURITIES IN A U_3O_8 MATRIX

A Dissertation
Presented for the
Doctor of Philosophy
Degree
The University of Tennessee, Knoxville

Alan Scott Icenhour
May 2000

DEDICATION

This dissertation is dedicated to my wife, Teresa. You have patiently endured this task with me. I will be forever grateful for your loving support and that you always kept the candle in the window.

ACKNOWLEDGMENTS

I thank my major professor, Dr. Larry Miller, for his guidance in the completion of this dissertation and my Ph.D. degree program. I especially thank Dr. L. Mac Toth, who served as my advisor and mentor at Oak Ridge National Laboratory (ORNL). He has been an invaluable source of advice, knowledge, and encouragement. He is directly responsible for my selection of this challenging dissertation topic. I am also indebted to Dr. Herschel Godbee, who has provided encouragement, advice, and critical review through these many years of my education. I appreciate the helpful review and comments of the other members of my dissertation committee, Dr. Peter Groer and Dr. Larry Townsend.

I thank my colleagues at ORNL: Dr. Bill Del Cul, Dr. David Williams, Darrell Simmons, Dr. Lee Trowbridge, and Jim Travis. They have each provided many helpful discussions, guidance, and support in my laboratory studies. I thank Ralph Sharpe for his insightful and timely editorial review. I especially am grateful to Mary McGarvey for her efforts in preparing this manuscript. Her extraordinary effort made this difficult task possible. I appreciate the support of the Chemical Technology Division at ORNL and the U.S. Department of Energy. I acknowledge also the support and encouragement of Dr. Jim Rushton of ORNL.

Finally, I am profoundly grateful to my family—my wife, Teresa; my daughters, Melissa and Abby; my parents, Joe and Ruby Icenhour; and my parents-in-law, Harold and Rebecca Phillips. They have been a source of continued support. This degree could not have been completed without them, and they each share in the accomplishment. I sincerely appreciate their sacrifices and their abiding support.

ABSTRACT

The safe handling and storage of radioactive materials require an understanding of the effects of radiolysis on those materials. Radiolysis may result in the production of gases (e.g., corrosives) or pressures that are deleterious to storage containers. A study has been performed to address these concerns as they relate to the radiolysis of residual fluoride compounds in uranium oxides. The interactions of radiation with crystalline solids, based on the bonding characteristics of the crystal, were described. Samples of $UO_2F_2 \cdot xH_2O$ and U_3O_8 (with ~1.4 wt % fluorine content) were irradiated in a ^{60}Co source and in spent nuclear fuel (SNF) elements from the High Flux Isotope Reactor (HFIR) at Oak Ridge National Laboratory. Container pressures were monitored throughout the irradiations, and gas and solid samples were analyzed after the irradiations. The irradiation of $UO_2F_2 \cdot xH_2O$ produced O_2—with $G(O_2)$-values ranging from 0.007 to 0.03 molecules O_2 produced per 100 eV. Neither F_2 nor HF was produced by the irradiations. Chemical analysis of solid samples showed that some of the uranium was reduced from U(VI) to U(IV). A saturation damage limit for the $UO_2F_2 \cdot xH_2O$ was demonstrated by using the HFIR SNF elements, and the limit was found to be 7–9% (at ~10^8 rad/h). It is shown that the covalently bonded oxygen is more susceptible to radiation damage than is the ionically bonded fluorine. Irradiation of U_3O_8 (with ~1.4 wt % fluorine content) resulted in neither gas production nor a pressure increase. These experiments led to the conclusion that U_3O_8 is safe during long-term storage from overpressurization and the production of corrosives caused by gamma radiolysis of residual fluorides.

CONTENTS

LIST OF TABLES

LIST OF FIGURES

LIST OF SYMBOLS

A = absorbance (unitless)

A_{uc} = relative unit-cell expansion at saturation (unitless)

B_{uc} = rate constant for simultaneous recombination of defects during irradiation (Gy^{-1})

c = concentration (M)

C = amount of oxygen absorbed [cm^3 (at STP)/g]

$CF(t)$ = correction factor at time t after shutdown (unitless)

d = distance between each set of atomic planes (cm)

D = dose (Gy)

$D(t)$ = integrated dose at time t (Gy)

$\dot{D}_o$ = initial dose rate (Gy/h)

$\dot{D}(t)$ = dose rate at time t (Gy/h)

$\dot{D}_y$ = dose rate in material y (Gy/h)

ϵ = molar absorbtivity ($M^{-1}\mathrm{cm}^{-1}$)

E_B = bonding energy of the core or valence electron (eV)

E_d = threshold displacement energy (eV)

E_k = photoelectron kinetic energy (eV)

G(gas) = number of molecules of gas produced per 100 eV deposited in the material being irradiated

$h\nu$ = photon energy (eV)

l = light path length (cm)

λ = decay constant (d^{-1})

λ_1 = wavelength (cm)

m = mass of sample (g)

μ = attenuation coefficient (cm^{-1})

μ_{en}/ρ = mass energy absorption coefficient (m^2/kg)

n = order of diffraction (integer $n = 1, 2, \ldots$)

Δn = gas yield (mmoles gas/g sample)

$\Delta\,(O/M)$ = change in oxygen-to-metal ratio (unitless)

ΔP = change in pressure (Torr)

ϕ = system dependent, adjustable factor (eV)

R = gas constant = 0.08205 atm-L/mol-K

T = time of operation at 85 MW (d)

t = time (d)

T_c = temperature in container (K)

θ = diffraction angle (degrees)

V_o = initial volume of unit cell (cm^3)

V_{void} = void volume of sample container (L)

$\Delta\,V_{uc}$ = change in volume of unit cell (cm^3)

w_i = proportion by weight of the *i*th element (unitless)

$\dot{X}$ = exposure rate (R/h)

LIST OF ABBREVIATIONS, ACRONYMS, AND INITIALISMS

ASTM	American Society for Testing and Materials
ATR	attenuated total reflectance
BWR	boiling water reactor
CANDU	Canadian Deuterium uranium
DOE	U.S. Department of Energy
DTA	differential thermal analysis
DU	depleted uranium
ESCA	electron spectroscopy for chemical analysis
ETTP	East Tennessee Technology Park
FTIR	Fourier transform infrared
HFIR	High Flux Isotope Reactor
HLW	high-level waste
LANL	Los Alamos National Laboratory
LLW	low-level waste
MS	mass spectrometry
MSRE	Molten Salt Reactor Experiment
n_f	fast neutron
ORNL	Oak Ridge National Laboratory
PWR	pressurized water reactor

SEM	scanning electron microscopy
SNF	spent nuclear fuel
XPS	X-ray photon spectroscopy
XRD	X-ray diffraction
TGA	thermogravimetric analysis

1. INTRODUCTION

The radiolysis of various materials by different radiation sources (e.g., alpha, beta, gamma, and neutron) has been the subject of extensive investigations. Often, the purpose of these investigations is to provide an understanding of the radiolytic products and concomitant effects of radiolysis in a specific system. The source of the radiative energy can be either internal (e.g., self-irradiation) or external (e.g., material exposed to a source or surrounded by radioactive materials). Examples of systems that have been studied include: radioactive wastes [e.g., low-level waste (LLW) and high-level waste (HLW)], spent nuclear fuel (SNF), mixed wastes (e.g., mixed LLW), and stored radioactive materials [e.g., uranium oxides, plutonium oxides, and uranium hexafluoride (UF_6)]. Examples of possible effects include (a) swelling of oxide samples resulting from radiation-induced defects in the crystalline lattice; (b) radiolytic degradation of water, organics, or inorganics; (c) production of gases—resulting in pressure increases with subsequent container failure; (d) production of flammable or explosive concentrations of gases (e.g., H_2); and (e) production of corrosive products [e.g., fluorine (F_2) and hydrogen fluoride (HF)]. The specific effect in a given system is dependent upon many factors including: the type of radioactive decay and associated decay energy, the composition of the systems (i.e., the composition of the material undergoing radiolysis and the container), competing reactions for radiolytic products (e.g., recombination of products), and the total dose (and dose rate) delivered to a material.

The February 1993 U.S. Department of Energy (DOE) Office of Nuclear Safety "Safety Notice" provides a summary of accidents associated with waste drums and containers. This notice reports that "eight incidents of fire, explosion, and drum overpressurization occurred at DOE facilities from 1970 through 1985." In addition, eight incidents of this type occurred at DOE facilities from January 1991 to September 1992. Hydrogen and other gases were identified as major contributors to these accidents (DOE 1993). Gas generation in the infamous, burping HLW tank (101-SY) at Hanford is attributed to chemical reactions (~60 vol % of gas) and radiolysis (~40 vol % gas). The radiolytic production of F_2 in cylinders containing highly-enriched UF_6 has resulted in overpressurization of these cylinders (Saraceno 1988).

Because of these and other observed effects, much research has been dedicated to understanding and predicting the results of radiolytic damage occurring in stored materials. Recently, work has focused on radioactive wastes, mixed wastes, and SNF because of both the large volume of these wastes and the need to dispose of them safely.

Radiolysis is a concern also with respect to the remediation project for the Molten Salt Reactor Experiment (MSRE) at the Oak Ridge National Laboratory (ORNL). Radiolytically produced F_2 from the fluoride salt (LiF-BeF_2-ZrF_4-UF_4) resulted in the production of UF_6, which migrated throughout reactor piping systems (National Research Council 1997) . The discovery of this situation led to an extensive effort to remove the ^{233}U from the reactor. The removed ^{233}U will be converted to U_3O_8 and will be placed in long-term storage. The isotope ^{232}U, which usually occurs in 50–300 ppm concentrations in ^{233}U, causes a large radiation field (Fig. 1.1) which, in turn, can cause radiolysis of the

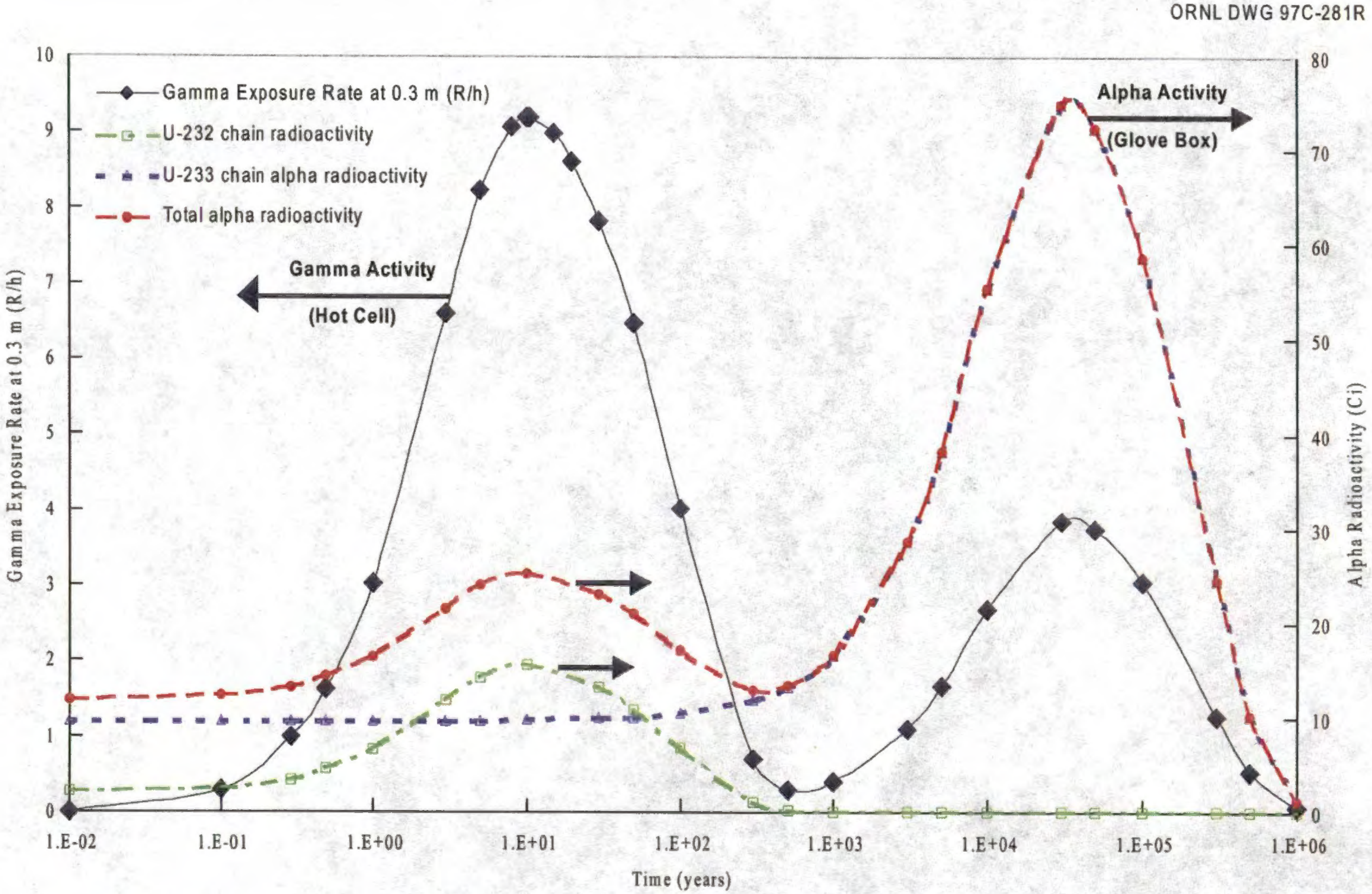

Fig. 1.1. Alpha activity and gamma exposure rate at a distance of 0.3 m as a function of time as calculated for 1 kg ^{233}U (with 100 ppm ^{232}U) as a loose powder (1.5 g/cm^3) contained in a 7.62-cm-diam by 15.24-cm-tall can with 0.051-cm-thick steel walls. [Forsberg, C. W., A. S. Icenhour, E. L. Youngblood, and A. M. Krichinsky, November 26, 1997. *Strategy for the Future Use and Disposition of Uranium-233: Disposition Options*, ORNL/MD/LTR-63, Lockheed Martin Energy Research Corp., Oak Ridge National Laboratory, Oak Ridge Tennessee, (draft).]

uranium-oxide matrix and other impurity components—e.g., fluoride as UO_2F_2 and water—that may be present.*

Specific concerns regarding the radiolysis of residual fluorides (or oxyfluorides) in U_3O_8 are (a) formation of F_2, resulting in overpressurization of containers; (b) formation of HF (in the presence of water), resulting in chemical attack of the container materials; (c) fluorination of the uranium oxide, producing mobile UF_6 inside the container (similar to the phenomenon which occurred at the MSRE); and (d) formation of other gaseous compounds, such as O_2.

Clearly, the effects that occur in a specific system are dependent upon many factors. In addition, depending on the types and amounts of other impurities present (e.g., water), other radiolytic reactions could occur (e.g., production of H_2). Consequently, it is necessary to establish a limit for residual fluoride impurities in the $^{233}U_3O_8$ (Del Cul, Icenhour, and Toth 1997). Furthermore, depleted uranium (DU) from the nation's stockpile may be converted to U_3O_8 and used as a backfill for SNF packages (Forsberg 1996). Hence, because this material would be placed in the radiation field of the SNF,

---

* Uranium-233 is more difficult to handle than ^{235}U, because an inherent characteristic of ^{233}U is that it also contains some ^{232}U. Uranium-233 containing tens to hundreds of ppm of ^{232}U requires heavy radiation shielding and remote-handling operations to protect workers from gamma radiation (Forsberg et al. 1997). Uranium-232 has a daughter, ^{208}Tl, which emits a 2.6-MeV gamma-ray. The current ^{232}U concentration in the MSRE ^{233}U is about 160 ppm; hence, conversion and handling of the MSRE materials will necessarily be performed in a hot cell.

The hazards associated with ^{233}U are illustrated in Fig. 1.1, which gives the alpha activity and gamma exposure rate for 1 kg ^{233}U (with 100 ppm ^{232}U) that is packaged as a loose powder contained in a 7.62-cm (3-in.)-diam, 15.24-cm (6-in.)-tall can, with 0.051-cm (20-mil)-thick steel walls. The first set of peaks are associated with the buildup and decrease of ^{232}U decay products. The second set of peaks results from the buildup and decrease of ^{233}U decay products (Forsberg et al. 1997). From the figure, it is evident that this material has a significant gamma radiation field and alpha activity. These characteristics can result in radiolytic effects on either the material itself or on surrounding materials.

the radiolytic effects on fluoride impurities in the DU oxide must also be understood (Forsberg 1997).

Specifications exist for the fluoride content in uranium oxides, enriched in ^{235}U, that are to be used in light water reactors. However, there are no similar specifications for ^{233}U-oxides or DU-oxides. For example, for reactor-grade, sinterable UO_2 powder, the specification for fluorine impurities is 100 ppm of the total uranium [American Society for Testing and Materials (ASTM) C753–94 1994]. For sintered UO_2 pellets, the specification for residual fluorine is 15 ppm of the total uranium (ASTM C776–94 1994). These specifications are for nuclear fuel and are not, therefore, directly applicable to the converted U_3O_8 (containing either ^{233}U or DU) that is intended only for storage. Furthermore, these specifications are driven by neutronics considerations for in-core irradiation of fuels (Cagle 1997). No plans exist to use the U_3O_8 resulting from the MSRE remediation as reactor fuel; as a result, this material may not need these high levels of purity. Consequently, the residual fluoride content must be established only on the basis of requirements for long-term storage. There is therefore a need to establish a standard for residual fluoride levels in uranium oxides under these storage conditions.

Recent efforts at ORNL and at other national laboratories have been directed toward establishing safe storage standards for plutonium and ^{233}U. Radiolysis studies are being conducted to provide a technical basis for the limits imposed on the storage of plutonium oxides (Mason et al. 1999). The work presented herein provides a similar study for uranium oxides.

The objective of this work was to evaluate radiolytic effects on uranium oxides and, in particular, on the fluoride impurities in uranium oxides. Also of interest was the observation of any deleterious effects of radiolytic products on containers used in the experimental studies. The work was focused on two primary areas: (1) literature review and evaluation and (2) radiolysis experiments. A literature search was conducted to provide a general understanding of the interaction of radiation with crystalline solids and oxides. Additionally, because uranium oxides are a major constituent of the heterogeneous systems being studied, the literature on the effects of radiation on uranium oxides was evaluated as well.

To evaluate the radiolytic effects on fluoride impurities in uranium oxides, laboratory experiments were performed. Uranyl fluoride ($UO_2F_2 \bullet xH_2O$), an intermediate compound produced during the conversion of UF_6 to U_3O_8 and the likely form of the residual fluorides, was irradiated with gamma sources. Furthermore, this compound represents the maximum fluoride content that could be present after the conversion process, and, consequently, it should give the maximum radiolytic yield. Also irradiated were samples of U_3O_8 that were prepared by the conversion process. These materials contained low fluoride concentrations like those expected as a result of converting UF_6 from the MSRE to U_3O_8.

Uranyl fluoride can form hydrates, as indicated by the formula $UO_2F_2 \bullet xH_2O$. The value of x varies from about 0.4 to 2.3. Of course, $x = 0$ for anhydrous UO_2F_2. Throughout this report, uranyl fluoride is referred to as $UO_2F_2 \bullet xH_2O$, unless a specific hydrate is being addressed. It should also be pointed out that the converted U_3O_8 often contains other uranium oxide phases, although it is predominately U_3O_8. Hence, throughout this report, this material will be described simply as U_3O_8.

Two sources of gamma radiation were used in the experiments: (a) the ORNL ^{60}Co source, which has dose rates of about 10^5 rad/h and (b) a High Flux Isotope Reactor (HFIR) SNF element, which has dose rates that range from 10^7 to 10^8 rad/h (depending on the time since element discharge from the reactor). Integrated doses using the ^{60}Co source were about 2×10^8 rad, while the integrated doses using HFIR SNF elements were up to 6×10^{10} rad.

During irradiations, pressures in sample containers were monitored and recorded. After irradiation, gas samples were withdrawn from the containers and analyzed for composition. Additionally, solid samples of the irradiated material were analyzed by several techniques to evaluate radiolytic effects on the solids.

One of the most important outcomes from this work is hoped to be the establishment of a standard for residual fluoride content in a U_3O_8 matrix for long-term storage. Currently, the only fluoride-content standards are for nuclear-reactor-grade materials, and these concentrations are stringently low. However, because the materials from the MSRE will not need to meet reactor-grade specifications, the fluoride-content specification should only be set low enough such as to ensure safe, long-term storage.

It should be stressed that the establishment of a fluoride limit in U_3O_8 is not a problem that is unique to the MSRE materials. It has been proposed to use DU oxide as a fill material for SNF canisters, which will be disposed of in a repository (Forsberg 1996).

This oxide will be exposed to high radiation fields from the SNF; consequently, our increased understanding of the radiolytic effects on residual fluorides will be important.

The results from this work will lead to (a) identification of radiolytic products, (b) identification of deleterious effects on both the U_3O_8 matrix and container materials, and (c) establishment of a fluoride concentration limit for long-term storage of U_3O_8. These types of information are not currently available in the literature and are needed to support a current DOE program.

A description of the content of each of the sections in this report is outlined in the following paragraphs. In Sect. 2, background information on the effects of radiation on crystalline solids is provided. First, the crystal structures of uranium compounds that are either used in the irradiation experiments or that may be placed into long-term storage are described. Next, the interaction of different types of radiation with crystalline solids and the subsequent effects on the crystal lattice are described. Radiation effects on crystals with respect to bonding characteristic (i.e., covalent, ionic, or mixed ionic-covalent) are then discussed. This is followed by the description of the effects of radiation on several oxide compounds. Finally, the discussion focuses on the effects of radiation on uranium oxides, because these are the materials that will be placed into long-term storage. The uranium oxide discussion is divided into two categories: oxidation and structural changes.

In Sect. 3, the irradiation experiments that were performed are described. Samples of $UO_2F_2 \cdot xH_2O$ and U_3O_8 (with a known residual fluoride content) were irradiated using the ORNL ^{60}Co source and HFIR SNF elements. The irradiation facilities, sample containers, data acquisition systems, preparation of the materials to be irradiated, and analyses performed for gas and solid samples are discussed.

In Sect. 4, the results of the gamma irradiation experiments are presented. The pressures, as a function of time, for each sample are provided, and these data are used to derive G-values for each of the samples. The *G(gas)-value* is defined as the number of molecules of gas produced (or destroyed) per 100 eV of energy deposited. Gas analyses provide the composition of the gas for each sample. Results from solids analyses provide information on the effects of gamma radiation on the samples.

In Sect. 5, the results from the gamma irradiation experiments are discussed. First, results from each of the individual analyses are discussed (e.g., pressure monitoring, gas and solids analyses) to provide insight into specific mechanisms that may be occurring during irradiation. Then these discussions are summarized to provide a clearer overall picture regarding the radiolysis of $UO_2F_2 \bullet xH_2O$ and residual fluoride compounds in U_3O_8.

In Sect. 6, conclusions regarding this study and recommendations for further work are presented.

Supplemental information is discussed in the appendixes. Because of the close relationship of this work to the MSRE remediation project, further background information is provided in Appendixes A and B. Appendix A gives a brief history of the MSRE project, while Appendix B contains a description of the process that will be used to convert the uranium removed from the MSRE to uranium oxide. The information in Appendixes A and B is based primarily on descriptions presented in the National

Research Council (1997) report, and in Del Cul, Icenhour, and Toth (1997). Appendix C provides a description of the method used to estimate absorbed dose from exposure data. Finally, in Appendix D, results from infrared analyses of both gas and solid samples are given.

2. BACKGROUND

In this section, background information is provided on the materials to be irradiated and the effects of radiation on crystalline solids, in particular, oxides. First, in Sect 2.1 the crystal structures of UO_2F_2 and various uranium oxides (i.e., UO_2, U_3O_8, and UO_3) are described. The effects of radiation often alter structure and are monitored through structural analysis. Uranyl fluoride is an intermediate compound, which is formed during the conversion of UF_6 to U_3O_8 (Appendix B), and it is used in the majority of the irradiation experiments reported in this study. Uranium oxides placed in storage are likely to be in the form of UO_2 or U_3O_8. However, some UO_3 is also in storage at ORNL. In Sect. 2.2 the interactions of different types of radiation with solids are discussed, and an overview of the effects of radiation on crystalline solids is presented. Then, in Sect. 2.3 a further division of the effects of radiation on crystals with respect to bonding characteristics of the crystal (i.e., covalent, ionic, and mixed ionic-covalent) is provided. Finally, the effects of radiation on oxides and, in particular, uranium oxides are described in Sect. 2.4.

2.1 CRYSTAL STRUCTURES OF SELECTED URANIUM COMPOUNDS

In the following subsections, the crystal structures are presented for UO_2F_2, UO_2, U_3O_8, and UO_3. These structures are provided to give insight into the types of radiation effects that might be produced in these materials. Such effects are described in later subsections.

2.1.1 UO_2F_2

The structure of anhydrous UO_2F_2 was first reported by Zachariasen (1948). Measurements of lattice parameters were further refined by the neutron powder-diffraction studies of Atoji and McDermott (1970). Taylor (1976) summarized the reported studies of the anhydrous UO_2F_2 crystal structure, and he provided the structure shown in Fig. 2.1. The UO_2F_2 structure consists of a stack of identical, hexagonal layers (Zachariasen 1948). The uranyl ions (UO_2^{2+}) are normal to the layer with the double-bonded oxygens above and below each plane. Six fluorine atoms surround each uranyl ion in its equatorial plane. The U–O distances are 1.71 Å, and the U–F distances are 2.429 Å (Taylor 1976). The equatorial fluorine hexagon is slightly puckered, with the fluorine atoms alternatively located 0.21 Å above and below the plane formed by the uranium atoms (Taylor 1976, Atoji and McDermott 1970). The next layer above the one displayed in Fig. 2.1 is horizontally displaced by the vector A, which is indicated in the structure, because of the location of the oxygens in the uranyl groups (i.e., perpendicular to the layer). The cohesive force between adjacent layers is the result of O-O and O-F attractions between the layers. The O-O and O-F bonds exist because oxygen and fluorine atoms are strongly polarized by one-sided binding to uranium atoms (Zachariasen 1948).

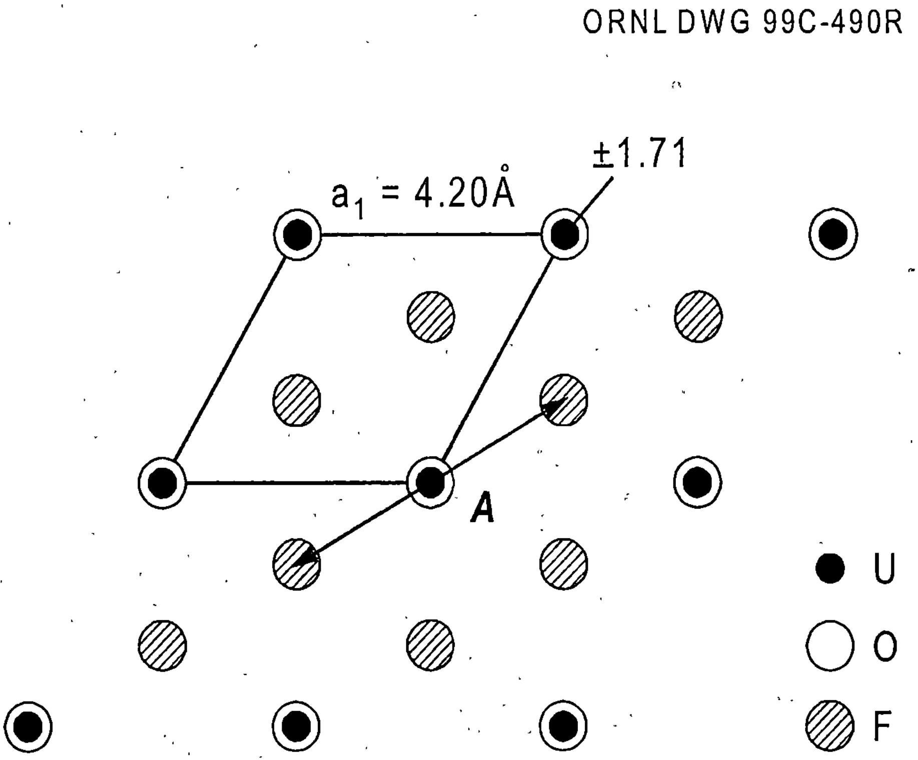

Fig. 2.1. Crystal structure of anhydrous UO_2F_2 [after Taylor (1976)].

UO_2F_2 can be characterized as having mixed bonding, because it contains both covalent and ionic bonds. The oxygens are covalently bonded to the uranium, forming the UO_2^{2+} ion. The UO_2^{2+} and F^- ions are ionically bonded.

2.1.2 UO_2

The UO_2 unit cell is the face-centered cubic fluorite structure (Fig. 2.2). The uranium atoms occupy the positions (0 0 0), (½ ½ 0), (½ 0 ½), and (0 ½ ½). The oxygen atoms are located in the (¼ ¼ ¼) positions (Katz 1986).

2.1.3 U_3O_8

Katz (1986) reports two forms for U_3O_8 —α-U_3O_8 and β-U_3O_8. Both forms are orthorhombic (Fig. 2.3). The U(1) atoms [located at (0 0 0) and (½ ½ ½)] are surrounded by six oxygens, while the U(2) atoms [located at ± (0, 0.315, 0) and body centered] are surrounded by seven oxygens. (Wyckoff 1964, Pearson 1958).

2.1.4 UO_3

Katz (1986) reports that there are one amorphous and six crystalline modifications of UO_3, depending on the conditions of preparation. However, only one of the modifications, γ-UO_3, is stable at atmospheric pressure. The structure of γ-UO_3 is orthorhombic. All of the crystalline modifications contain two short, collinear primary uranium-oxygen (i.e., uranyl-type) bonds, with weaker bonds to other oxygens in a plane that is perpendicular to the primary bonds.

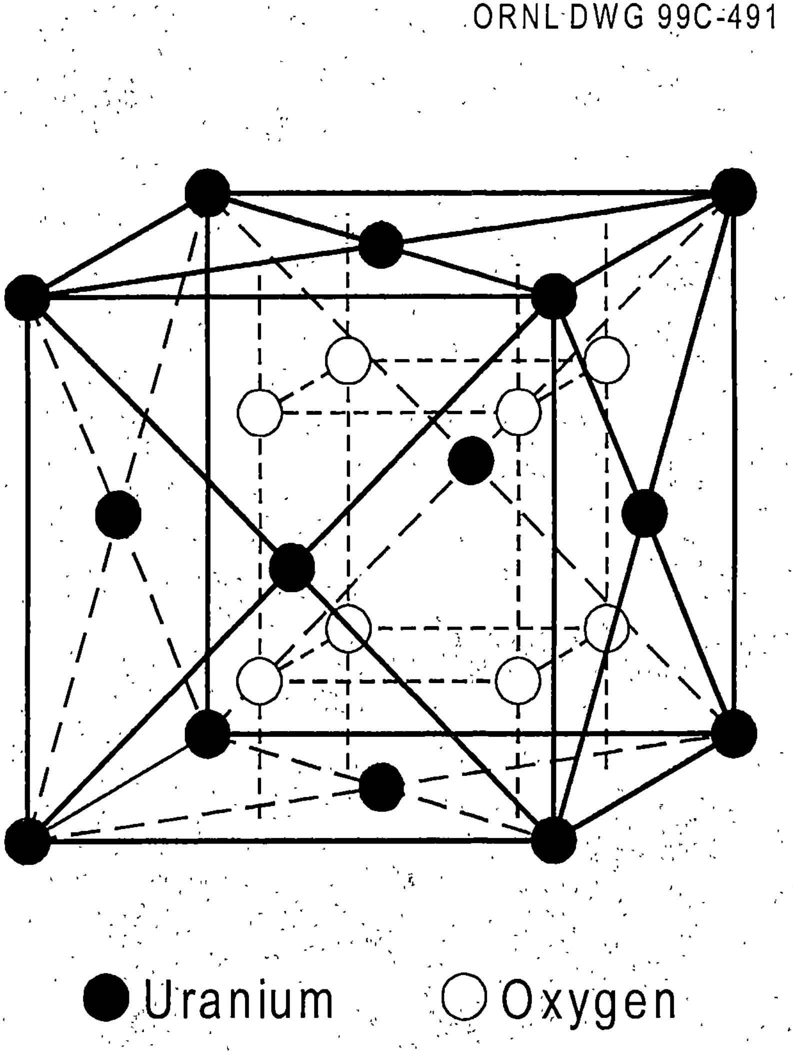

Fig. 2.2. Crystal structure of UO_2 (Katz 1986).

ORNL DWG 99C-6903

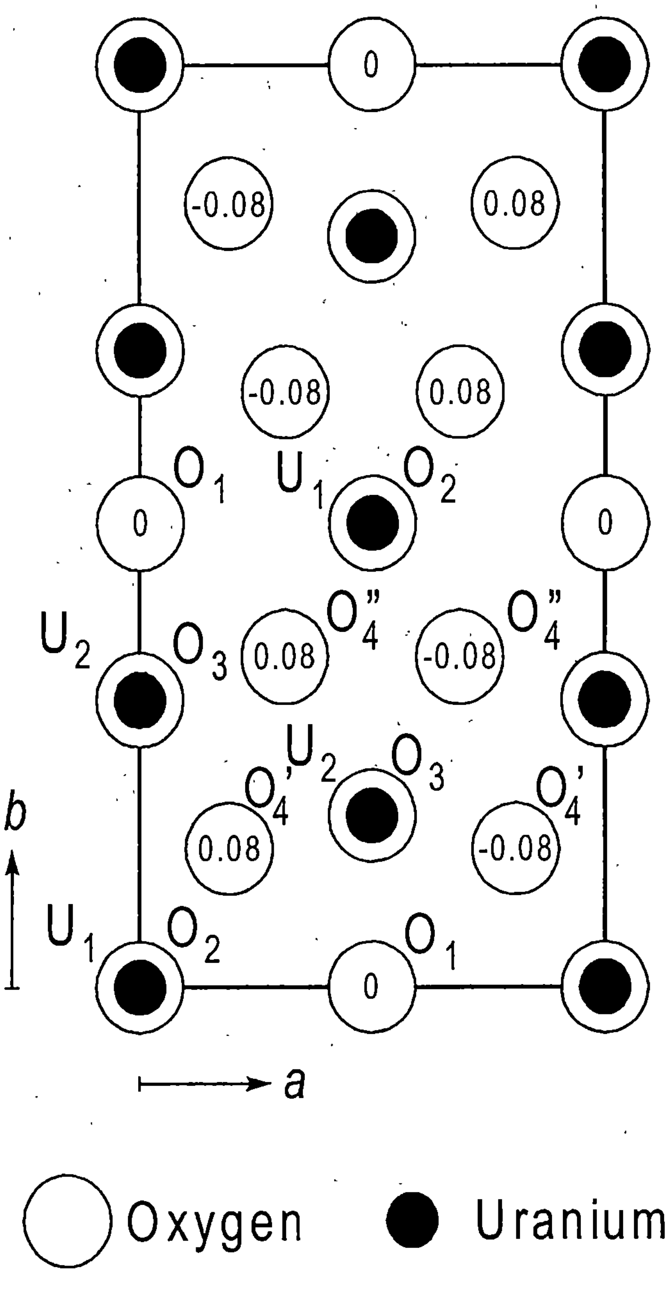

Fig. 2.3. **Crystal structure of U_3O_8 (c-axis projection)** (Pearson 1958).

Uranium trioxide also forms hydrates, that is, $UO_3 \cdot xH_2O$ (with $x = 0.5, 0.8, 1, 2$). The molecular structure of the hydrate, as presented in Fig. 2.4, consists of uranyl ions that are connected in linear chains through hydroxyls. Water molecules are held in the voids of the solid phase. (Baran 1993).

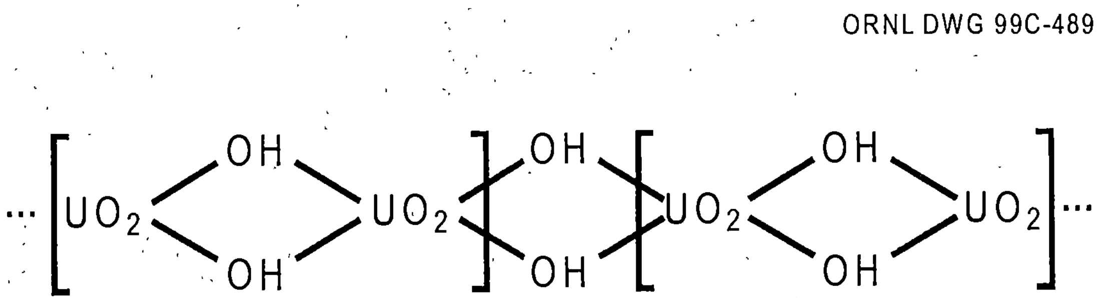

Fig. 2.4. Molecular structure of hydrated UO_3 (Baran 1993).

2.2 INTERACTION OF RADIATION WITH CRYSTALLINE SOLIDS

Gittus (1978) provides an overview of the ways in which various types of radiation (i.e., photons, electrons, heavy ions, and neutrons) interact with crystalline solids. The focus of the discussion is primarily on the displacement of an atom from its lattice site by radiation. Such displacement requires a certain threshold energy, E_d. The value of the E_d is typically 20–60 eV (Weber 1998). Depending (a) upon the radiation type and energy and (b) upon the characteristics of the solid target, the radiation may cause ionization or displacement of atoms in the solid. Such effects can, in turn, cause radiochemical reactions or damage to the crystal matrix.

The interaction of radiation with solids can be grouped into two categories: (a) transfer of energy to electrons (through ionization and electronic excitation) and (b) transfer of energy to nuclei (by elastic collisions). For alpha, beta, and gamma irradiation, the energy transfer is primarily by ionization processes. Alpha-recoil nuclei and neutrons transfer energy through elastic collisions (Weber et al. 1998).

In Sects. 2.2.1–2.2.4, the interactions of photons, electrons, heavy ions, and neutrons with matter are described, respectively. The effects of these interactions on crystalline solids are then discussed in Sect. 2.2.5.

2.2.1 Photon Interactions

Billington and Crawford (1961) list five ways by which photons may transfer energy to a lattice, thus resulting in displacement of atoms: (1) direct displacement of an atom by a Compton interaction with a nucleus, (2) a photonuclear reaction, (3) indirect displacement caused by interaction with photoelectrons, (4) indirect displacement caused by interaction with Compton electrons, and (5) indirect displacement caused by the interaction with components of pair production (i.e., electrons or positrons). Billington and Crawford (1961) dismiss the first two direct processes as being insignificant contributors to atom displacement, stating that the three indirect processes are the most important. Each of the indirect processes—photoelectric effect, Compton scattering, and pair production—result in the production of electrons (and positrons in the case of pair production), which, in turn, may be energetic enough to displace atoms.

For the photoelectric effect, an incident photon causes the ejection of an electron (i.e., the photoelectron) from the irradiated material. The energy of the photoelectron is equal to the photon energy minus the energy expended in removing the electron from the material. For the Compton effect, an incident photon transfers part of its energy to an electron (the Compton electron), resulting in a scattered, lower-energy photon. Finally, for pair production, a photon with energy ≥1.02 MeV (i.e., twice the electron rest mass energy) can be converted to an electron-positron pair in the field of an atomic nucleus. Electrons and positrons will annihilate, producing two photons, each with energy equal to 0.511 MeV plus the kinetic energy of the particles (Turner 1986).

2.2.2 Electron Interactions

Interactions of electrons with atoms are Coulombic in nature. Energy transfer occurs as a result of the electrostatic forces between the electron and either the electrons or the nuclei of the atom (Gittus 1978). Electrons can be the primary source of radiation (e.g., from beta decay or electron bombardment) or a result of interactions of photons with materials (e.g., from the photoelectric effect, Compton scattering, or pair production).

2.2.3 Heavy-Ion Interactions

A heavy ion (e.g., alpha particle, proton, deuteron) can interact with solids by ionizing atoms in the solid, by undergoing further ionization itself, or by particle-nuclei interactions (Gittus 1978). The latter effect, of course, can result in atomic displacements. Similar to electrons, the interaction (and, hence, energy transfer) between the heavy ion and a nucleus is the result of Coulombic repulsion (Billington and Crawford 1961).

2.2.4 Neutron Interactions

Elastic collisions between neutrons and atoms result in energy transfer and may displace the atom from its lattice site. The displaced atom is termed a *primary knock-on* and, if provided enough energy, may cause additional displacements of other atoms. This sequence of displacements can continue until the energy of the displaced atoms no longer exceeds the threshold energy for displacement. The damage caused by such interactions is called a *displacement cascade* (Gittus 1978).

Gittus (1978) lists two other processes by which neutron interactions may cause atom displacement: fission and neutron-gamma (n, γ) reactions. Of course, for the first process to occur, nuclei capable of undergoing fission (e.g., ^{233}U, ^{235}U, and ^{239}Pu) must be present in the solid. Upon fission, the nucleus splits into two energetic fragments which can each cause a large number of displacements. A nucleus that absorbs a neutron may subsequently release energy by emitting a gamma ray [i.e., an (n, γ) reaction]. The recoil of the atom upon emission of the photon may, in turn, cause displacements.

2.2.5 Radiation Effects on Crystalline Solids

Weber et al. (1998) reviewed the literature on radiation effects on crystalline ceramics in the context of immobilization and stabilization of HLW and plutonium for disposal. The review provides a description of types of interactions that occur and the major effects on the crystals that are observed. Weber et al. (1998) describe four major effects of radiation on crystalline materials: amorphization, enhanced diffusion, volume changes, and stored energy.

2.2.5.1 Amorphization

Irradiation damage may result in a crystalline-to-amorphous transformation (i.e., the crystal structure is destroyed or becomes microcrystalline). Materials with the fluorite-related structure (e.g., UO_2 and PuO_2) are not susceptible to radiation-induced amorphization (Weber et al. 1998, Belle 1961). Once formed, the amorphous state is stable under further irradiation. A good example of the crystalline-to-amorphous transformation phenomena is the amorphization of uranium- or thorium-containing minerals by alpha decay. This transformation is referred to as *metamictization* of the minerals (see Sect. 2.4.2.2). Weber et al. (1998) point out that studies of metamictization can provide information on radiation effects on certain materials over geologic time periods. Such information is important for studying the disposal of HLW and plutonium, as well as for understanding effects of radiation on other crystalline materials.

2.2.5.2 Enhanced Diffusion

Irradiation of crystals can result in increased ionic diffusion. Examples include cation diffusion, which is enhanced in UO_2 and mixed oxide fuels by reactor irradiation. Additionally, the activation energy for diffusion of iron in crystalline Al_2O_3 is higher than that in amorphous Al_2O_3, indicating enhanced diffusion in the amorphous material. In general, ionization-induced diffusion improves radiation resistance by enhancing point-defect recombination (Weber et al. 1998). Thus, this improved resistance ultimately results in a saturation damage to the crystal.

2.2.5.3 Volume Changes

Irradiation of crystalline materials can result in volume changes (usually an increase) caused by accumulation of point defects, phase transformations, and the production of microstructural defects such as gas bubbles, voids, and microcracks. The expansion of the crystalline unit cell is a function of the dose and the amount of recombination of defects. These factors determine the saturation defect concentration, and hence, the volume change that is reached. Weber et al. (1998) provide a mathematical expression that describes the volume change and the approach to saturation radiation damage in the unit cell:

$$\frac{\Delta V_{UC}}{V_0} = A_{UC}\left[1 - e^{-B_{UC}D}\right], \tag{2.1}$$

where

ΔV_{UC} = change in volume of unit cell,

V_0 = initial volume of unit cell,

A_{UC} = relative unit-cell expansion at saturation,

B_{UC} = rate constant for simultaneous recombination of defects during irradiation, and

D = dose.

Macroscopic swelling occurs as a result of unit cell volume changes, amorphization of the solid, and the formation of microstructural defects (e.g., gas bubbles and voids). This swelling is often measured by changes in density of the irradiated material. Similar to unit cell volume changes, macroscopic swelling caused by irradiation has been shown to reach saturation in ceramics (Weber 1998).

2.2.5.4 Stored Energy

Radiation damage effectively stores energy in a crystalline solid until the fully amorphous state (i.e., saturation) is reached (Weber 1998). Such energy may be located in (a) point defects in the crystal, (b) the atomic disorder associated with amorphization, and (c) strains induced in the crystal. These defects and structural changes are metastable, and radiation-damaged materials will react (e.g., upon heating) to release the stored energy as the material recrystallizes.

2.3 EFFECT OF RADIATION ON CRYSTALS WITH RESPECT TO BONDING CHARACTERISTICS

The effect of radiation on materials can be considered with respect to the material characteristics themselves: liquids and solids, organics and inorganics, homogeneous and heterogeneous, crystalline and amorphous, and type of bonding (e.g., covalent, ionic, and mixed ionic-covalent). In the context of the study undertaken for this work, it is expedient to focus on the bonding characteristics of the materials used in the irradiation experiments—namely UO_2F_2 and uranium oxides. The former consists of uranyl ions (UO_2^{+2}) and F^- ions (see Sect. 2.1.1). Consequently, this crystalline compound has both covalent and ionic characteristics. In the following subsections, the effects of radiation are broadly described for (a) covalent crystals, (b) ionic crystals, and (c) crystals containing both covalent and ionic bonds (i.e., crystals with mixed bonding).

Covalent crystals consist of a network of covalent bonds that extend throughout the solid. Ionic crystals consist of ions located at lattice sites, and the bonding between the ions is primarily electrostatic. (Brady and Humiston 1982).

The descriptions provided in Sects. 2.3.1 and 2.3.2 for covalent crystals and ionic crystals, respectively, are classical divisions of these types of solids, and are based largely on the text by Billington and Crawford (1961). Irradiation of crystals with mixed bonding is discussed in Sect. 2.3.3. A summary of the effects of radiation on ionic, covalent, and mixed-bonding crystals is provided in Sect. 2.3.4.

2.3.1 Covalent Crystals

Covalent crystals include valence crystals (i.e., each atom or unit is bound to every other atom or unit by a network of covalent bonds, e.g., diamond), many carbides, borides, nitrides, silicates, and oxides. Also included are organic molecular crystals and semicrystalline polymers.

For materials with this sort of bonding, Billington and Crawford (1961) primarily discussed irradiation experiments that had been performed on diamond, quartz, and fused silica. Different sources of radiation have been used in the study of these materials, and irradiation has been shown to result in changes in density, in the production of magnetic defects, and in changes in optical absorption spectra. In some cases, the damage to the crystalline structure is so extensive that the structure is destroyed or becomes microcrystalline. In either case, the material becomes glass-like because structure can not be detected. The description of radiation effects provided by Billington and Crawford (1961) on covalent crystals is summarized in the following paragraphs.

Two basic types of structural defects are present in a crystal: point defects and dislocations. Point defects are vacancies, interstitial atoms, or impurity atoms that perturb the lattice for several lattice distances. A dislocation is a line irregularity that is able to move under stresses that are much less than the yield stress of the perfect crystal. The motion of a dislocation leads to plastic deformation. As with point defects, dislocations cause perturbations in the crystalline matrix for several lattice distances. Dislocations in covalent solids are characterized by "dangling" covalent bonds that trap impurity atoms and lock dislocations in place (Billington and Crawford 1961).

Covalent bonds are directional and rigid in nature. Covalent crystals depend on appropriate geometric arrangement for stability. These characteristics result in more difficulty for an interstitial or vacancy to diffuse in the lattice, as compared to its ability to diffuse in an ionic crystal. Additionally, the rigid character of the covalent crystal prevents (or limits) small-scale atomic rearrangement that can relieve localized stresses near point defects. Activation energies for the migration of interstitials or vacancies are expected to be higher in covalent crystals than in ionic crystals because, for covalent crystals, bond rupture and reformation must occur for an atom to change places with a vacancy.

Fast-neutron (n_f) irradiation of quartz for doses up to about 3×10^{19} n_f/cm^2 resulted in damage that was primarily attributed to point defects and small, disordered regions (1,000–10,000 atoms). The resultant lattice vacancies and interstitials are assumed to be almost entirely oxygen vacancies and interstitials because (a) formation of Si vacancies requires more energy and (b) Si interstitials are much less chemically stable than are O interstitials. The formation of the vacancies and interstitials in the quartz results in lattice expansion and, thus, in a decrease in density. At higher doses, the concentration of disordered regions increase, which results in increased stress. These effects ultimately cause the destruction of the crystalline order, leaving an amorphous solid.

Neutron-irradiation studies have been conducted also on natural crystals, which are termed “metamict minerals” (Sect. 2.4.2.2). Crawford and Wittels (1956) define *metamict minerals* as those “whose structures have been disordered by bombardment over geologic periods with alpha particles and natural radioactive elements.” Irradiation of metamict minerals has resulted in lattice expansion and, in some cases, complete disordering of the lattice at high doses (Crawford and Wittels 1956). Based on the evidence found for metamict crystals, Billington and Crawford (1961) draw two general conclusions about inorganic compounds: (1) “Structural alterations are less pronounced the greater the ionic character of the bonding," and (2) "Radiation sensitivity is greater the lower the symmetry" (or, in other words, the higher the anisotrophy).

For studies with diamond, optical and magnetic changes have been shown to result from the direct displacement of carbon atoms from their equilibrium positions. Neutron bombardment of diamond results in a much higher production of disordered regions than does electron or gamma irradiation. By contrast, both quartz and fused silica are colored (i.e., color centers are produced) by both ionization and radiation-induced displacement. Several types of imperfections are possible in the quartz, including: a ruptured covalent Si-O bond with sufficient separation between the Si and the O such that the bond is not easily reformed, an oxygen vacancy, an oxygen interstitial, and an internetwork O_2 or O_2^+. Billington and Crawford (1961) state that missing Si atoms are not likely because of the greater number of bonds restraining them and the high chemical reactivity expected for such sites.

Defects can have a magnetic moment, which can be measured to provide the defect concentration. Measurement of the concentration of magnetic defects (i.e., the magnetic center density) in quartz shows a linear increase in the magnetic center density with fast neutron dose (up to about 3×10^{19} n_f/cm^2). A maximum center density is reached at a dose of about 4×10^{19} n_f/cm^2 and then decreases (Stevens, Sturm, and Silsbee 1958). This result suggests that a saturation value of magnetic defects is reached. The dose for maximum magnetic center density corresponds closely to the dose at which expansion (or distortion) of the crystal is observed to begin. The magnetic center density is a measure of the concentration of ruptured covalent bonds, which are caused by displacement of oxygen atoms, and which contribute to the instability of the lattice. Ultimately, the quartz lattice rearranges itself to relieve stresses. The magnetic center density then decreases (as observed experimentally) as the crystalline lattice becomes amorphous (Billington and Crawford 1961).

Optical absorption spectra for irradiated quartz and fused silica have been used to identify the nature of the irradiation-produced defects in these materials. Neutron irradiation of both quartz and silica showed that the intensity of an optical absorption band reached saturation with increasing neutron dose (Billington and Crawford 1961). These defects were found to anneal upon heating of the quartz above 500°C (Billington and Crawford 1961) and the silica above 550°C (Nelson and Crawford 1958).

2.3.2 Ionic Crystals

As stated in Sect. 2.3.1, covalent bonds are directional in nature, and covalent crystals depend on appropriate geometric arrangement for stability. When extensive disorder (caused by defects) is introduced, the covalent bonds are weakened, and the crystal then expands and loses its structure. By contrast, within ionic crystals, the arrangement of the ions depends upon electrostatic forces and the size of the ions. Lattice defects in ionic crystals have a higher degree of freedom to migrate, as compared to those of covalent crystals, because directional bonds do not have to be ruptured and reformed to allow for migration. As a result, ionic crystals can accommodate a large amount of disorder without exhibiting the extensive structural changes observed in covalent crystals. In general, the greater the ionicity of bonding, the greater the tendency of a crystal to resist structural changes upon irradiation. The description of radiation effects on ionic crystals by Billington and Crawford (1961) is summarized in the following paragraphs. Additionally, the effects on one particular type of ionic crystal, the LiF-BeF_2 salts used in the MSRE, are described.

Ionic conductivity studies have been performed on KCl crystals that were irradiated by neutrons, protons, and gamma rays. For particle-irradiated KCl, the ionic conductivity was found to increase. This increase apparently resulted from a higher concentration of positive-ion vacancies available for charge transport (Billington and Crawford 1961, Nelson, Sproull, and Caswell 1953). Heating of the irradiated material resulted in annealing, which began at about 175°C. At temperatures above 250°C, the material completely annealed, and the ionic conductivity returned to the pre-irradiation value. In some annealing experiments for alkali halides, the lattice contracts to a size less than that of the pre-irradiated value, indicating the relaxation of pre-existing strains.

By contrast, for gamma-irradiated KCl, the ionic conductivity decreased, as compared to its nonirradiated counterpart. Billington and Crawford (1961) suggest that the decrease in the ionic conductivity "may result from the relaxation process" in the lattice. Note that for short, fast neutron exposures ($<< 10^{16}$ n_f/cm^2), the ionic conductivity deceases, while for longer exposures ($> 10^{16}$ n_f/cm^2), the ionic conductivity increases (characteristic of the particle irradiations). Hence, it appears that relaxation may occur during the early stages of a reactor irradiation of a sample, followed by the buildup of positive ion vacancies.

Billington and Crawford (1961) described optical effects that have been observed after irradiation of alkali halides, MgO, and Al_2O_3. Generally, in alkali halides the same absorption bands are produced by charged particles and photons.

Different radiation types have been shown to produce different absorption bands in MgO. Some of the bands are the result of impurity atoms. In neutron-irradiated MgO, it appears that F-centers (i.e., an electron trapped at an oxygen vacancy) are produced (Wertz et al. 1957). Ionizing radiation does not produce these centers. Electron and neutron irradiation of MgO produces a band (at 2,550 Å) that is attributed to the F′ center (i.e., two electrons trapped at an oxygen vacancy). The bands produced by X-ray or electron irradiation were found to be thermally unstable— even decaying in the dark at room temperature. On the other hand, the neutron-produced bands were much more stable, with one band remaining even after heat treatment of the sample up to 900°C.

Similar to MgO, neutron irradiation of Al_2O_3 produces absorption bands in addition to those produced by gamma irradiation. For gamma irradiation, the bands were found to saturate at low exposures and, in fact, may be associated with impurity centers rather than defects in the Al_2O_3 lattice. Billington and Crawford (1961) point out that for crystals such as MgO and Al_2O_3, which consist of divalent and trivalent ions, the lattice energy is greater than that in the monovalent alkali halides. Therefore, ionizing radiation may be unable to impart the energy required to create lattice defects in MgO or Al_2O_3, while it can impart sufficient energy in the alkali halides.

In ionic crystals, the majority of structural effects are associated with simple defects: interstitials and vacancies. F-center concentrations in alkali halides that were exposed to X rays have been measured. As X-ray exposure increased, F-center concentration increased with a corresponding decrease in density. Both parameters reached a saturation value as exposure increased (Estermann, Leivo, and Stern 1949). Saturation has been explained in terms that once a certain concentration of interstitials and vacancies are reached, it is equally probable that either additional collisions will knock an interstitial back into a vacancy or that a new interstitial-vacancy pair will be created (Pease 1954).

Bombardment of KCl with protons has also shown a decrease in the density. Furthermore, neutron irradiation of alkali halides has shown a greater density decrease than that produced by protons or X rays (Billington and Crawford 1961). This result suggests that neutrons are more effective at producing vacancies and interstitials in these materials than are protons and X rays.

In addition to changes in ionic conductivity and optical properties, mechanical properties of irradiated alkali halides have also been studied. Irradiation of KCl with protons, X rays, and electrons has resulted in increased hardness in the specimen; saturation in the hardness has been demonstrated (Vaughan, Leivo, and Smoluchowski 1953, Westervelt 1953). The yield stress in LiF crystals that were exposed to neutrons was found to increase, ultimately reaching a saturation value (Gilman and Johnston 1958).

A number of irradiation studies have been performed on the ionic MSRE fuel salts (LiF-BeF_2) (Williams, Del Cul, and Toth 1996, Toth and Felker 1990, Haubenreich 1970). These studies were more chemically oriented than most solid-irradiation studies, which focus primarily on the production of defects and lattice changes. For experiments on the MSRE-type salts, the focus was on the production and migration of fluorine radicals, ultimately resulting in the production of F_2 gas. The amount of gas produced is a measure of the amount of damage to the matrix. Gas yields ranging from 0.005 to 0.045 F_2 molecules/100 eV have been reported, with a consensus from the studies that the expected yield is about 0.02 F_2 molecules/100 eV (Williams, Del Cul, and Toth 1996). The salts were found to exhibit an induction period during which no gas was measured in the void space of the sample container. This period was then followed by a linear increase in the gas pressure, and finally, a saturation pressure (or a plateau) was reached. Figure 2.5 depicts a typical gas yield curve for irradiation of an alkali halide salt. The characteristics exhibited in this curve are typical of most radiolysis experiments. In many cases, an induction period is not observed, but usually the linear increase and plateau are seen.

The induction period is probably related to the accumulation of gas in the crystalline lattice and the rate of diffusion of the gas molecules out of the lattice. For gamma irradiation of MSRE-type salts, the induction period was found to range from 1.3–17 W-h/g (equivalent to $4.7\text{–}61 \times 10^8$ rad). The observed plateau represents the maximum damage limit to the crystal at a particular dose rate. The maximum matrix damage by gamma irradiation of LiF-BeF_2 has been measured by Toth and Felker (1990) to be about 2% for dose rates up to 10^8 rad/h. Toth (1990) also performed alpha irradiation experiments for LiF-BeF_2 by doping the salt with ^{238}Pu. No F_2 was produced after 1.5 years of irradiation.

ORNL DWG 99C-6870

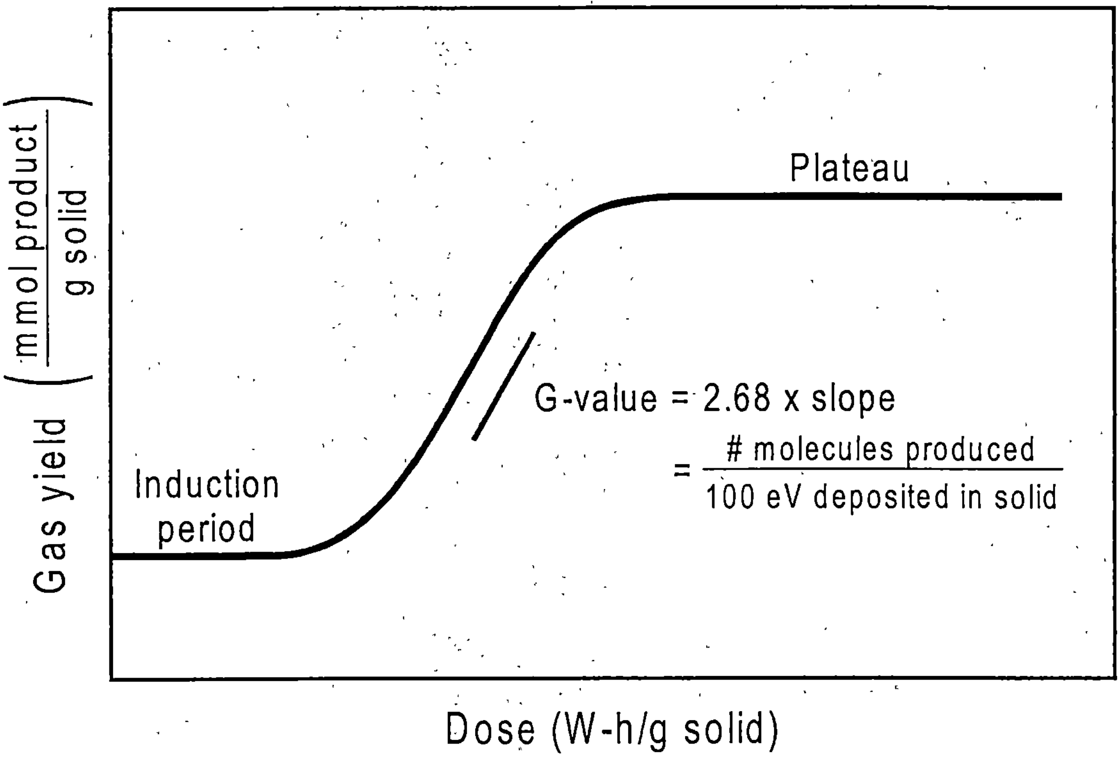

Fig. 2.5. Typical gas yield curve for irradiation of an alkali halide salt.

2.3.3 Crystals with Mixed Bonding

Rosenwasser, Dreyfus, and Levy (1956) pointed out that another class of crystals is of interest with respect to radiation damage— namely, crystals that have mixed bonding with both ionic and covalent components. Examples of such crystals include $Ba(NO_3)_2$ (with the Ba^{+2} and the NO_3^- ions), NaN_3 (with the Na^+ and N_3^- ions), $NaNO_3$ (with the Na^+ and NO_3^- ions), and UO_2F_2 (with the UO_2^{+2} and F^- ions), for which no previous results have been presented.

Allen and Ghormley (1947) studied the effects of irradiating of $Ba(NO_3)_2$ crystals with 1.2-MeV electrons. Doses up to 25 W-h/g (9×10^9 rad) were used. At the completion of an irradiation, the salt was dissolved in water, and the gases produced and the composition of the solution were analyzed. It was found that nitrite (NO_2^-) and oxygen were produced. Most of the oxygen was trapped (as O_2 or O) in the crystal and was released upon dissolution. The authors suggest that the electron bombardment of the crystal strips electrons from the NO_3^-, resulting in the formation of NO_3 radicals. The following reactions may then occur:

$$NO_3 + e^- \rightarrow NO_2^- + O; \text{ or} \tag{2.2}$$

$$NO_3 \rightarrow NO_2 + O. \tag{2.3}$$

During the experiments, it was found that the production rate of NO_2^- decreased with increasing dose, suggesting that steady state was being approached. Allen and Ghormley (1947) indicate that, based on their experiments, steady state may be reached after about

40% conversion of NO_3^- to NO_2^-. Such a steady state would occur when back reactions, resulting in the production of NO_3^-, equals the forward reaction.

Henning, Lees, and Matheson (1953) irradiated $NaNO_3$, KNO_3, and $KClO_3$ in a nuclear reactor to study radiation effects on these materials. Samples of $NaNO_3$ were also irradiated with X rays. After irradiation, the samples were heated to release gases trapped within the crystals. The nitrite content in the $NaNO_3$ and KNO_3 samples was also evaluated. An analysis of gases obtained from a $NaNO_3$ sample revealed that the gas was primarily O_2 with a small amount of N_2. The authors do not report on the analysis of the gases from the other samples, so the presence of N_2 in these samples is unknown. However, O_2 yields (G-values) were reported for each of the samples.

Following the theory of Allen and Ghormley (1947) regarding the mechanism for NO_2^- and O_2 production, one would predict that two NO_2^- ions will be produced for every O_2 molecule produced. Henning, Lees, and Matheson (1953) found that the ratio of NO_2^- to O_2 for their experiments was in reasonable agreement with this prediction. The ratio was 2.04 for a KNO_3 sample and 1.67 for a $NaNO_3$ sample.

The G-values reported by Henning, Lees and Matheson (1953) for the production of O_2 for different samples and doses are provided in Table 2.1. For the irradiation of $NaNO_3$, it appears that the G-value decreases with higher total doses, indicating an approach to steady state. The authors concluded that the variation in the O_2 yield for the two nitrates must be related to the crystal structure since the N-O bond strength is about the same for both materials. Because of the different size of the unit cell, there is about 20% more open space available per nitrate in KNO_3 crystals, as compared to $NaNO_3$.

Hence, it is easier for an O atom to migrate in the KNO_3, resulting in a higher yield, as shown in Table 2.1. Magnetic susceptibility measurements of irradiated KNO_3 showed that the oxygen was trapped as oxygen gas in the crystal. Similar studies were not reported for $NaNO_3$. Finally, Henning, Lees, and Matheson (1953) state that the higher yield of O_2 from the $KClO_3$ (as compared to the nitrates) resulted from the weaker Cl-O bond (as compared to the N-O bond).

Table 2.1. Reported gas yields from the nuclear reactor irradiation of $NaNO_3$, KNO_3, and $KClO_3$[a]

Material	Estimated dose (10^8 rad)	$G(O_2)$ (molecules O_2/100eV)
$NaNO_3$	3.16	0.333, 0.361
$NaNO_3$	4.13	0.334, 0.360
$NaNO_3$	4.81	0.205, 0.261
$NaNO_3$	5.27	0.273
$NaNO_3$	8.61	0.145
$NaNO_3$	11.8	0.195
KNO_3	3.76	0.79,0.92
$KClO_3$	2.07	2.60, 2.70
$KClO_3$	2.61	1.57

[a] Adapted from Henning, G., R. Lees, and M. S. Matheson, 1953. "The Decomposition of Nitrate Crystals by Ionizing Radiations," *J. Chem. Phys.* **21**(4), 664–668.

Gas yields from the X-ray irradiation of $NaNO_3$ by Henning, Lees, and Matheson (1953) (Table 2.2) were very similar to those measured for the reactor irradiations. The energy of the X rays used in the irradiations was not high enough such as to produce photoelectrons with sufficient energy to displace oxygen atoms. Because of the similarity in the gas yields seen for the reactor and the X-ray irradiations, the authors concluded that the oxygen was removed by an ionization mechanism [as suggested by Allen and Ghormley (1947)] rather than by direct displacement of the oxygen by a "knock-on" process (see Sect. 2.2.4).

Heal (1953) and Rosenwasser, Dreyfus, and Levy (1956) performed irradiation experiments on sodium azide (NaN_3). Heal used X rays as the radiation source, while Rosenwasser, Dreyfus, and Levy (1956) used gamma rays, slow neutrons, and fast neutrons. Heal conducted irradiations at 51 and 102°C and, upon completion of an irradiation, dissolved the sample in water and measured (a) the volume of gas evolved and (b) the amount of OH^- and NH_3 (produced by the reaction of trapped radicals with

Table 2.2. Reported gas yields from the X-ray irradiation of $NaNO_3$[a]

Estimated dose (10^8 rad)	$G(O_2)$ (molecules O_2/100eV)
0.584	0.27
0.0649	~0.38

[a] Adapted from Henning, G., R. Lees, and M. S. Matheson, 1953. "The Decomposition of Nitrate Crystals by Ionizing Radiations," *J. Chem. Phys.* **21**(4), 664–668.

water) in solution. Heal reports a G-value for the destruction of NaN_3 [G($-NaN_3$)] as 5.2 NaN_3 molecules destroyed per 100 eV at 102°C and 4.0 molecules destroyed per 100 eV at 51°C. The molar ratio of the measured yields of N_2, OH^-, and NH_3 was 1:0.72:0.25 at 102°C and 1:0.81:0.22 at 51°C. Absorption spectra showed that, after irradiation, the crystals did not contain colloidal sodium metal. Heal proposes that the observed product may be formed by the following reactions. First, the X radiation decomposes the azide ion:

$$N_3^- + \text{X-ray} \rightarrow N^- + N_2. \tag{2.4}$$

The N^- and N_2 are then trapped in the crystal. Upon dissolution, the N_2 is released, and the OH^- and NH_3 are formed by the following reactions with water:

$$N^- + H_2O \rightarrow NH + OH^- \tag{2.5}$$

$$NH + N_3^- \rightarrow NH^- + 3/2N_2 \tag{2.6}$$

$$NH^- + H_2O \rightarrow NH_2 + OH^- \tag{2.7}$$

$$NH_2 + N_3^- \rightarrow NH_2^- + 3/2N_2 \tag{2.8}$$

$$NH_2^- + H_2O \rightarrow NH_3 + OH^-. \tag{2.9}$$

This set of reactions would result in the formation of N_2, OH^-, and NH_3 in the molar ratio 4:3:1—essentially the ratio that was observed in the experiments.

Rosenwasser, Dreyfus, and Levy (1956) studied the reflectance spectra of NaN_3 after its irradiation with gamma rays, slow neutrons, and fast neutrons. For gamma irradiation, a strong band was observed at 3,600 Å. This band increased at a decreasing rate as the dose was increased, thus indicating an approach to saturation. Irradiation with neutrons showed the production of an additional band at 6,000 Å. This band was not produced by gamma irradiation. The authors speculate that the 3,600 Å band may be a color center band (such as are observed in the alkali halides) formed by ionizing radiation. Ionization of the azide ion may leave it in an excited state, which, in turn, may cause it to disintegrate and produce N_2. The authors suggest a number of potential sources for the neutron-irradiation-produced band at 6,000 Å. This band may have resulted from the aggregation of sodium into colloidal particles—either by disruption of the lattice or by the release of displaced N atoms during heating, resulting in an unstable configuration. Note, however, that absorption spectra measured by Heal (1953) provided no evidence of colloidal sodium metal. Other possible causes of the band at 6,000 Å are electrons trapped at azide or nitrogen ion vacancies, atom displacement by neutron collisions, or thermal spikes. Based on the experiments, however, the authors were unable to provide evidence that any of these mechanisms caused the observed bands.

2.3.4 Summary of Irradiation Effects on Covalent, Ionic, and Mixed-Bonding Crystals

A large number of irradiation studies have been performed on covalent crystals, ionic crystals, and the so-called mixed-bonding crystals, which exhibit both ionic and covalent bonding. Because covalent crystals have bonds that are directional in nature, small-scale atomic rearrangement to relieve localized stresses is prevented. Activation energies for movement of interstitials or vacancies within covalent crystals is expected to be higher than the activation energy for movement within ionic crystals. Additionally, high doses to covalent crystals result in extensive damage to bonds, with the lattice ultimately being destroyed (or becoming microcrystalline). A natural example of this effect are metamict minerals (see Sect. 2.4.2.2), which, after long periods of bombardment by naturally occurring radioactivity, exhibit a complete disordering of the crystalline lattice.

The arrangement of the ions in ionic crystals depends upon electrostatic forces and the size of the ions. Defects have a higher degree of freedom to move than they do in covalent crystals. Consequently, ionic crystals are more resistant to structural changes than are covalent crystals. Gamma irradiation of some ionic crystals (i.e., MSRE-type salt) has shown an induction period before any gas is released, followed by a period in which the amount of gas released is proportional to the dose. Finally, a plateau or saturation amount of gas is reached, signifying a damage limit in the crystal for that dose rate.

Mixed crystals have both covalent and ionic bonds. For the experiments discussed, gases produced during the irradiation were trapped within the crystalline lattice, and these gases were released upon heating or dissolution of the crystal. Upon dissolution, some of the radiolytic products trapped in the crystal also reacted with the water to form other products. Additionally, from the experiments described, it appears that the bulk damage is to the covalent part and not the ionic part of the crystals.

One feature that is common to the covalent, ionic, and mixed crystals, which were described, is that, as dose is increased, *saturation* in the damage is reached. In covalent crystals, magnetic center densities and optical bands have been shown to saturate. In ionic crystals, saturation has been shown for F-center concentrations, the decrease in crystal density, and hardness of the crystals. Of course, for ionic crystals, a good example of saturation is the pressure plateau of product gases reached at high doses to LiF-BeF_2. Finally, in mixed crystals, saturation has been demonstrated in the production of NO_2^- from NO_3^-, in the production of O_2, and in optical absorption spectra. It is noteworthy that saturation has been observed in other (noncrystalline/nonsolid) systems. A good example is the radiolysis of water in which a plateau is reached when *back reactions*, resulting in the reformation of water, balance the destruction of water (Allen et al. 1952). Saturation in crystalline materials is analogous in that, at some point, a maximum damage limit is reached in which the rate of production of defects is balanced by the annealing (thermal or chemical) of the defects.

2.4 RADIATION EFFECTS ON OXIDES AND URANIUM OXIDES

In previous subsections, the interactions of radiation with solids and the subsequent effects on crystalline solids (covalent, ionic, and mixed ionic-covalent) were described. Some of the materials used in the examples of radiation effects were oxides. In Sect. 2.3.1, the effects of both neutron and gamma irradiation of the covalent crystal SiO_2 (as quartz or fused silica) were described. The effects of irradiation by neutrons and electrons on MgO and gamma irradiation of Al_2O_3 were presented in Sect. 2.3.2. Both oxides form ionic crystals. Finally, in Sect. 2.3.3, the effects of radiation on the oxygen-containing, mixed-bonding crystals $Ba(NO_3)_2$, $NaNO_3$, KNO_3, and $KClO_3$ were discussed. Electrons, neutrons, and X rays were used in these mixed-bonding studies, and, in each case, O_2 was released from the crystal.

In Sect. 2.4.1, additional information is provided concerning radiation effects on oxides. A proposed mechanism of energy deposition and migration to the crystal surface is described. In Sect. 2.4.2, radiation effects on uranium oxides and on the atmosphere over the uranium oxides are described. Uranium oxides are to be placed into long-term storage. Radiation will interact with the oxide and impurities (e.g., fluorides and water) that are present. Therefore, it is important to (a) understand the effects of radiation on both the pure material and impurities and (b) to evaluate the radiolytic contribution from each of the components of these heterogeneous systems. Information is presented on the direct and indirect effects [i.e., radiation interacting with an impurity (e.g., water), resulting in some effect (e.g., oxidation) on the uranium oxide] of radiation on the uranium oxides. Finally, because it is important to understand the interaction of the storage atmosphere with the uranium oxide, information is presented on the radiolysis of moist air.

2.4.1 Oxides

The radiation damage mechanisms, which are described in Sects. 2.3.1–2.3.3, were for the *bulk* crystal. Alternative mechanisms have been proposed in which energy, deposited in the bulk, migrates to the *surface* where the radiolytic reaction occurs. Such mechanisms have been proposed for ZnO and MgO.

Sugier and Duda (1976) examined the gamma radiolysis of ZnO, which forms simple ionic crystals. They measured the amount of oxygen directly evolved from the ZnO crystals and calculated a yield of G(O) = 0.92 (O atoms)/100 eV. They proposed that the O_2 production is primarily a surface phenomenon whereby energy deposited in the bulk material is rapidly transferred through the crystal lattice to the surface, where it causes radiolysis. It is unlikely that the oxygen is produced in the bulk and then migrates to the surface because (a) diffusion of the O_2 is slow and (b) the needed concentration gradient would imply an induction period, which was not observed. Also, there was a linear relationship between the dose rate and the yield—a relationship which supports the idea of energy migration from the bulk to the surface.

Wysocki (1986) irradiated MgO with gamma rays. Different species of oxygen were observed at the surface (e.g., O_2^- and O_3^-). Depending on the surface area, reported G-values for the oxygen species at the surface ranged from 1.18 to 3.68 (O species)/100 eV. Oxygen was initially observed in the gas space; however, its concentration declined as it was reabsorbed on the MgO surface. Wysocki also states that the gamma energy is deposited in the bulk material and then migrates to the surface, where it causes radiolysis.

While these authors address surface phenomena, it is not clear whether or not examinations were made for bulk effects. Based on the theory presented, after irradiation, one could open a crystal and find that the MgO and ZnO inside were undamaged. This, however, seems doubtful.

2.4.2 Uranium Oxides

A range of effects are possible when radiation interacts with uranium oxides. These effects may be manifested as chemical (e.g., oxidation) or structural (e.g., change in crystal structure) changes to the irradiated material. These two types of changes then serve as logical divisions of the study of radiolytic effects on uranium oxides.

McEachern and Taylor (1998) have provided a broad survey of the mechanisms for oxidation of uranium dioxide at temperatures below 400°C. Several of these mechanisms are attributed to direct irradiation of the oxide, or indirectly to irradiation of associated impurities—namely, the influence of moisture, nitrogen oxides, and radiation upon oxidation. The presence of moisture serves as a source of radiolytic products (e.g., H_2O_2 and free radicals such as OH), which can cause oxidation of the uranium dioxide. Similarly, the radiolytic production of nitrogen oxides (in the presence of air and moisture) can accelerate oxidation. Finally, radiation can cause lattice defects, which can accelerate oxygen diffusion and, hence, increase oxidation. Moisture and moist air may both be present in the uranium oxide storage environment. Therefore, it is important to understand their effects on the uranium oxides during irradiation.

Changes to the crystal structure have been reported under nuclear reactor irradiation conditions for some uranium oxides (Belle 1961). Additionally, damage to the lattices of minerals found in nature because of either self-irradiation or external radiation has been reported (Lustman 1961). Such materials undergoing the latter phenomenon are referred to as being in the metamict state.

This description of radiolytic effects on uranium oxides has been divided into two major areas—oxidation and structural effects. In Sect. 2.4.2.1, oxidation is described in terms of three variables: moisture, nitrogen oxides, and radiation. Structural changes resulting from nuclear reactor irradiation, alpha decay, and naturally present radioactivity are described in Sect 2.4.2.2.

2.4.2.1 Oxidation

A significant number of studies have been performed on the oxidation of uranium oxides (McEachern and Taylor 1998). Many of these studies have focused on the effect of moisture (and, hence, the radiolytic products of water) on the oxidation of UO_2 to higher oxides. Structural changes contribute to volumetric changes during oxidation. The molecular volumes of uranium oxides increase steadily with increasing O:U ratio (Katz and Rabinowitch 1951).

Taylor et al. (1989) summarized the relative volumes (as compared to UO_2) of various uranium oxides. These volumes, which are presented in Table 2.3, illustrate the dramatic change in volume as uranium is oxidized. There is about a 36 vol % increase for complete oxidation from UO_2 to U_3O_8, while there is a 162 vol % increase for oxidation from UO_2 to $UO_3•2H_2O$. Note that Table 2.3 shows an initial volume decrease as the UO_2 is oxidized to U_3O_7. This decrease is visually evident in some samples.

Sections 2.4.2.1.1 through 2.4.2.1.3 describe the dependence of uranium oxide oxidation upon moisture, nitrogen oxides, and radiation, respectively.

Table 2.3. Volumes of various uranium oxides relative to UO_2[a]

Compound	Relative volume[b]
UO_2	1.000
α-U_3O_7	0.988
β-U_3O_7	0.973
α-U_3O_8	1.358
α'-U_3O_8	1.357
β-U_3O_8	1.369
$U_3O_8(OH)_2$	1.730
$UO_3 \bullet 0.8H_2O$	1.850
α-$UO_2(OH)_2$	1.836
β-$UO_2(OH)_2$	2.156
γ-$UO_2(OH)_2$	2.222
$UO_3 \bullet 2H_2O$	2.618

[a] Adapted from Taylor, P., D. D. Wood, A. M. Duclos, and D. G. Owen, 1989. "Formation of Uranium Trioxide Hydrates on UO_2 Fuel in Air-Steam Mixtures Near 200°C," *J. Nucl. Mater.* **168**, 70–75.

[b] Volume relative to UO_2.

2.4.2.1.1 Moisture

Sunder et al. (1990) studied the effects of radicals (in particular, the effects of $OH^{\cdot}$ and O_2^-), formed by radiolysis of water, on the oxidation and dissolution of UO_2. Solution chemistry was controlled to promote the formation of a particular radical. For gamma radiolysis, a water solution saturated with N_2O resulted in the preferential production of OH radicals. Similarly, for a solution saturated with O_2 and containing either formate ($HCOO^-$) ions or t-butanol [$(CH_3)_3COH$], gamma radiolysis resulted in the preferential formation of O_2^- radicals. For experiments performed with argon-saturated water solutions, a mixture of OH and e_{aq}^- (i.e., hydrated electron) radicals were formed.

In a separate paper, Sunder et al. (1989) described the formation of the various radicals under the controlled chemical conditions of their experiments. A solution that is saturated with N_2O favors formation of OH radicals because the e_{aq}^- are scavenged, as illustrated by the following equation:

$$e_{aq}^- + N_2O \rightarrow N_2 + OH^- + OH \qquad (2.10)$$

The t-butanol or the formate react with the OH radical, thereby allowing the e_{aq}^- and H radicals to react with O_2 to produce O_2^-. The addition of t-butanol results in the following reaction:

$$OH + (CH_3)_3COH \rightarrow H_2O + (CH_3)_2(CH_2)COH \qquad (2.11)$$

Formate reacts with OH radicals as follows:

$$OH + HCOO^- \rightarrow CO_2^- + H_2O \qquad (2.12)$$

Finally, O_2^- radicals are produced, as illustrated in the following equations:

$$e_{aq}^- + O_2 \rightarrow O_2^- \tag{2.13}$$

$$H + O_2 \rightarrow O_2^- + H^+ \tag{2.14}$$

$$CO_2^- + O_2 \rightarrow O_2^- + CO_2 \tag{2.15}$$

An ^{192}Ir source was used by Sunder et al. (1990) to perform the irradiations. The maximum dose rate was 30,000 rad/h. The rate and amount of oxidation were determined by measuring the corrosion potential. X-ray photoelectron spectroscopy (XPS) was used to determine the amount of surface oxidation [i.e., the relative amount of U(VI) and U(IV)].

Sunder et al. (1990) found that the oxidation of UO_2 was most sensitive to the dose rate for the N_2O-purged solutions (i.e., the solution that favors OH formation). Therefore, it appears that in a radiolytic environment, OH plays a key role in the oxidation of UO_2. Note that even at low (or no) doses, O_2 (in O_2-saturated solutions) can cause oxidation of UO_2.

Sunder et al. (1990) state that UO_2 oxidation occurs in two stages. Initially, a surface layer of $UO_{2.33}$ (U_3O_7) is formed, that is,

$$UO_2 \rightarrow UO_{2.33} \tag{2.16}$$

In the second stage, some of this layer dissolves (as UO_2^{2+}), and a thin layer of $UO_3 \bullet xH_2O$ (possible values of x are 0.5, 0.8, 1 and 2) is formed. XPS was used to evaluate the ratio of U(VI) to U(IV) on the surface of the UO_2 sample as a function of dose. Table 2.4

Table 2.4. U(VI):U(IV) ratio for various uranium compounds

Compound	U(VI):U(IV)
UO_2	0[a]
$UO_{2.25}$ (U_4O_9)	0.33
$UO_{2.33}$ (U_3O_7)	0.5
$UO_{2.5}$ (U_2O_5)	1
$UO_{2.67}$ (U_3O_8)	2
UO_3	∞[b]

[a] Uranium present as U(IV).
[b] Uranium present as U(VI).

provides the values of these ratios for various uranium oxides. It was found that the value of U(VI):U(IV) increased rapidly to 0.5, and then the rate of increase began to slow. A value of 0.5 for this ratio corresponds to $UO_{2.33}$— a value which is consistent with the theory of initial formation of a $UO_{2.33}$ layer. The increase of the ratio, with dose, above 0.5 reflected the formation of higher oxides (e.g., $UO_3 \bullet xH_2O$). Additionally, it was concluded that oxidation of this type is faster in the irradiated, deoxygenated (i.e., Ar-purged) solutions than in nonirradiated, oxygenated solutions because of the production of oxidizing radicals (e.g., OH) in the former.

For each of the solutions studied (i.e., oxygenated in combination with $HCOO^-$ or t-butanol, N_2O-purged, and Ar-purged), it was found that the rate of $UO_{2.33}$ layer formation (as measured by reaching a certain corrosion potential value) was proportional to the square root of the dose rate. Because the rate of formation of this layer is proportional to the radical concentration, it appears that the radical concentration is then proportional to the square root of the dose rate.

In addition to solutions, the role of the radiolysis of the atmosphere over the uranium oxide on oxidation has also been studied. Recent work by Sunder and Miller (1996) examined the oxidation of Canadian deuterium uranium (CANDU) reactor fuel at 150°C in a gamma radiation field. Four different atmospheres were used in these experiments: air (both in sealed and unsealed containers), O_2 with 60% saturated steam, and Ar with 60% saturated steam. Unirradiated (i.e., unexposed in a nuclear reactor) UO_2 disks that were about 13-mm in diameter and 3-mm thick were placed in containers with one of the 4 atmospheres. These containers were placed between spent CANDU fuel bundles for about 2 years. The gamma field was estimated to be about 15 Gy/h (1,500 rad/h). During the 2-year period, the containers were maintained at 150°C for 3 weeks and then at 30°C for 3 d to permit the sampling of gases from an unrelated experiment. This cycle was repeated throughout the 2 years. After completing the irradiations, the surfaces of the disks were examined by XPS, X-ray diffraction (XRD), and scanning electron microscopy (SEM).

The relative amounts of U(VI) and U(IV) on the surfaces of the samples were determined by XPS. For the three types of samples containing O_2 (either as air or as O_2), surface oxidation was evident. The most oxidation was observed for samples containing O_2 and 60% saturated steam. The U(VI):U(IV) ratios ranged from 2.2 to 118. For the sample with a U(VI):U(IV) ratio of 2.2, the authors state that likely a leak in the container resulted in a loss of water. This sample would then be equivalent to the other samples that were open to the atmosphere (and XPS measurements were consistent with such samples). The UO_2 samples in sealed-in-air containers showed the next most oxidation (with U(VI):U(IV) ratios ranging from 5.6 to 10). Finally, the open-to-air samples had U(VI):U(IV) ratios ranging from 2.6 to 3.7.

The samples that contained Ar and 60% steam exhibited no oxidation. For two of these samples, U(VI):U(IV) ratios were 0.01. One sample had a ratio of 0.4 (note that U_3O_7 has a ratio of 0.5); this observation was attributed to O_2 contamination during sample preparation.

The increased oxidation in the sealed-in-air samples, as compared to the open-to-air samples, was attributed to the formation of a greater concentration of oxidants (from the radiolysis of absorbed water on the UO_2 and container surfaces and moisture in the air) in the former. The radiolysis of air results in the formation of nitrogen oxides, which can also oxidize UO_2. It is believed that the open-to-air container allowed the oxidants to diffuse outward, while their concentration increased in the closed container.

Because the radiolysis of water produces both oxidants and reductants, it was proposed by Sunder and Miller (1996) that at high temperatures (such as 150°C used in these experiments), the rates of oxidation and reduction cancel each other. This proposal explains the lack of oxidation of the Ar-60% saturated steam sample. Note that at room temperature, the oxidation of UO_2 by water radiolysis products has been observed [Sunder et al. (1990)]. The reactivity of the reductants at room temperature is much less than that of the oxidants.

XRD analysis of the UO_2 disks confirmed the oxidation observed during the XPS analysis. The UO_2 samples that contained only air (both opened and sealed) exhibited UO_2, U_3O_7, U_3O_8, and U_8O_{19}. For the samples containing O_2 and 60% saturated steam, both UO_3 and $UO_3{\bullet}xH_2O$ were found in addition to the other uranium oxides. This serves as evidence of more complete oxidation of uranium to the U(VI) valence state. The samples that contained Ar and 60% saturated steam did not show that either U_3O_8 or $UO_3{\bullet}xH_2O$ were present. The sample that was thought to be contaminated with O_2 showed the formation of U_3O_7 and $U_{16}O_{37}$. For the other Ar-60% saturated steam samples, only UO_2 was found to be present. The SEM results were consistent with those from both the XRD and XPS analyses.

Wasywich et al. (1993) performed experiments to study the oxidation of defected and intact CANDU fuel, both in dry air and in moisture-saturated air at 150°C. Intact CANDU fuel elements and intentionally defected (single 3-mm-diam hole) CANDU fuel elements were placed in each of these two environments. The elements were placed in sealed containers with a void volume such that there was only enough oxygen available to oxidize a small fraction of the UO_2. Water was added to some of the containers for the moisture-saturated air experiments. After long storage times (on the order of 3 to 6 years), some elements were destructively analyzed by using optical microscopy, SEM, XPS, and XRD. Optical microscopy was used to identify the effects of localized oxidation (i.e., contraction and distortion) resulting from volume changes.

The UO_2 oxidation was observed only in the intentionally defected fuel elements. For the dry-air tests, oxidation was localized to the defect region. XPS showed that the

UO_2 was oxidized primarily to U_3O_7. The authors stated that, for the dry-air tests, the oxidation appeared to be controlled by diffusion of oxygen into the UO_2 lattice.

For the moist-air tests, oxidation occurred throughout the fuel element. For high-power (i.e., high-decay-energy) fuel, oxidation was observed in the fuel core region. XPS showed the formation of higher oxides (i.e., greater than U_3O_7), as compared to the dry-air oxidation. The oxidation appeared to proceed as dissolution (as UO_2^{2+}) and precipitation (as $UO_3 \bullet xH_2O$, $x \sim 0.8$) reactions. The authors point out three different processes in which radiolysis may contribute to oxidation. Radiolysis of water produces oxidizing solutions at the surface of the UO_2 through the formation of radicals such as OH. For aerated water, O_2^- can be formed [e.g., Sunder et al. (1990)]. Finally, radiolysis of moist air leads to the production of nitric acid, which can cause rapid oxidative dissolution of the UO_2.

Einzinger, Marschman, and Buchanan (1991) evaluated the oxidation of SNF at expected conditions during the postcontainment period in a geologic repository. This time period (300 to 10^4 years after disposal) would be characterized by a low radiation field (~4 R/h) and high dew-point air.

Samples of SNF were tested for a variety of temperatures, moisture levels, and test durations. Dew points were −55 or 80°C, while temperatures of 110, 130, and 175°C were used. Fuel samples (~10 g each) were used from both pressurized water reactors (PWRs) (~8 years since discharge) and boiling water reactors (BWRs) (~15 years since discharge).

Einzinger, Marschman, and Buchanan (1991) proposed a mechanism of rapid oxidation at the grain boundaries, which is followed by penetration of an oxidation front into the UO_2 grains. The growth of the oxidation front (and the resulting formation of U_3O_7) is described by the following equation:

$$1-[1-3\Delta(O/M)]^{1/3}=(kt)^{1/2}\ , \tag{2.17}$$

where

$\Delta(O/M)$ = change in oxygen-to-metal ratio,

k = rate constant, and

t = time.

For oxidation to U_4O_9, the term $3\Delta(O/M)$ in the equation is replaced by $4\Delta(O/M)$. Key assumptions for using this equation are that the particles are spherical, the particles oxidize independently, and oxidation does not penetrate deeply into the grains. The authors used this model to estimate values of the rate constant, k, for the various experiments performed. The rate constant showed an Arrhenius-type behavior with temperature.

Analyses of the samples showed that oxidation occurred more rapidly in moist atmospheres. Finally, the BWR samples appeared to oxidize more rapidly than did the PWR samples. This difference was attributed to the smaller grain size and, hence, larger surface area of the BWR fuel samples.

To evaluate the effects of moisture alone, Taylor et al. (1989) studied the oxidation of unused CANDU fuel for a number of air-steam mixtures near 200°C. More than 70 experiments were performed in which the amount of moisture and the surface finish of the UO_2 sample were varied. Disks, 2 mm thick, were cut from fuel pellets and were then polished. These disks were then further subdivided into quarters. Water and the UO_2 samples were added to a pressure vessel, which was then heated in an oven at 200 to 225°C for a period of 2 to 20 d. The balance of the atmosphere inside the containers was air. The volume of the container was such that oxygen depletion was not expected to affect the extent of oxidation. XRD was used to identify oxidation products. SEM was also performed on the samples.

Upon analysis, both $UO_3{\bullet}2H_2O$ and $UO_3{\bullet}xH_2O$ ($0.7 \leq x \leq 0.9$) were observed as well as some U_3O_7 and U_3O_8. Below 50% saturated steam, the oxidation rates were similar to those in a dry atmosphere, and only U_3O_7 or U_3O_8 was observed. For the range from 50% saturated steam to slightly over saturation, hydrated UO_3 was observed. These hydrates appeared to form at higher rates as temperature increased. For wet conditions (i.e., water in excess of that required for saturation) large crystals of $UO_3{\bullet}xH_2O$ were formed.

Taylor et al. (1989) concluded that for the conditions of less than 50% saturated steam, the moisture had little or no effect. Hence, the oxidation appears to have been controlled by oxygen diffusion into the UO_2 matrix and the solid-state oxidation of the UO_2 to U_3O_7 or U_3O_8. For the high-moisture conditions (i.e., greater that 50% saturated steam), the $UO_3{\bullet}xH_2O$ formation was described in terms of a dissolution-precipitation reaction at the UO_2 surface. This is the same reaction that appears to be enhanced in a radiation field.

2.4.2.1.2 Nitrogen Oxides

The presence of nitrogen oxides and nitric acid has been shown to cause oxidation of UO_2. These chemicals can be formed by the radiation of moist air.

Harteck and Dondes (1956) studied the use of radiation in the direct production of NO_2 and N_2O, and they summarized the radiochemcial reactions responsible for the production of these species. The key radicals in the radiolytic production of nitrogen oxides are N and O. The production of N radicals is described by

$$N_2 + \text{radiation} \rightarrow N_2^+ + e^- \tag{2.18}$$

$$N_2 + \text{radiation} \rightarrow N_2^* \tag{2.19}$$

$$N_2^* \rightarrow N + N \tag{2.20}$$

$$N_2^+ + e^- \rightarrow N + N \text{ or } N_2 + \gamma \text{ ,} \tag{2.21}$$

where the symbol * indicates an excited state. Oxygen radical production is described by the following equations:

$$O_2 + \text{radiation} \rightarrow O_2^+ + e^- \tag{2.22}$$

$$O_2 + \text{radiation} \rightarrow O_2^* \tag{2.23}$$

$$O_2^* \rightarrow O + O \tag{2.24}$$

$$O_2^+ + e^- \rightarrow O + O \text{ or } O_2 + \gamma \; . \tag{2.25}$$

The formation of NO_2 is described by

$$N + O_2 \rightarrow NO + O \tag{2.26}$$

$$2NO + O_2 \rightarrow 2NO_2. \tag{2.27}$$

The production of N_2O is described by the following equation:

$$NO_2 + N \rightarrow N_2O + O. \tag{2.28}$$

Note that a number of propagation reactions (e.g., $NO_2 + N \rightarrow N_2 + 2O$ and $NO_2 + O \rightarrow NO + O_2$) occur, but they are not shown. Finally, the reaction of NO_2 with water produces nitric acid, as described by the following equation:

$$3NO_2 + H_2O \rightarrow 2HNO_3 + NO. \tag{2.29}$$

Primak and Fuchs (1955) evaluated the effects of radiation on moist oxygen-nitrogen mixtures and the subsequent corrosion of metals. In addition to their experimental work, they summarized a number of observations concerning different types of materials that had been irradiated in air. These observations served as motivation for their work. Examples included a nickel mirror that became transparent after irradiation in an air atmosphere. A transparent, light-green coating (thought to be hydrated nickel nitrate) was found on the mirror. Nickel suspension wires used in a reactor parted in humid summer weather. A copper clip that had been irradiated in humid air exhibited a heavy, blue-green deposit (thought to be hydrated cupric nitrate).

Primak and Fuchs (1955) performed experiments on the corrosion of nickel in a variety of oxygen-nitrogen atmospheres. Nickel samples (0.071-cm in diameter and 5.1-cm long) were cleaned, polished, and placed in ampules containing the desired atmosphere. The ampules, further contained in aluminum tubes, were irradiated in the central region of a nuclear research reactor. For samples in dry oxygen-nitrogen mixtures, irradiated to about 30 MW-h, no reaction products were found on the nickel. However, for samples irradiated in a humid-air atmosphere, a large amount of light-green reaction products was found on the nickel surface. The products were identified as $Ni(NO_3)_2 \bullet 6H_2O$.

Jones (1959) studied the radiolysis of moist air caused by electron bombardment. In his paper, Jones refers to Russian work that found that yields of nitrogen oxides are about equal for electrons and gamma-rays in both liquid air and room-temperature air. Jones' experiments were performed by using a 10-cm infrared gas cell that contained the gas composition of interest and that had sodium chloride windows. Samples were irradiated with a 100-μA beam of 1.0-MeV electrons, which entered the cell through a gold-foil window.

Jones provided a description of the progress of a typical experiment and presented typical G-values for the yields. The G-values are dependent upon the air composition, but the typical values are illustrative of general trends. Electron bombardment of moist air produced nitric acid with a typical G-value of 2.9 HNO_3 molecules/100 eV. When the water was depleted, the HNO_3 began to be destroyed (G = −5.4 HNO_3 molecules/100 eV), and NO_2 was produced (G = 5.4 NO_2 molecules/100 eV). After decomposition of the HNO_3, NO_2 continued to be produced at an asymptotic G-value of 0.28 NO_2 molecules/100eV. Throughout the irradiation, N_2O was produced also with an asymptotic G-value of 0.55 N_2O molecules/100 eV. Ozone and nitrogen pentoxide were also observed to be formed and destroyed during the irradiation.

Mixtures of nitrogen, moisture, and various concentrations of oxygen were irradiated and spectroscopically examined by Jones. The G-values for HNO_3 production and destruction, NO_2 production, and N_2O production were found to vary as a function of O_2 concentration. The maximum G-value for all products occurred at an O_2 concentration of about 15%. Irradiation of moist N_2 showed no production of HNO_3, NO_2, or N_2O.

Anderson, Roberts, and Harper (1955) studied the oxidation of UO_2 in both O_2 and O_2-NO_2 atmospheres. The oxygen absorption (i.e., the weight gain from oxidation) was found to be proportional to the square root of time for UO_x compositions with values of x up to 2.10. This is expressed by the following equation:

$$C = Kt^{1/2} + A\,, \tag{2.30}$$

where

C = oxygen absorbed,

t = time, and

K, A = constants.

The constant K is a measure of the oxidation rate and shows a dependence on pressure.

Experiments with O_2 were carried out at a number of temperatures and pressures, while experiments with O_2-NO_2 mixtures were carried out at a pressure of 0.5 atm and for two temperatures—131 and 155°C. Table 2.5 provides values of the constants K and A for O_2 and O_2-NO_2 oxidation of UO_2. The experiments that were performed at similar pressures and temperatures should be comparable. Hence, it appears from examination of Table 2.5 that the rate of oxidation in the O_2-NO_2 mixture (as indicated by the rate constant K) is about twice that in O_2 alone at the same temperature and pressure.

Table 2.5. Values of the constants K and A for various temperatures and pressures for O_2 and NO_2 oxidation of UO_2[a]

Atmosphere	Temperature (°C)	Pressure (Torr)	K	A
O_2	154	480	0.80	0.9
O_2	153.4	480	0.62	0.5
O_2	155	480	0.42	-0.3
O_2	153	480	0.29	0.05
O_2-NO_2	155	380	1.44	0.8
O_2	131	480	0.35	0.4
O_2	131	480	0.24	0.1
O_2-NO_2	131	380	0.64	0.8

[a] Adapted from Anderson, Roberts, and Harper (1955).

Oxidation tests were performed, both with and without an external gamma field, on nonirradiated UO_2 fuel pellets by Campbell et al. (1989) to evaluate the effects of air and air containing NO_2. The UO_2 pellets were placed in air and in air containing 1% NO_2, and were then heated to 250°C. For the 1% NO_2-air mixture, the pellet weight gain was about 5 wt % after 600 h, while pellets in air only gained about 1 wt %. XRD was used to determine the chemical form of the uranium oxide formed. Oxidation in the 1% NO_2-air mixture led to formation of a composition that was about 95 wt % UO_3. Oxidation in air led to formation of a composition that was about 24 wt % U_3O_8. Hence, the oxidation rate in the presence of NO_2 was greater than that in air. Additionally, the uranium was oxidized to a higher oxidation state (UO_3) in NO_2 than that attained in air.

Campbell et al. (1989) examined the effects of radiation by irradiating pellets in air using a ^{60}Co source with an exposure rate of about 2×10^5 R/h. Experiments were carried out at 200, 215, and 230°C. The oxidation rate in a static system (as compared to that in air without irradiation) increased because of the increased formation of oxidants by radiolysis of air. For a flowing-gas system (i.e., air swept through the irradiation chamber), no irradiation effects were observed. For the flowing system, it appears that the radiolytically-produced oxidants were swept away from the UO_2.

2.4.2.1.3 Radiation

As discussed in Sects. 2.4.2.1.1 and 2.4.2.1.2, radiation indirectly effects oxidation of uranium oxides through the radiolytic production of oxidizing species. McEachern and Taylor (1998) point out a second potential role for radiation with respect to oxidation —production of lattice defects. Such defects may enhance oxygen diffusion into the uranium oxide lattice and thereby increase the oxidation rate.

Dominey (1968) compared oxidation of UO_2 by CO_2 in a reactor with oxidation of UO_2 by O_2 in the absence of a radiation field. Temperatures during reactor irradiation varied between 60 and 90°C. Two experiments with O_2 oxidation and no irradiation were performed—one at 66 and the other at 80°C. It was found that the oxidation rate for the reactor-irradiated samples was about the same as that for the nonirradiated O_2 oxidation experiment conducted at 80°C. Dominey concluded that if the reactor temperature was 80°C or above, then the rate of oxidation could be explained by thermal diffusion. However, for lower reactor temperatures, the diffusion must be enhanced to explain a larger-than-expected diffusion rate.

McEachern and Taylor (1998) conclude that, based on the experimental evidence to date, the rate of oxidation of UO_2 is affected only slightly, if at all, by radiation alone. They state that such effects are more likely to be observed for defect-free materials (e.g., monocrystalline UO_2) and less likely to be observed for highly defected materials (e.g., SNF). This conclusion follows from the assertion that radiation introduces defects that enhance that rate of O_2 diffusion into the lattice. These effects are likely to occur only at low temperatures because the defects begin to anneal at higher temperatures (200 to 300°C).

2.4.2.2 Structural Changes

Lustman (1961) summarized changes in both structure and properties as a result of nuclear reactor (i.e., neutron) irradiation for a number of compounds. Several of the studies summarized were for effects on UO_2 or U_3O_8. Structural changes for UO_2 irradiated in a reactor (~3.4×10^{18} fissions/cm^3) were evaluated by using XRD. XRD spectra of UO_2 both before and after irradiation were compared, and neutron irradiation was shown to broaden the diffraction peaks. This broadening was attributed to increased lattice strain. For UO_2 that was prestrained (by the method of preparation), irradiation produced little additional lattice strain. In fact, in some cases, the strain decreased because the irradiation annealed the lattice. Typically, reactor irradiation of UO_2 causes a slight expansion of the lattice, which can be annealed by heating the material. Apparently, there is a steady-state condition of strain that is dependent on the temperature and dose rate.

The effect of neutron irradiation and, thus, fission fragments is significantly different for U_3O_8, as compared to the effects on UO_2. Lustman (1961) states that this observation should be expected because of the metamictization of weathered uraninites (i.e., UO_2 that has been oxidized to U_3O_8, as discussed later in this subsection). XRD analysis of U_3O_8 exposed to a relatively low dose (~1.9×10^{16} fissions/cm^3) showed no evidence of diffraction peaks. Consequently, the crystalline structure of the material is effectively destroyed or becomes microcrystalline. The strains caused by displaced atoms in the lattice, in turn, cause a relatively long-range disruption of the lattice structure.

Another difference between UO_2 and U_3O_8 described by Lustman (1961) is the energy release during heating. No energy release was observed for heating UO_2 (exposed to fission densities of about 8 × 10^{17} fissions/cm^3) to 750°C. Only small energy releases at 500°C were observed for $UO_{1.9}$. By contrast, heating of U_3O_8 (exposed to 7.5 × 10^{15} fissions/cm^3) from 150 to 350°C released about 25 cal/g. The energy release is a result of annealing and recrystallization of the U_3O_8 lattice. Lustman states that energy releases for U_3O_8 irradiated to higher doses are "consistent with the estimated latent heat of fusion of U_3O_8."

Nakae, Harada, and Kirihara (1978) studied the change in the crystal lattice parameter of UO_2 for several grain sizes as a function of fission dose (1.14 × 10^{14} to 2.92 × 10^{19} fissions/cm^3). Three distinct stages in the change of the lattice parameter were observed. During the first stage, the lattice parameter increased until it plateaued between doses of 1 × 10^{16} and 2 × 10^{16} fissions/cm^3. For some samples, the lattice parameter decreased with dose initially. This annealing behavior was thought to result from the relocation of excess oxygen (note that the O:U ratio for the sample was 2.01), thereby relieving lattice strain.

During the second stage, the lattice parameter began to increase (beyond the first-stage plateau) again as a function of dose. A maximum was reached between 1 × 10^{17} and 5 × 10^{17} fissions/cm^3. The differences between the first two stages are attributed to the formation of different types of defects during these stages. However, the nature of these defects was not identified.

During the third stage, the lattice parameter decreases (from the maximum reached in the second stage) with further increases in dose. This change was attributed to the recovery of defects by annihilation of mobile interstitials as more vacancies are produced.

Matzke (1982) discusses radiation damage to crystalline insulators, oxides, and ceramic nuclear fuels. In particular, he points out key differences between metals and insulators with respect to radiation damage. First, insulators, such as UO_2, have a large difference in atomic number for the components that make up the lattice. As a result, partitioning of nuclear and electronic stopping power is different for the sublattices (i.e., in the uranium and in the oxygen). Secondly, the formation of charged defects in insulators results in complex forces between defects; as a result, defect mobility may be affected. Thirdly, bulk thermal effects are more likely to occur in insulators because of low thermal and electronic conductivities.

Matzke (1982) provides information on the effects of different radiation sources (e.g., alpha particles and fission products) on damage to lattices. For example, 5-MeV alpha particles have a range of about 10 μm in UO_2 (i.e., an energy loss rate of about 5×10^8 keV/m). The alpha particles lose their energy primarily through electronic interactions, and there are about 100 to 200 displaced atoms per alpha particle. By contrast, the recoil nucleus, produced in alpha decay, has an energy of about 100 keV. The range of the recoil nucleus in UO_2 is about 200 Å (for an energy loss rate of 5×10^9 keV/m), and about 1,500 displaced atoms are produced per recoil nucleus. Interactions with the recoil nucleus are primarily nuclear (i.e., energy is given to the lattice). The recoil nucleus produces a denser defect track than does the alpha particle. In fact, almost 90% of the damage in alpha decay is caused by the recoil nuclei.

Similar to alpha particles, fission products have a range of about 6 to 8 μm in UO_2. Thermal spikes {i.e., localized heating along the track [Lustman (1961)]} enhance the recombination of defects. The saturation level of fission-product-produced point defects is about a factor of 10 less than that for alpha particles.

Lustman (1961) describes a natural phenomenon regarding structural changes in some minerals. This condition, termed the "metamict state," occurs in minerals that either contain or are near uranium or thorium. The content of uranium or thorium may be very low. For example 0.41% ThO_2 in some minerals can cause metamictization (Pabst 1952).

Metamict minerals exhibit a number of characteristics. These include a loss of optical birefringence and little or no coherent X-ray diffraction, the reconstitution of the crystalline structure during heating of the material, heat release during recrystallization, and an increase in density as the material is heated. These are general characteristics that are seen in most, but not all, metamict materials (Pabst 1952).

The damage to the crystalline structure of metamict minerals is attributed to the energy deposited in the crystal by the radioactive decay of either uranium or thorium. The majority of the damage is caused by the recoil nucleus that results from alpha decay. Lustman states that the volume changes associated with the metamictization of some minerals is large enough such as to shatter other minerals that encase the metamict mineral.

Some minerals maintain their structure despite large doses. In particular, uraninite (UO_2) is structurally unaffected by the large doses to which it is subjected. However, weathered uraninite containing uranium that has been oxidized to higher valence states (i.e., UO_2 that has been oxidized to U_3O_8) is usually found in the metamict condition.

Complete metamictization of a mineral takes a very long time. For example, Pabst (1952) estimates that it would take more that 100,000 years to completely metamictize gadolinite ($Y_2FeBe_2Si_2O_{10}$) that contains 0.41% ThO_2. If, instead, the mineral contains about 1% uranium, Pabst estimates that complete metamictization would require about 12,000 years. However, a key assumption in these calculations is that all of the decay energy goes into disruption of the crystal lattice. Because this assumption is not likely, the time required for complete metamictization would be much longer than that given by the estimates.

3. EXPERIMENTAL

The radiolysis experiments that were performed are described in this section. Additionally, the techniques used to analyze both gas and solid samples are discussed.

Experiments on the radiolysis of fluorides in uranium oxides were performed to obtain information not available in the literature. The objectives of these experiments were to evaluate:

- radiolytic products and their production rates
- chemical or physical effects on the irradiated materials
- effects of varying parameters, which include
    - —initial fluoride content (e.g., vary from pure UO_2F_2 to U_3O_8 containing some known level of fluoride)
    - —chemical form (e.g., UO_2F_2, U_3O_8)
    - —dose and dose rate
    - —water content
    - —atmosphere in irradiation container

Additionally, the effects on containers and metal sample coupons used in the experiments were observed.

Two different sources of gamma radiation were used: (a) the ORNL ^{60}Co irradiator and (b) HFIR SNF elements. After their irradiation, gas and solid samples were taken and analyzed. In Sects. 3.1 and 3.2, the irradiation facilities are described.

Associated with each of these facilities are the details of the specific experimental configuration used (e.g., sample containers and their preparation, data acquisition, and the types of materials irradiated). In Sect. 3.3 an overview of the analytical techniques used to evaluate the gas and solid samples is presented.

3.1 ^{60}Co IRRADIATION EXPERIMENTS

The ORNL ^{60}Co irradiator (emitting 1.173-MeV and 1.332-MeV gamma rays, 5.271-year half-life, specific activity = 2.6016 MeV/disintegration) was used to provide a gamma radiation field with a dose rate of about 10^5 rad/h. Details are provided in Sects. 3.1.1 through 3.1.4 on the irradiator, sample containers, the data acquisition system, and the materials irradiated.

3.1.1 ^{60}Co Irradiator

A J. L. Shepherd Model 109-68 (Serial No. 654) ^{60}Co gamma irradiator was used for the experiments (Fig. 3.1). Sources, doubly encapsulated in type-300-series stainless steel, radially surround the cylindrical irradiation chamber, which is also constructed with 300-series stainless steel and has a 170°-wide closure door, which is used for loading and unloading samples. The dimensions of the chamber are 15.24 cm (6 in.) in diameter and 20.32 cm (8 in.) high. A photograph of the irradiation chamber with sample containers installed is shown as Fig. 3.2. A 3.18-cm (1.25-in.) diam opening at the top of the chamber leads to an access tube (of the same diameter) that is provided for inserting tubing or wiring. A hinged scatter shield is located on top of the access tube. This shield

Fig. 3.1. ORNL ^{60}Co irradiator.

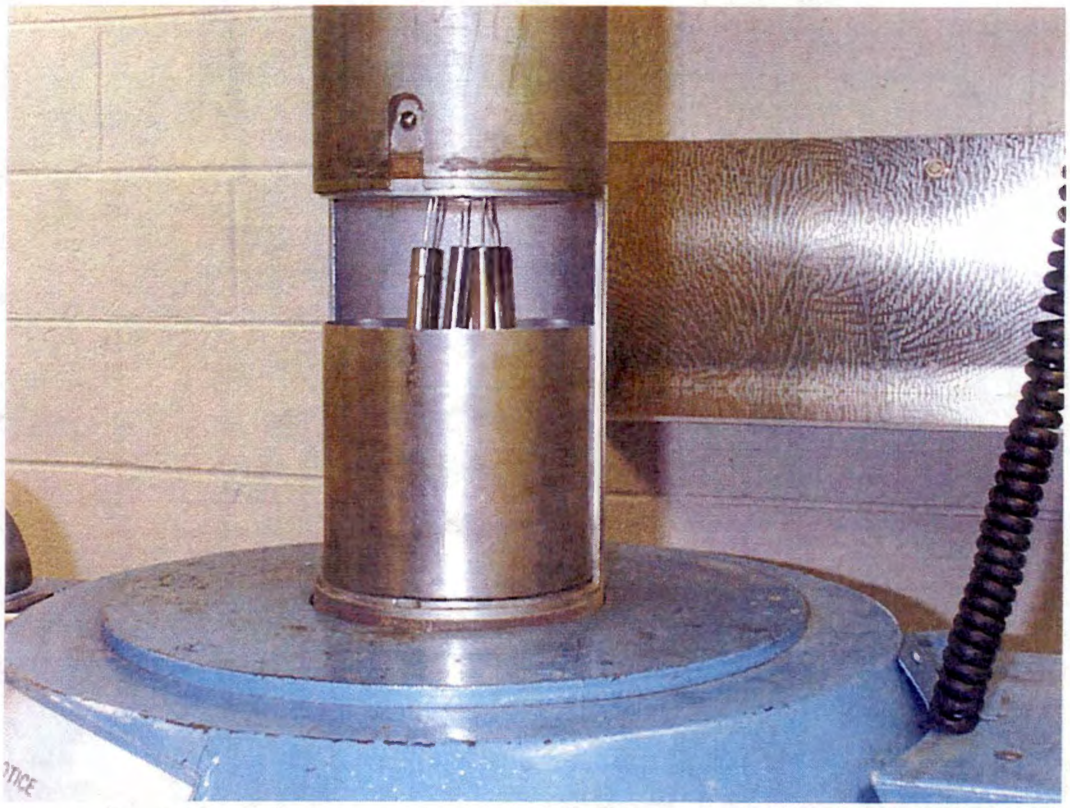

Fig. 3.2. Irradiation chamber of ORNL ^{60}Co irradiator with sample containers installed.

may be moved aside when the irradiator is in the "load" position (i.e., samples are not being irradiated); allowing researchers to feed tubes and wires into the chamber through the access tube. A 2.54-cm (1-in.) vertical clearance between the top of the access tube and the bottom of the scatter shield allows for connection of the tubes and wires to external equipment (e.g., pressure transducers or a data acquisition system) when the chamber is lowered into the "irradiate" position. Interlocks prevent the lowering of the chamber into the irradiate position with the scatter shield open. The design of the J. L. Shepherd irradiator permits a sample to be (a) irradiated under controlled temperatures and atmospheric conditions and (b) continuously monitored in either a flowing-gas system or by sensors (e.g., pressure transducers and thermocouples).

The exposure rate profile provided by the manufacturer for this particular irradiator is shown in Fig. 3.3. The reported exposure rate in the center of the irradiation chamber (i.e., the 100% rate) on December 9, 1977, was 1.85×10^6 R/h (Shepherd 1977). Unpublished exposure rate measurements made in 1982 and 1993 showed good agreement with the expected exposure rate from the manufacturer's data (Dillow 1998).

To evaluate radiolytic yields (i.e., the number of molecules of a species produced per amount of energy deposited in a material), the energy deposited in the irradiated material (i.e., the dose) must be known. Hence, the exposure rate (which is a measure of the amount of ionization produced in air by gamma or X rays) must be converted to a dose rate in the irradiated material. The method established in ASTM Standard E666-91 (ASTM E666-91 1991) was used to perform this conversion. This method is described in Appendix C, herein.

ORNL DWG 99C-58

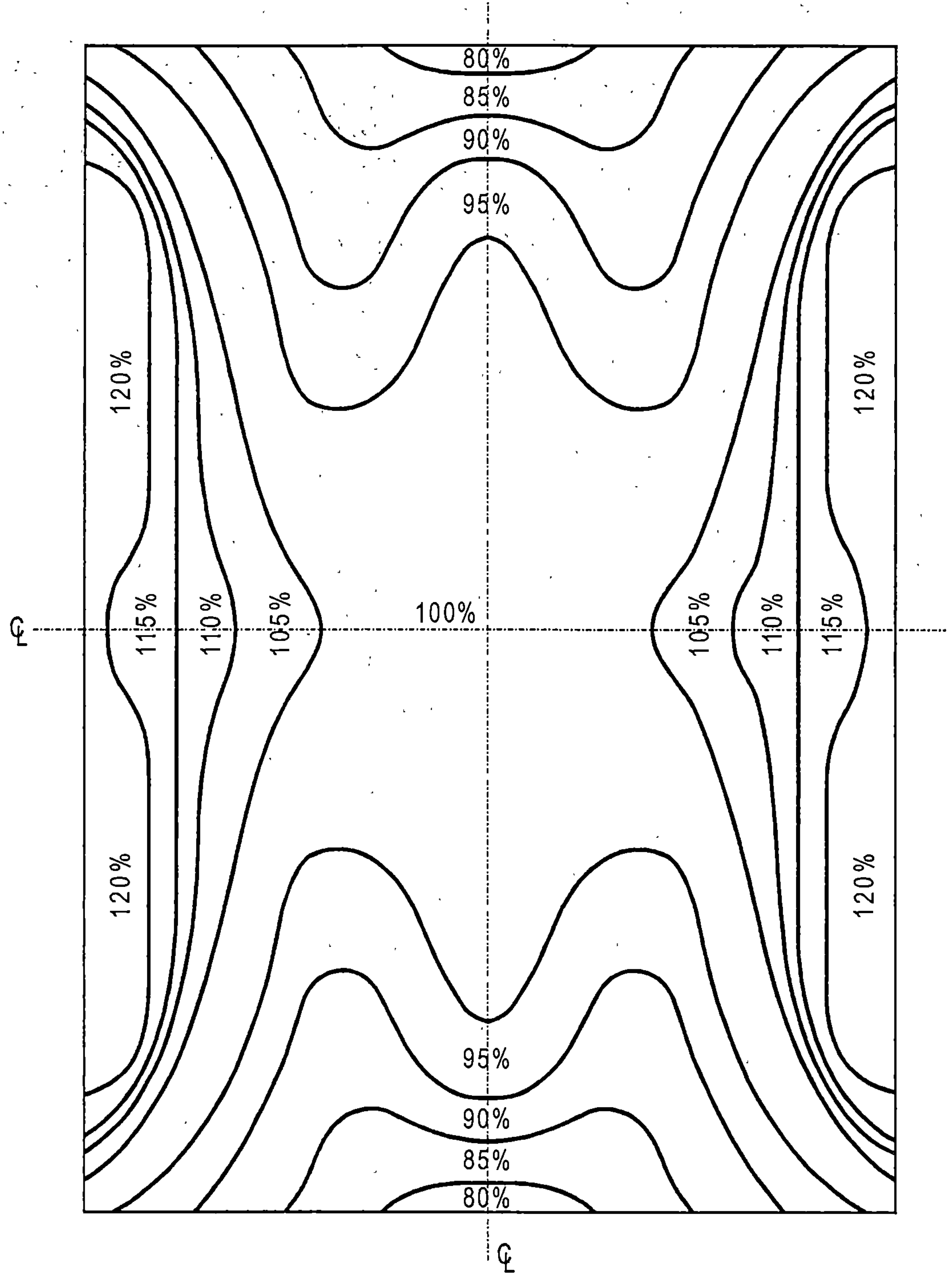

Fig. 3.3. Exposure rate profile for ORNL ^{60}Co irradiation chamber. (Reported 100% exposure rate on December 9, 1977, was 1.85×10^6 R/h) (after Shepherd 1977).

A 14.288-cm (5.625-in.) diam, 1.91-cm (0.75-in.) thick aluminum disk with 9 evenly spaced 2.54-cm (1-in.) diam holes was placed in the bottom of the irradiation chamber to hold sample containers. This holder ensured that the samples remained in a fixed position throughout their insertion into and removal from the irradiate position. Additionally, because the dose rate varies as a function of both the axial and radial position in the chamber (Fig. 3.3), the holder provided a convenient means by which to index the sample container position. As it turned out, the configuration of the containers resulted in the irradiated materials being located in the 100%-exposure-rate region of the chamber.

3.1.2 Sample Containers

Sample containers, instrumented with pressure transducers, provided for the real-time monitoring of pressure inside the container and for withdrawing gas samples at the end of an irradiation. The interior volume of the containers and associated components (i.e., tubing, fittings, valves, and pressure transducers) were minimized inasmuch as practicable to provide greater sensitivity to pressure changes within the container.

The samples to be irradiated were placed in stainless steel containers, each of which had a small-diameter nickel tube connected at one end for pressure sensing and a capped opening at the other end for loading samples (Fig. 3.4). The sample containers were constructed from 11.75-cm (4.625-in.) long, 1.27-cm (0.5-in.) diam type 304L stainless steel tubing. The wall thickness of the tubing was 0.089 cm (0.035 in.). One

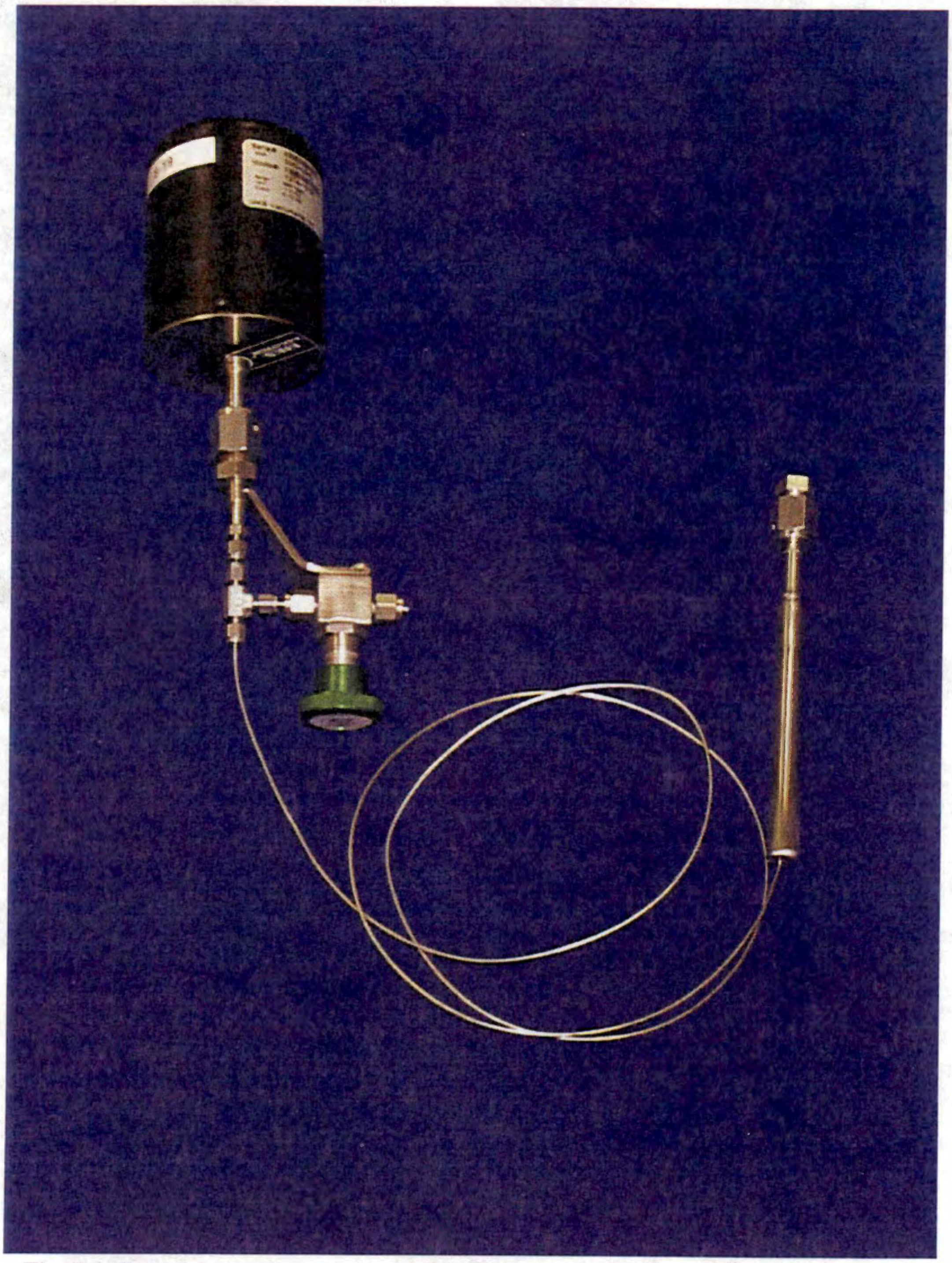

Fig. 3.4. Sample container and pressure transducer used in the ^{60}Co irradiations.

end of the tube was welded closed with a 1.27-cm (0.5-in.) diam, 0.159-cm (0.0625-in.) thick stainless steel disk. A hole in the center of the disk was connected to 0.159-cm (0.0625-in.) diam nickel tubing [~ 84-cm (33-in.) long]. A small disk of 100-mesh monel was placed inside the sample container and over the hole leading to the nickel tubing. This mesh prevented the movement of particles from the sample container into the tubing. The sample tubing was connected to a 0.159-cm (0.0625-in.) stainless steel Swagelok® tee. The tee was then connected to (1) a 0.318-cm (0.125-in.) stainless steel Nupro® valve with Swagelok fittings [using a 0.318-cm (0.125-in.) to 0.159-cm (0.0625-in.) reducing fitting] and (2) a 0.635-cm (0.25-in.) Cajon® VCR gland [using a 0.635-cm (0.25-in.) to 0.159-cm (0.0625-in.) reducing fitting] with a male Cajon VCR nut. The valve was connected such that the metal valve seat (vs the valve bellows) isolated the pressure-sensing line. The valve was capped with a 0.318-cm (0.125-in.) Swagelok plug, except during container preparation (e.g., leak checks and fluorination) and sampling operations. The Cajon gland was used to mate the sample tubing to a MKS Baratron® pressure transducer (Type 127A). These transducers were custom-made with 0.635-cm (0.25-in.) Cajon VCR glands to minimize volume. A nickel gasket was used to seal the connection between the two Cajon glands.

The other end of the stainless steel tubing was welded to a 0.635-cm (0.25-in.) stainless steel VCR gland with a female nut. Material to be irradiated was loaded through this gland into the container. A VCR plug and nickel gasket were used to close the opening in the sample tube. The overall length of the sample container [excluding the added length of the 0.159-cm (0.0625-in.) nickel tubing] was 17.8-cm (7-in.). Each container was etched with an unique number for identification. [Note that the first two containers used in the irradiations (S-1 and S-2) were fabricated such that the loading end was closed with a 1.27-cm (0.5-in.) Swagelok cap (see Table 3.1). However, after one of the containers leaked, the design of the loading end was changed to the 0.635-cm (0.25-in.) Cajon gland.] One of the sample containers, S-8, was not fitted with the sampling tubing and pressure transducer. This arrangement allowed only for withdrawal of gas samples at the end of an experiment, but not for pressure monitoring.

Preparation of sample containers for their insertion into the ^{60}Co irradiator consisted of leak checks, volume measurements, fluorination, and loading of the samples into the containers. As part of their fabrication, the containers were leak-checked with air to a pressure of about 6.8 atm (100 psia). Just before their use, the containers were leak-checked again using both pressure (typically ~3 atm) and vacuum. The volume of the irradiation rig (i.e., the sample container, tubing, valve, and pressure transducer) was measured by expanding helium from a known volume into the rig, observing the pressure change, and applying the ideal gas law. The results of the volume measurements are presented in Table 3.1.

The sample rig was treated with fluorine to passivate the system. Typically, the empty sample rig was evacuated, and then 50–100 Torr of F_2 was introduced into the rig. A heat gun was then used to heat all of the surfaces of the rig to promote reaction. After about 1 h, the F_2 was evacuated through a soda-lime trap. Then, 500–600 Torr of F_2 was introduced into the rig, and the heating was repeated. After several hours, the F_2 was evacuated through a soda-lime trap, and the rig was backfilled with helium.

Table 3.1. Volume measurements of irradiation containers as determined by gas expansion method

Container	Volume (cm^3)
Calibrated volume[a]	153.9 ± 0.07
S-1[a,b]	20.0 ± 0.1
S-2[a,b]	19.9 ± 0.1
S-3[c]	16.3 ± 2.0
S-4[c]	15.9 ± 2.1
S-8[c,d]	13.5 ± 2.1
S-12[e]	17.1 ± 0.04
S-13[e]	16.6 ± 0.04
S-16[e]	15.7 ± 0.04
S-17[e]	15.8 ± 0.05
S-20[e]	15.6 ± 0.04
S-21[e]	15.6 ± 0.04
S-22[e]	15.9 ± 0.04
HFIR-1,2[c,f]	70.5 ± 2.2

[a] Measured by weight of water required to fill volume.

[b] S-1 and S-2 were equipped with 1.27-cm (0.5-in.) Swagelok fittings on the loading end, while all others (except HFIR-1 and 2) were equipped with 0.635-cm (0.25-in.) Cajon fittings.

[c] Used manifold transducer with estimated accuracy of ±0.25% of reading (manufacturer's specification).

[d] S-8 was not fitted with sensing tubing and a pressure transducer.

[e] Used transducer attached to container. Estimated accuracy ±0.07% of reading based on transducer calibration data.

[f] The same container was used for the HFIR SNF experiments (i.e., HFIR-1 and HFIR-2).

Samples were loaded with either an inert (helium) or air atmosphere in the container. To obtain the inert atmosphere, the rig was first placed inside an inert atmosphere glove box. Typically, the glove-box atmosphere contains less than 1 ppm O_2 or moisture. The loading end of the sample container was opened, the container was filled with the desired amount of sample, and then the container was resealed. The irradiation rig was then removed from the glove box. For an air atmosphere, the sample was simply loaded into the container in the laboratory atmosphere (in a radiochemical hood).

3.1.3 Data Acquisition System

A computerized data acquisition system was used to collect data during each irradiation (Fig. 3.5). Validyne® hardware and software were used, providing up to eight data channels per card. Other locally developed software* and a MicroSoft® web server, made the data available continuously over the world wide web. Typical parameters recorded during an irradiation included container pressure, temperature of selected containers, and room pressure and temperature.

Omega® Type K thermocouples and MKS Baratron Type 127A pressure transducers were used to measure temperature and pressure, respectively.

---

* Battle, R. E., 1998. Software program developed to interface with a Validyne output file and a Microsoft Web Server, Lockheed Martin Energy Research Corp., Oak Ridge National Laboratory, Oak Ridge, Tennessee.

Fig. 3.5. Photograph of data acquisition computer in operation at the ORNL ^{60}Co source.

3.1.4 Materials Irradiated

$UO_2F_2 \cdot xH_2O$ is an intermediate compound formed during the conversion of UF_6 to U_3O_8. During conversion processing, the UO_2F_2 – uranium oxide mixture is heated in 50°C steps and contacted with pressurized steam (see Appendix B). Ferris and Baird (1960) found that uranyl fluoride was stable in a dry atmosphere below 700°C. Above 700°C, the uranyl fluoride was found to slowly decompose according to the following reaction:

$$3UO_2F_2 \rightarrow UF_6 + \tfrac{2}{3}U_3O_8 + \tfrac{1}{3}O_2. \qquad (3.1)$$

Treatment of the oxyfluoride with pressurized steam slowly removes the fluorine (as HF), thus promoting the conversion to uranium oxide. First, the UF_6 (produced by the decomposing UO_2F_2) reacts with the water to form UO_2F_2 and HF, as shown in the following reaction:

$$UF_6 + 2H_2O \rightarrow UO_2F_2 + 4HF. \qquad (3.2)$$

The newly produced UO_2F_2 can then decompose [Eq. (3.1)] and the reaction, shown in Eq. (3.2), is then repeated. This cycle continues, slowly reducing the amount of oxyfluoride in the material. Based on this reaction scheme, it is reasonable to expect that the residual fluoride remaining in the U_3O_8 after conversion is of the form UO_2F_2. It is therefore important to understand radiolytic effects on UO_2F_2, because studying this material provides a bounding case for the maximum amount of fluoride that could be in the converted product. Additionally, samples of U_3O_8 (with a known residual fluoride content), produced by the conversion process, were irradiated. The irradiation of this material simulated the radiolysis of the uranium oxides to be placed in storage.

Two sources of $UO_2F_2 \cdot xH_2O$ were used in the experiments: (1) $UO_2F_2 \cdot xH_2O$, which was produced at ORNL by the hydrolysis of UF_6, and (2) material obtained from the East Tennessee Technology Park (ETTP), Oak Ridge, Tennessee. Either DU or natural uranium was used in each of the samples. The production of $UO_2F_2 \cdot xH_2O$ was essentially the first step of the conversion process (Del Cul, Icenhour, and Toth 1997; see Appendix B). Initially, 375.9 g of UF_6 were transferred to a liquid-nitrogen-cooled vessel, where the UF_6 condensed. Then, 180 g of H_2O were added to the vessel, where it froze on top of the UF_6. The material was then allowed to slowly warm. As the water began to melt, the hydrolysis reaction occurred (with the excess water forming hydrates):

$$UF_6 + (2 + x)H_2O \rightarrow UO_2F_2 \cdot xH_2O + 4HF . \tag{3.3}$$

The vessel was then evacuated through a soda-lime trap for 5 d to remove the HF and excess moisture. This treatment resulted in the production of $UO_2F_2 \cdot 1.7H_2O$. Some of this material was pulverized, spread out in a thin layer, and then further evacuated for an additional 13 d. This treatment resulted in the production of a lower hydrate: $UO_2F_2 \cdot 0.4H_2O$. The higher hydrates of uranyl fluoride (e.g., $UO_2F_2 \cdot 1.7H_2O$) are distinctively bright yellow. Anhydrous UO_2F_2 is tan. The $UO_2F_2 \cdot 0.4H_2O$ was tan and yellow. Infrared analysis of this material indicated the presence of both hydrated and anhydrous UO_2F_2 (see Appendix D).

Material obtained from ETTP consisted of $UO_2F_2 \cdot 1.4H_2O$ and $UO_2F_2 \cdot 0.4H_2O$. The history of the production of these materials was unknown. However, attenuated total reflectance (ATR) analysis confirmed that the materials were hydrated uranyl fluoride (see Appendix D). A sample of $UO_2F_2 \cdot 2.3H_2O$ was prepared by placing some $UO_2F_2 \cdot 1.4H_2O$ in a 97 % humidity desicator.

The amount of hydration of each of the materials used in the experiments was determined by thermal gravimetric measurements and by mass-balance calculations from the results of the Davies-Gray titrations.

Some samples of $UO_2F_2 \cdot xH_2O$ were further treated by heating in a controlled atmosphere (e.g., O_2). An apparatus similar to that depicted in Fig. 3.6 was used in the treatment. A sample to be treated was first placed in an alumina boat, which, in turn, was inserted into a silica tube. The tube was contained inside a clamshell furnace. The tube was configured such that the desired cover gas could be supplied at one end, while gas samples could be withdrawn from the other end into a Fourier Transform Infrared (FTIR) gas cell to obtain an infrared spectrum. A pressure transducer was used to monitor the pressure in the apparatus. Although the configuration was such that the heat treatment could be performed either as a flowing gas or batch system, all heat treatments used the batch mode.

3.2 HFIR SNF IRRADIATION EXPERIMENTS

To obtain higher dose rates, the HFIR SNF gamma irradiation facility, which is located at ORNL, was also used. Details on the irradiation facility, containers, data acquisition, and the materials irradiated are provided in Sects. 3.2.1 through 3.2.4.

ORNL DWG 99C-6861

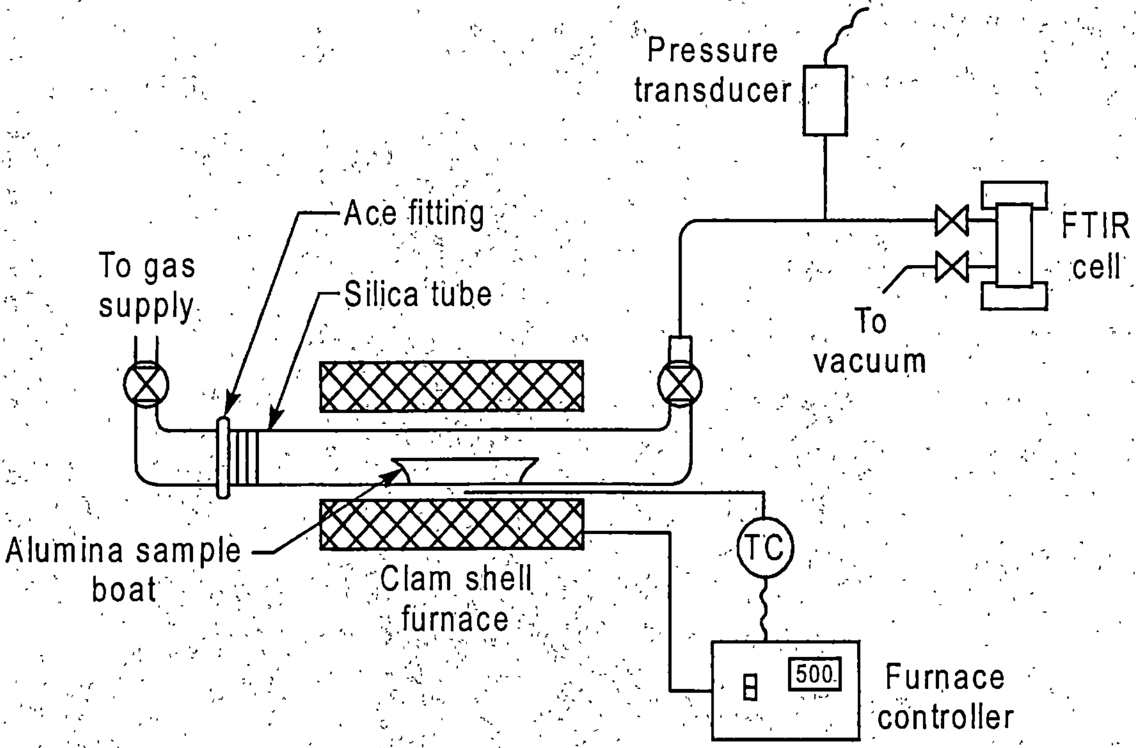

Fig. 3.6. Apparatus used to heat $UO_2F_2 \cdot xH_2O$ samples in a controlled atmosphere.

3.2.1 HFIR SNF Irradiation Facility

Samples can be irradiated in the HFIR SNF pool by inserting them inside SNF elements (Fig. 3.7). The SNF elements are cylindrical with a hollow center. In its storage position in the SNF pool, a cadmium sleeve inside the hollow region of the element absorbs neutrons. Hence, the hollow region of the fuel element primarily provides a gamma field for irradiation. Variable gamma-radiation fields are available based on the decay times of the elements. The facility provides a nominal 7.62-cm (3-in.) opening for placing the samples inside the SNF elements. Reported exposure rates range from about 10^8 down to 10^7 R/h or lower, depending on the time since the discharge of the SNF from the reactor. The gamma-ray energy spectrum for a HFIR SNF element 1 d after discharge from the reactor is shown in Table 3.2 (Williams, Del Cul, and Toth 1996).

Kohring (1986) measured the exposure rate inside HFIR SNF elements as a function of (1) axial location within the element and (2) time since discharge from the reactor. These measurements were made for elements that had been operated at 100 MW for 21.5 d (i.e., 2150-MWd burnup). Figure 3.8 shows the peak exposure rate as a function of time since shutdown (Kohring 1986). This exposure rate can be corrected for the axial location of the sample by use of Fig. 3.9, which is adapted from Kohring (1986). In 1987, HFIR operating power was reduced to 85 MW. This reduced power level necessitated an adjustment in the reported exposure rates and such an adjustment was calculated by Kohring (1987). Kohring used the ORIGEN computer code to calculate correction factors that needed to be applied to the measured exposure rates to account for

Fig. 3.7. SNF elements in the HFIR SNF pool.

Table 3.2. Gamma-ray energy spectrum for a HFIR SNF element 1 day after discharge from the reactor[a]

Energy group	Upper bound (MeV)	Average energy in group (MeV)	Percentage of total energy in group
1	0.02	0.01	0.44
2	0.03	0.025	0.44
3	0.045	0.0375	0.89
4	0.07	0.0575	0.56
5	0.1	0.085	1.04
6	0.15	0.125	2.66
7	0.3	0.225	5.66
8	0.45	0.375	4.48
9	0.7	0.575	26.94
10	1	0.85	26.82
11	1.5	1.25	6.89
12	2	1.75	21.06
13	2.5	2.25	0.88
14	3	2.75	1.24
15	4	3.5	0.01
Average energy = 0.93 MeV			

[a] Williams, D. F., G. D. Del Cul, and L. M. Toth, 1996. *A Descriptive Model of the Molten Salt Reactor Experiment After Shutdown: Review of FY 1995 Progress*, ORNL/TM-13142, Oak Ridge National Laboratory, Oak Ridge, Tennessee, January.

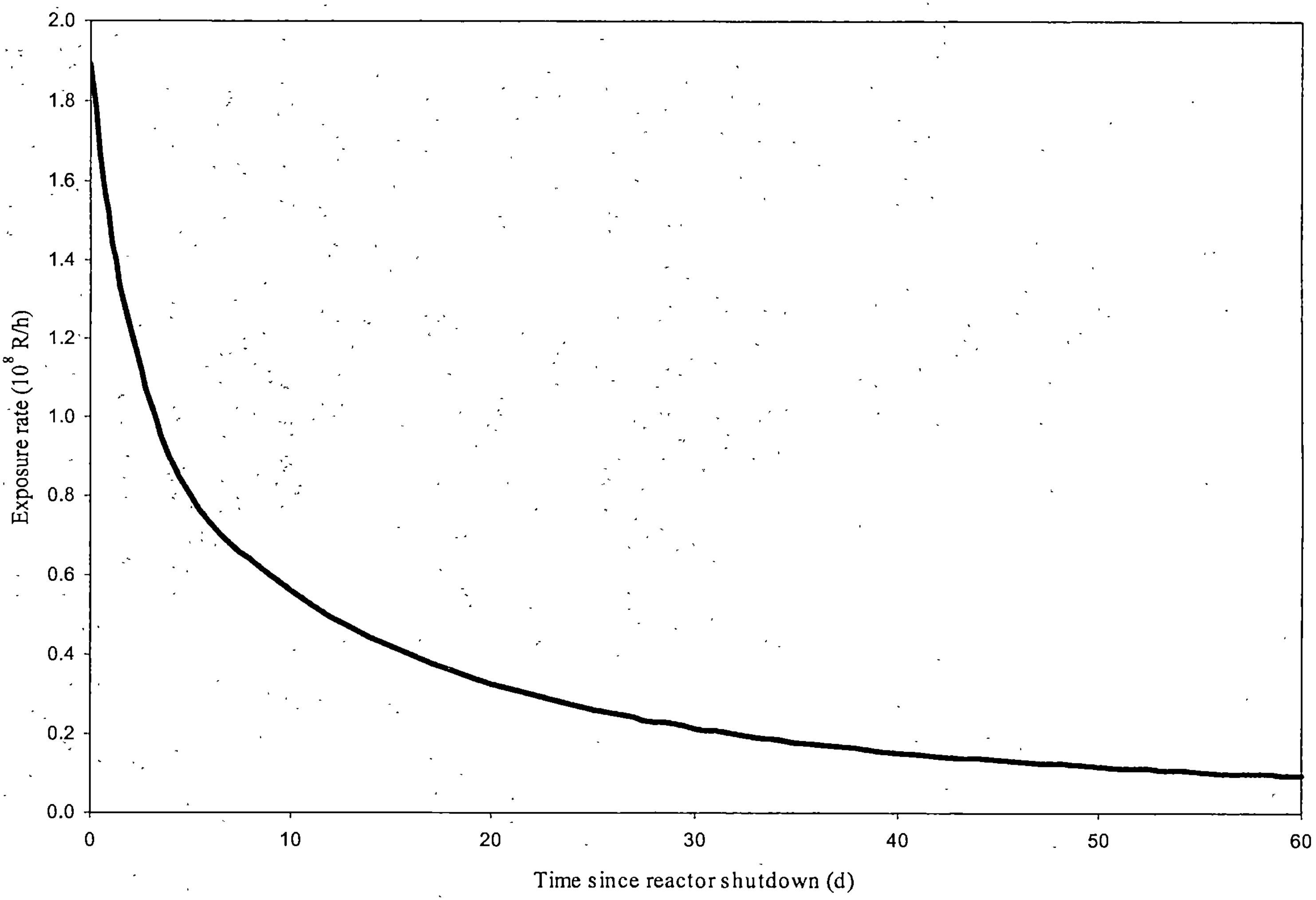

Fig. 3.8. Peak exposure rate in a HFIR SNF element as a function of time since reactor shutdown (adapted from Kohring 1986).

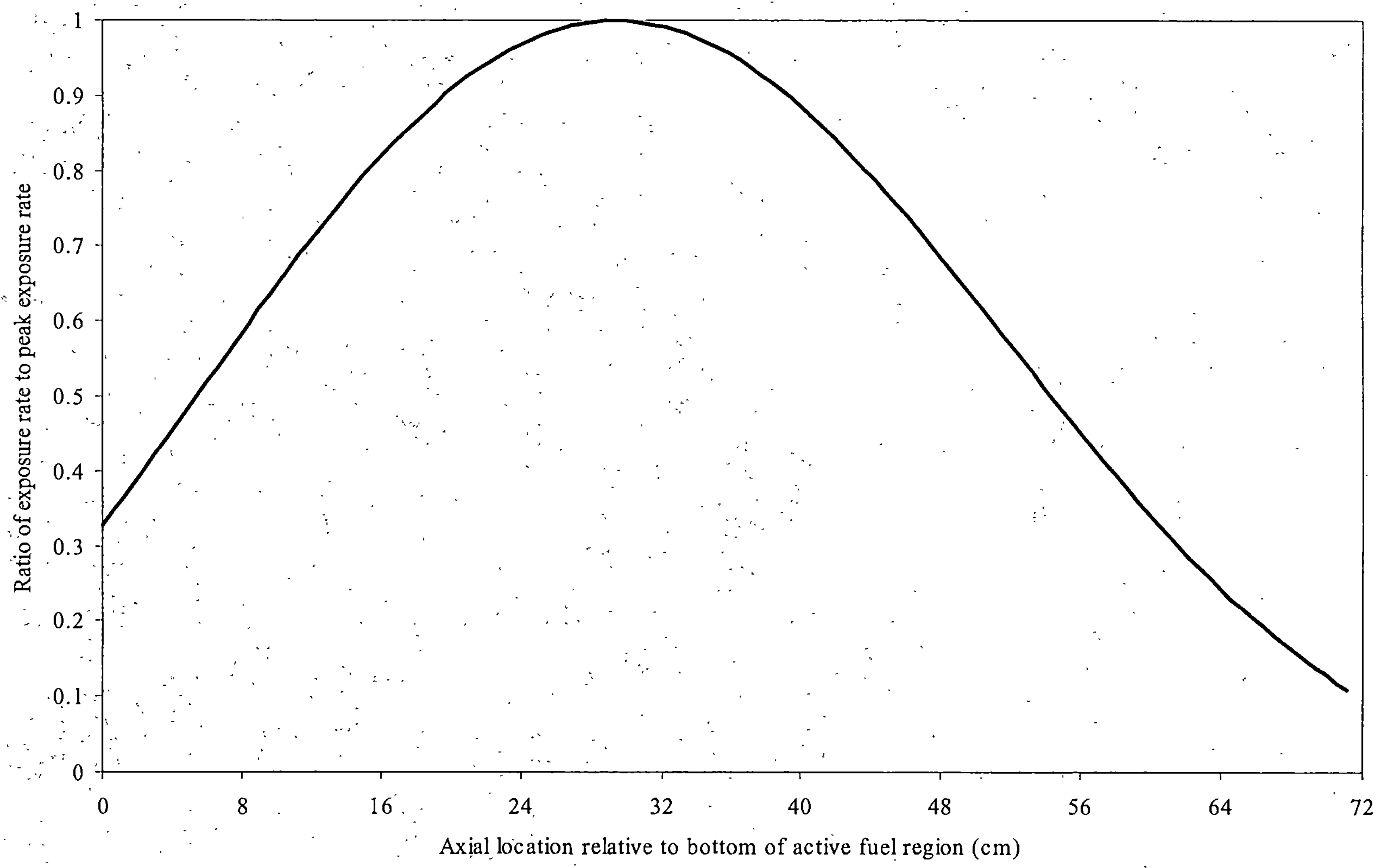

Fig. 3.9. Exposure rate relative to the peak exposure rate as a function of axial position in a HFIR SNF element (adapted from Kohring 1986).

the decreased operating power. These correction factors can also be calculated by use of the Borst-Wheeler formula (Lamarsh 1966), which has been shown to be in good agreement with the correction factors reported by Kohring (Hobbs 1995). The correction factor is calculated by:

$$CF(t) = 0.85\frac{\left(t^{-0.2} - (t + T)^{-0.2}\right)}{\left(t^{-0.2} - (t + 21.5)^{-0.2}\right)} \;, \tag{3.4}$$

where

$CF(t)$ = correction factor at time t after shutdown (unitless),

t = time since shutdown (d), and

T = time of operation at 85 MW [= Burnup(MWd)/85 MW] (d).

The factor 0.85 is simply the ratio of the new operating power level (85 MW) to the original operating power level (100 MW). To evaluate the dose rate to a sample, the exposure-rate data provided by Kohring are adjusted based on the burnup of the element and the axial location of the sample. The exposure is then converted to dose based on the method described in Appendix C.

3.2.2 Sample Container

The container placed in HFIR SNF elements has been used in a number of radiolysis experiments on MSRE-type salts (Toth and Felker 1990, Williams, Del Cul, and Toth 1996). This container (Fig. 3.10) was fabricated from a 2.54-cm (1-in.) diam, 8.9-cm (3.5-in.) long nickel tube, which is sealed at one end with nickel plate and has a Conflat® flange at the other end. A hole in the flange was connected to 6.1 m (20 ft) of

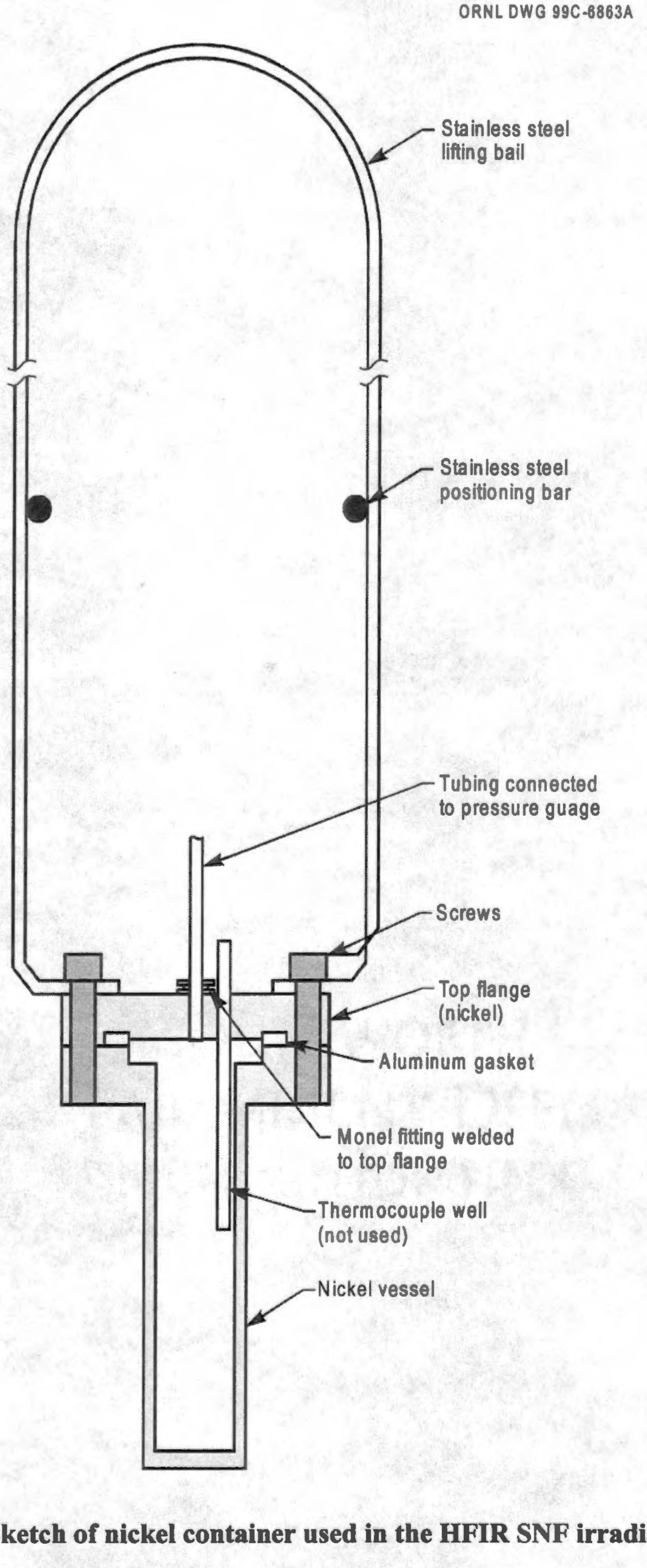

Fig. 3.10. Sketch of nickel container used in the HFIR SNF irradiations.

0.318-cm (0.125-in.) diam monel tubing, which was then connected to an Ashcroft® compound pressure gage and a valve for withdrawing gases.

Before the container was used, its volume was measured (Table 3.1), and the container was then passivated with fluorine using a procedure similar to that described in Sect. 3.1.2. Samples were loaded into the container through the flanged end in an inert-atmosphere glove box. The flange was then sealed with an aluminum gasket. Before the container was sent to HFIR for its insertion into an SNF element, the pressure in the container was increased to 1.68 ± 0.07 atm (10 ± 1 psig) with helium because of requirements imposed by HFIR personnel to maintain the container pressure greater than the water pressure in the pool. A sketch of the experimental configuration used for irradiation of samples in HFIR SNF elements is shown in Fig. 3.11.

A lifting bail attached to the flange was used to direct the container into position in the SNF element. Positioning rods on the lifting bail held the sample about 37 cm (14.5 in.) above the bottom of the active region of the fuel element.

3.2.3 Data Acquisition System

In contrast to the computerized data acquisition system that was used for the ^{60}Co experiments, a monel Bourdon pressure gage was used for the HFIR SNF irradiations. The pressure gage and a valve were attached to a mounting bracket, which was clamped to the edge of the SNF pool wall (Fig. 3.11). The container was then inserted into an SNF element, and HFIR operations personnel periodically recorded the container pressure.

ORNL DWG 99C-487

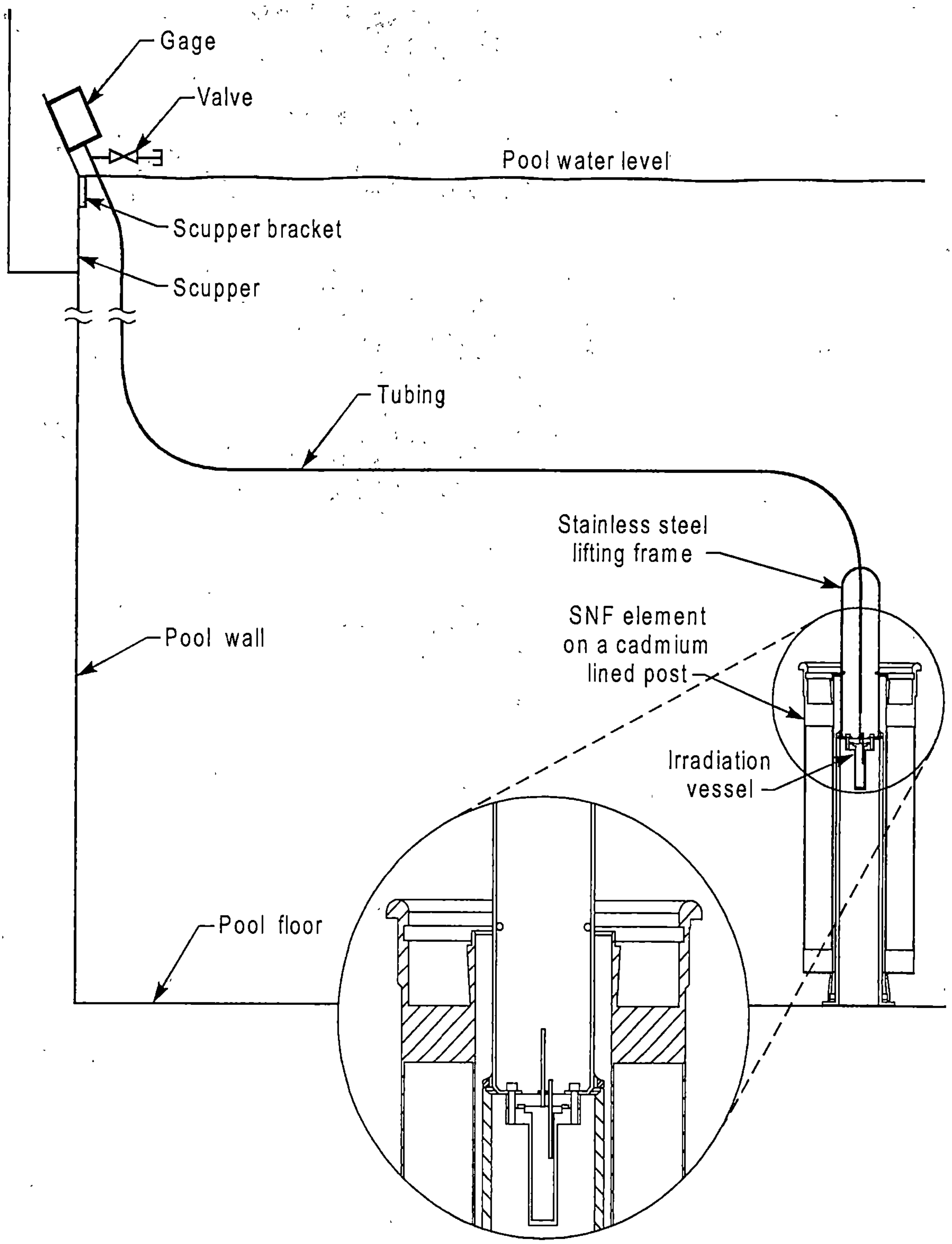

Fig. 3.11. Sketch of the experimental configuration for gamma-irradiation experiments with a HFIR SNF element.

3.2.4 Materials Irradiated

The sources of the materials used in the HFIR irradiation experiments are the same as those described in Sect. 3.1.4. Additionally, in one experiment (HFIR-2), types 304, 304L, 316, and 316L stainless steel metal coupons were placed inside the container, along with the sample to be irradiated, to evaluate corrosion effects.

3.3 SAMPLING AND ANALYSES

Besides recording gas pressure during an irradiation, a number of gas and solid samples were taken and analyzed after completion of the irradiation. The sampling technique and the analyses performed are described in Sects 3.3.1–3.3.3.

3.3.1 Sampling Technique

To withdraw gas samples, the irradiation rig was connected to a sampling rig (Fig. 3.12), which consisted of a sample cylinder for mass spectrometry (MS) connected in series to a 10-cm FTIR gas cell. Zinc selenide windows were used in the FTIR gas cells. The MS sample cylinder was fabricated from 0.635-cm (0.25-in.) diam, 7.62-cm (3-in.) long stainless steel tubing with 0.635-cm (0.25-in.) stainless steel Nupro valves welded to each end. Each valve had a 0.635-cm (0.25-in.) Cajon gland with a female nut, which was used to connect the sample cylinder to either an FTIR gas cell, the irradiation rig, or a mass spectrometer. The volume of the sampling rig was about 60 mL.

The gas-sampling procedure consisted of first evacuating the sampling rig. Then, with the vacuum source isolated, the valve on the irradiation rig was slowly opened

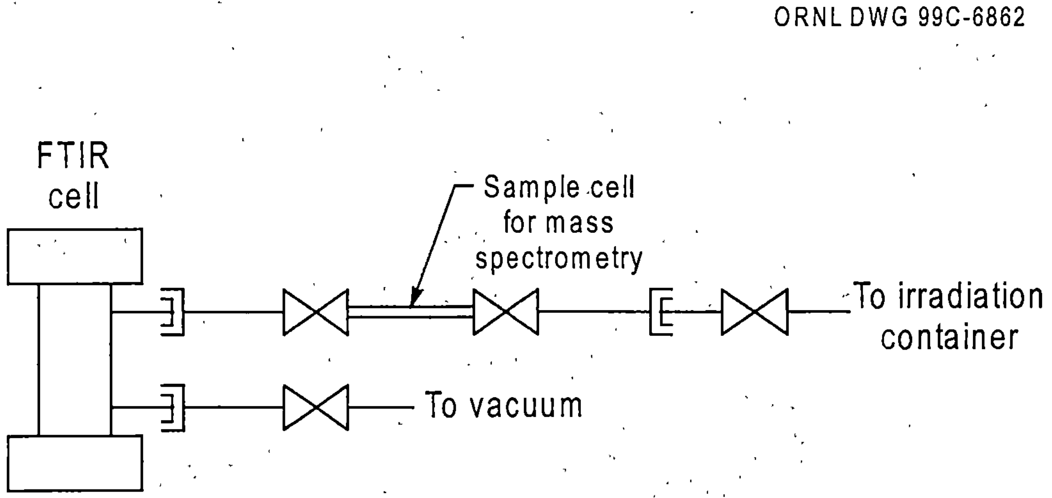

Fig. 3.12. Sampling rig used to withdraw gas samples from the irradiation container.

to expand the gas from the irradiation rig into the sample rig. All valves were then closed, thus isolating the gas in the MS cylinder and the FTIR cell. FTIR analyses were immediately performed on the gas, while the MS cylinder was sent to a laboratory at the Y-12 Plant in Oak Ridge, Tennessee, for analysis.

3.3.2 Gas Analyses

Gas samples were analyzed by MS and FTIR spectroscopy to identify the composition of the gas.

3.3.2.1 Mass Spectrometry

Mass spectrometry provides a quantitative analysis of the constituents of the gas sample. The sample is first ionized; then the ions are separated by electric and magnetic fields into groups of equivalent mass-to-charge ratio. This separation produces a mass spectrum, which is characteristic of the species present and the relative amounts of each species (Sibilia 1988).

3.3.2.2 FTIR Spectroscopy

A sample that is placed in an infrared beam will absorb radiation at frequencies that correspond to, among other vibrations, the frequencies of internal vibrations of the molecules in the sample. An infrared spectrum can then be obtained by plotting the absorbed energy vs frequency. The unique spectra, generated for different molecules, enable the identification of the types of molecules in a sample. Furthermore, the frequencies of the absorptions for a particular molecule give insight into the structure of the molecule (Sibilia 1988). Homonuclear diatomic molecules such as H_2, F_2, O_2, and N_2 are infrared inactive and thus do not absorb infrared radiation; so other techniques (e.g., mass spectrometry) must be used to identify them.

The absorption intensity of a specific frequency by a species is related to the concentration, as shown by Beer's law:

$$A = \epsilon c l, \tag{3.5}$$

where

A = absorbance (dimensionless),

ϵ = molar absorptivity (M^{-1} cm^{-1}),

c = concentration (M), and

l = light path length (cm).

Hence, a calibration of concentration vs absorbance at a specific frequency can be used to quantify the amount of a given species that is present in a sample.

3.3.3 Solids Analyses

Solid samples were analyzed by a number of techniques including visual, X-ray diffraction (XRD), X-ray photoelectron spectroscopy (XPS), attenuated total reflectance (ATR), differential thermal analysis-thermogravimetric analysis (DTA-TGA), and Davies-Gray titration. These techniques are briefly described in the following subsections.

3.3.3.1 Visual

Samples that were removed from the irradiation containers were visually examined for changes in color or texture. The irradiation containers and, if present, metal sample coupons were examined for signs of corrosion. Some samples were sent for metallographic microscopic examination.

3.3.3.2 X-ray Diffraction

XRD provides information about the structure and composition of polycrystalline materials. When a beam of monochromatic X rays is directed at a crystalline material, a diffraction pattern can be observed at various angles relative to the incident beam. Bragg's law describes the relationship between X-ray wavelength, the diffraction angle, and the distance between atomic planes in the crystal lattice, namely:

$$n\lambda_l = 2d \sin\theta, \tag{3.6}$$

where

n = order of the diffraction, integer (n = 1, 2, ...),

λ_l = wavelength of the X rays (cm),

d = distance between each set of atomic planes (cm), and

θ = diffraction angle.

Crystalline materials have unique diffraction patterns that can be used to identify the material (Sibilia 1988).

3.3.3.3 X-ray Photoelectron Spectroscopy

XPS [also known as electron spectroscopy for chemical analysis (ESCA)] is used to obtain information about the surface composition and structure of a solid. Upon exposure to X rays of known energy, a solid will emit photoelectrons which originate from the discrete energy levels associated with atoms in the solid. The energy of these photoelectrons is given by the following equation:

$$E_K = h\nu - E_B - \phi , \tag{3.7}$$

where

E_K = photoelectron kinetic energy (eV),
$h\nu$ = incident X-ray energy (eV),
E_B = bonding energy of the core or valence electron (eV), and
ϕ = system dependent, adjustable factor (eV).

The spectrum for a given element is normally compromised of a series of peaks that correspond to photoelectron emissions from the different shells of an element. Hence, the spectrum can be used to identify the elemental composition at the surface of a solid. Finally, E_B is dependent on the oxidation state of the atom probed with the X rays. This variation in E_B is referred to as a chemical shift. Hence, the valence of the atoms at the surface of a solid can be identified by using XPS (Sibilia 1988).

3.3.3.4 Attenuated Total Reflectance

ATR provides an infrared spectrum for solid materials. The solid sample is placed in close contact with an ATR crystal (e.g., diamond). Infrared radiation enters one end of the crystal through a set of mirrors, and it is internally reflected until it exits the other end of the crystal. The internal reflections create an evanescent wave, which extends beyond the crystal surface into the sample. Part of the evanescent radiation is absorbed by the sample and an absorption spectrum, characteristic of the species present, is produced. (Pike 1999).

3.3.3.5 Differential Thermal Analysis—Thermogravimetric Analysis

DTA and TGA are used in conjunction to examine changes to a sample as a function of temperature or time. DTA is a technique that is used to study the thermal behavior of a material as it undergoes physical and chemical changes during heat treatment. As a substance is heated, physical and chemical transformations occur that involve either heat absorption (i.e., an endothermic process) or heat release (i.e., an exothermic process). DTA involves the measurement of the temperature difference between a sample and an inert reference as both materials are heated at the same rate. These temperature differences indicate (a) the endotherms and exotherms and (b) the temperatures at which these thermal changes occur.

TGA is a technique that measures and records changes in weight of a sample as a function of temperature. Alternatively, TGA may be performed at a constant temperature (i.e., isothermal TGA), and the weight change as a function of time is measured. TGA data provide information on the thermal stability, composition, and decomposition behavior of a material (Sibilia 1988).

3.3.3.6 Davies-Gray Titration

The amount of U and U(IV) in a sample can be determined by Davies-Gray titration (Jarabek 1984, Davies and Gray 1964, Eberle and Lerner 1971). The Davies-Gray analyses reported in this work were performed by Materials and Chemistry Laboratory, Inc., of Oak Ridge, Tennessee, using the method described by Jarabek (1984), which is a modification of the method originally reported by Davies and Gray (1964). The method used is described in the following paragraphs. For brevity, only the major reactions are shown, and the original references should be consulted for further detail.

The determination of total U is accomplished by first dissolving the sample in a 3-to-1 mixture of phosphoric acid, H_3PO_4, and water. Any U(V) that is present will disproportionate to U(IV) and U(VI). The U(VI) is then reduced to U(IV) by ferrous ions, as shown in the following reaction:

$$\mathrm{UO_2^{+2} + 2Fe^{+2}\,(excess) + 4H^+ \rightarrow U^{+4} + 2Fe^{+3} + 2H_2O + 2Fe^{+2}\,(excess).} \qquad (3.8)$$

This mixture is diluted with sulfuric acid, and vanadyl sulfate is added as a catalyst. The U(IV) can then be titrated by a standard potassium dichromate solution to a potentiometric endpoint between 590 and 650 mV. The titration reaction is given by

$$\mathrm{3U^{+4} + Cr_2O_7^{-2} + 2H^+ \rightarrow 3UO_2^{+2} + 2Cr^{+3} + H_2O.} \qquad (3.9)$$

The amount of U is calculated based on the amount and concentration of potassium dichromate used.

To determine the amount of U(IV) present, the reduction of the U(VI) to U(IV) is prevented by preparing all of the reagents in a separate beaker and then adding these reagents to the uranium sample (which has been dissolved in phosphoric acid). This method fixes the U(VI) at its oxidation state; hence, only the U(IV) that was initially present in the sample is titrated. After its titration with potassium dichromate, the amount of U(IV) is calculated based on the amount and concentration of potassium dichromate used.

4. RESULTS

Irradiation experiments were conducted for a number of uranyl fluoride and uranium oxide samples using either the ORNL ^{60}Co source or HFIR SNF elements. Table 4.1 provides a summary of the irradiation experiments performed.

Table 4.1. Summary of irradiation experiments performed

Container	Material	Mass (g)	Atmosphere	Irradiation source	Total dose (rad)[a]
S-1	$UO_2F_2 \bullet 1.7H_2O$	29.8	Air	^{60}Co	1.7×10^8
S-2[b]	$UO_2F_2 \bullet 0.4H_2O$	20.0	Helium[b]	^{60}Co	1.7×10^8
S-3	$UO_2F_2 \bullet 1.7H_2O$	10.8	Air	^{60}Co	1.7×10^8
S-4	$UO_2F_2 \bullet 0.4H_2O$	14.8	Helium	^{60}Co	1.7×10^8
S-12	$UO_2F_2 \bullet 1.4H_2O$	10.3	Helium	^{60}Co	2.4×10^8
S-13	$UO_2F_2 \bullet 0.4H_2O$	7.5	Helium	^{60}Co	2.4×10^8
S-16	O_2-burned UO_2F_2	9.85	Helium	^{60}Co	2.1×10^8
S-17	Converted U_3O_8[c]	8.0	Helium	^{60}Co	2.2×10^8
HFIR-1	$UO_2F_2 \bullet 0.4H_2O$	29.56	Helium	HFIR SNF	6.1×10^{10}[d]
HFIR-2	Converted U_3O_8[c]	29.96	Helium	HFIR SNF	3.0×10^{10}[d]
S-21	Air	*e*	Air	^{60}Co	1.5×10^8

[a] W-h/g = 3.6×10^8 rad.
[b] Container leaked during experiment.
[c] Contained 1.4 wt % fluorine.
[d] Dose based on 0.93-MeV average gamma energy.
[e] Air loaded at atmospheric pressure.

Several blanks were also run for comparison with the irradiation experiments. One of the blanks, S-21, was simply loaded with room air and irradiated. Information regarding S-21 is given in Table 4.1. The other blanks consisted of loading $UO_2F_2 \bullet xH_2O$, in either air or helium, and then withdrawing gas samples after a period of time (typically ~60–70 d). These blanks were not irradiated, but were maintained in the sample containers for the same period of time as were those for the irradiation experiments. The blank experiments for $UO_2F_2 \bullet xH_2O$ are summarized in Table 4.2.

The results obtained from the experiments are presented in Sects. 4.1 through 4.3; these results include pressure measurements and estimates of radiolytic yields (i.e., G-values), analyses of gases, and analyses of solid samples. In Sect. 4.4, results are described from an experiment in which a uranyl fluoride sample was burned in O_2 to remove carbon.

Table 4.2. Summary of blank (nonirradiation) experiments conducted for $UO_2F_2 \bullet xH_2O$

Container	Material	Mass (g)	Atmosphere	Time material in container (d)
S-8	$UO_2F_2 \bullet 1.7H_2O$	9.8	Air	60
S-20	$UO_2F_2 \bullet 1.4H_2O$	10.0	Helium	65
S-22	$UO_2F_2 \bullet 2.3H_2O$	11.95	Air	72

4.1 PRESSURE MEASUREMENTS

Pressure within the sample containers was monitored throughout the irradiations, and the pressure data from the ^{60}Co and HFIR SNF irradiations are shown in Figs. 4.1–4.9. Note that the units of pressure are Torr for the ^{60}Co irradiations, while the units are pounds per square inch gage (psig) for HFIR SNF irradiations. The pressure data for container S-2 are not shown because this container leaked to the atmosphere during the experiment. The pressure and gas yield (mmol gas/g sample) are plotted as a function of dose in the figures. The gas yield is calculated by applying the ideal gas law, namely:

$$\Delta n = \frac{1.32 \ \Delta P \, V_{void}}{R \, T_c \, m} \ , \tag{4.1}$$

where

Δn = gas yield (mmoles gas/g sample),

ΔP = change in pressure from initial value (Torr),

V_{void} = void volume of sample container (L),

R = 0.08205 atm-L/mol-K,

T_c = temperature in container (K), and

m = mass of sample (g).

The value 1.32 is a unit conversion factor.

Container temperatures in the ^{60}Co irradiator were measured to be 27–28°C. The temperature for the HFIR irradiation was taken to be 40°C—the SNF pool-water temperature.

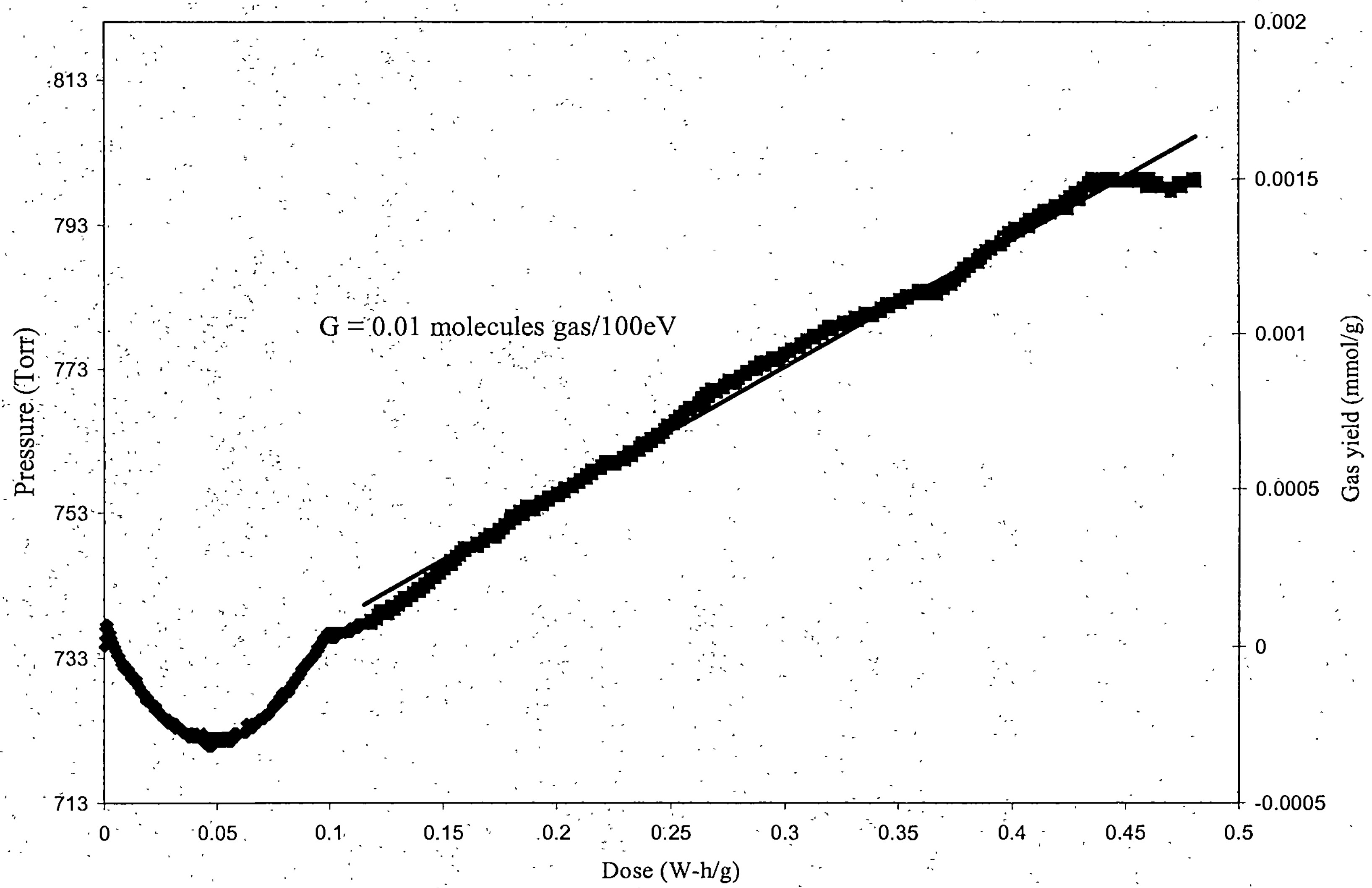

Fig. 4.1. Pressure and gas yield as a function of dose for sample S-1 (^{60}Co-irradiated $UO_2F_2 \cdot 1.7H_2O$ loaded in air).

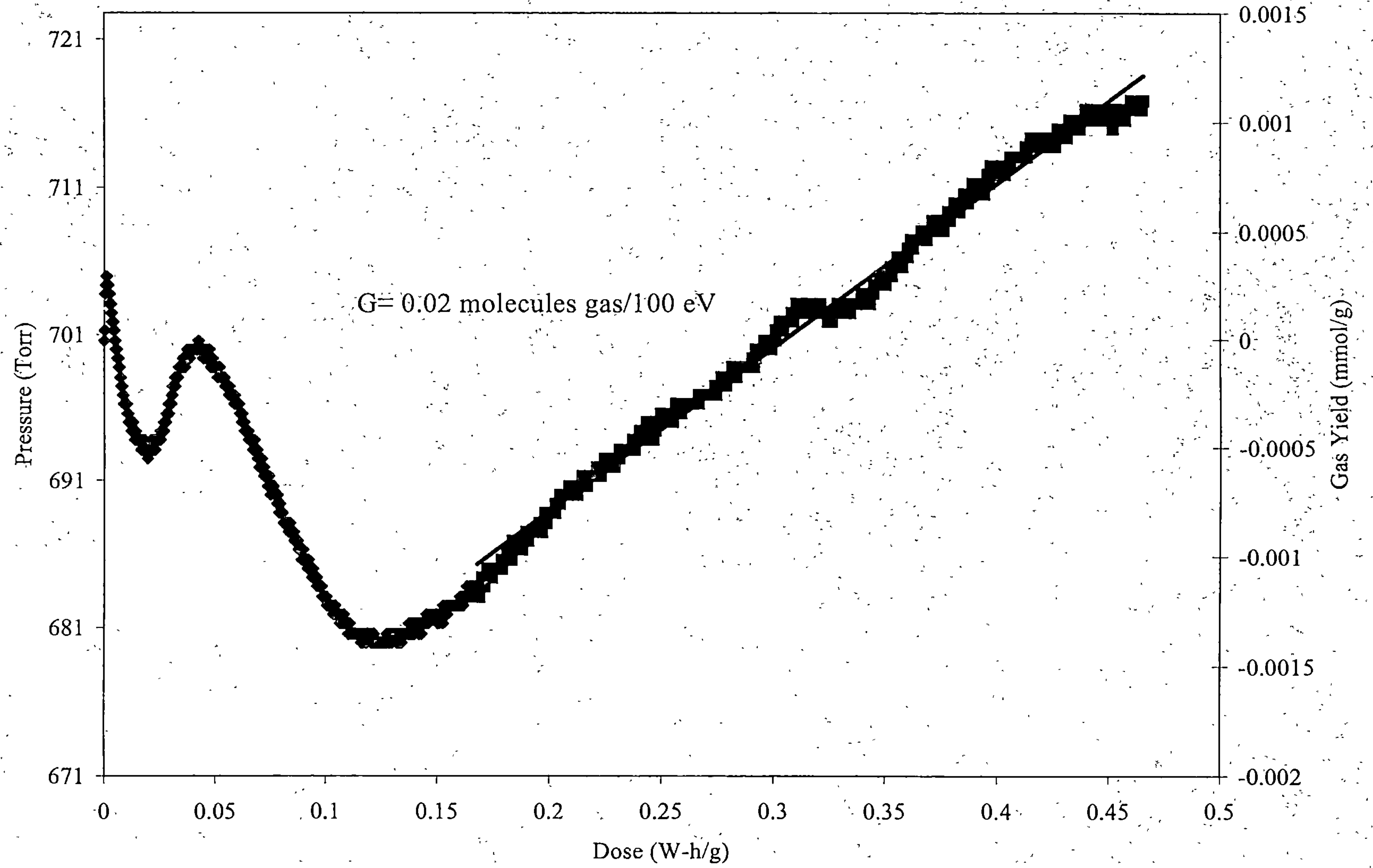

Fig. 4.2. Pressure and gas yield as a function of dose for sample S-3 (^{60}Co-irradiated $UO_2F_2 \cdot 1.7H_2O$ loaded in air).

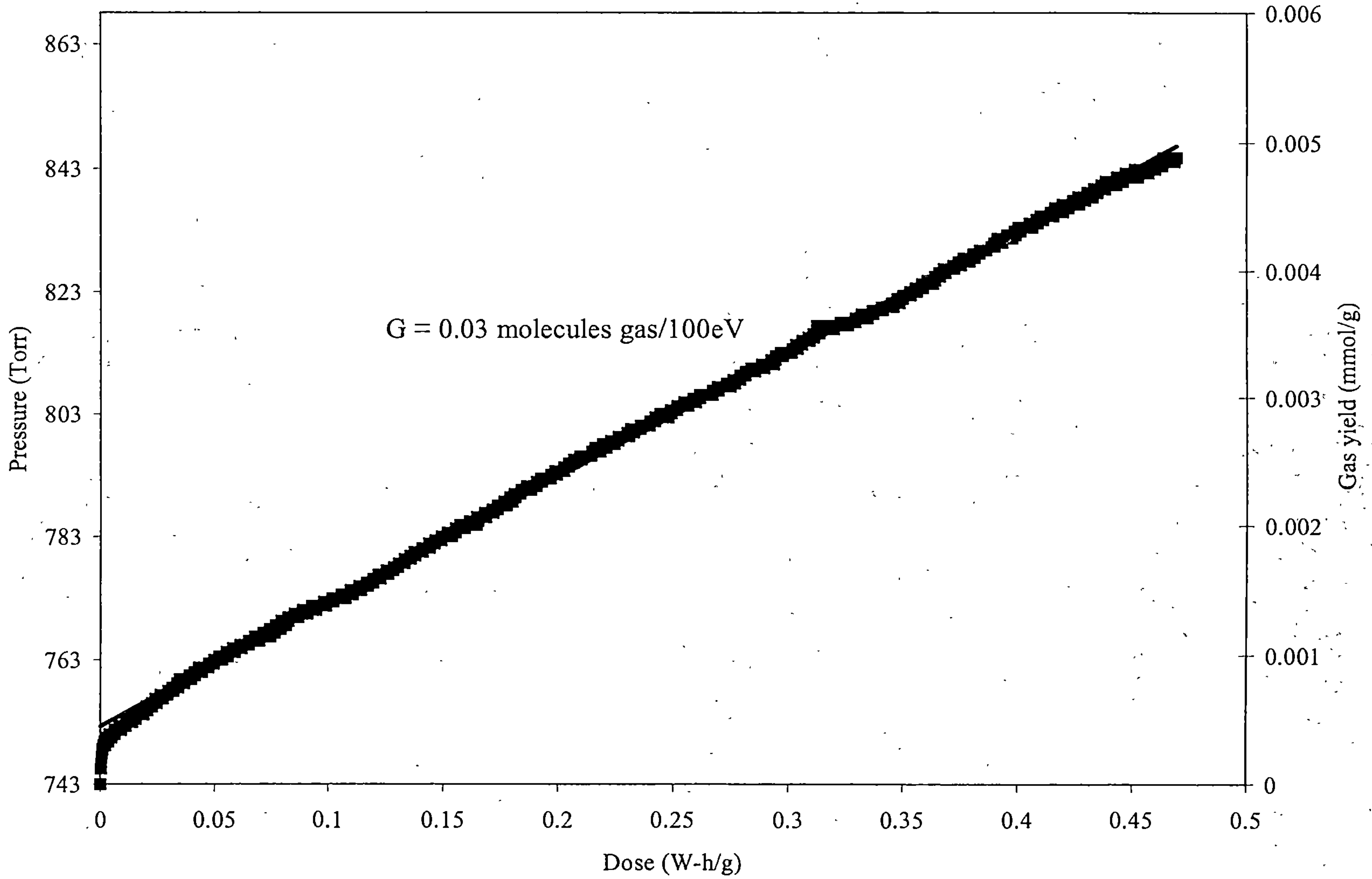

Fig. 4.3. Pressure and gas yield as a function of dose for sample S-4 (^{60}Co-irradiated $UO_2F_2{\bullet}0.4H_2O$ loaded in helium).

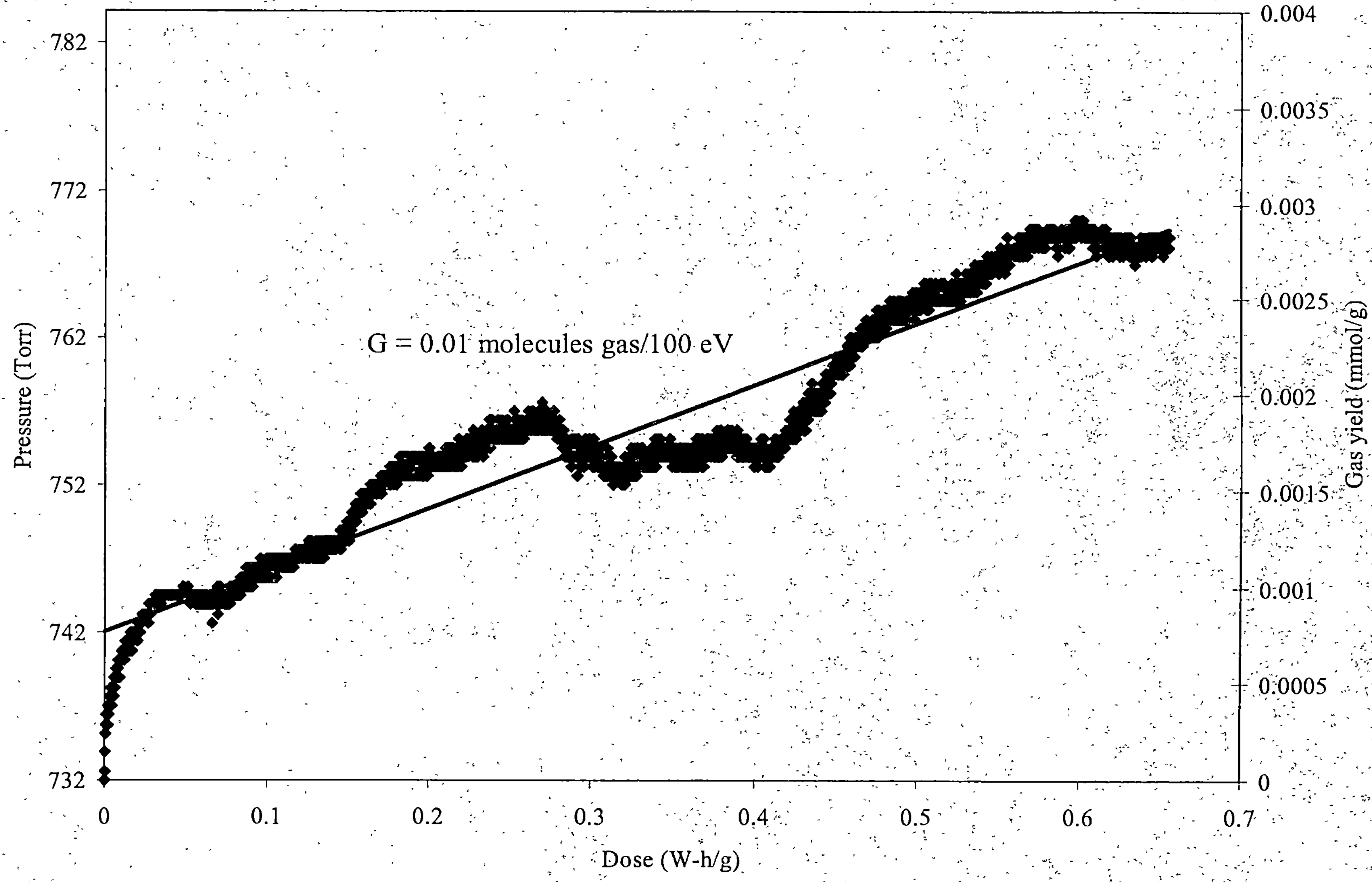

Fig. 4.4. Pressure and gas yield as a function of dose for sample S-12 (^{60}Co-irradiated UO_2F_2•$1.4H_2O$ loaded in helium).

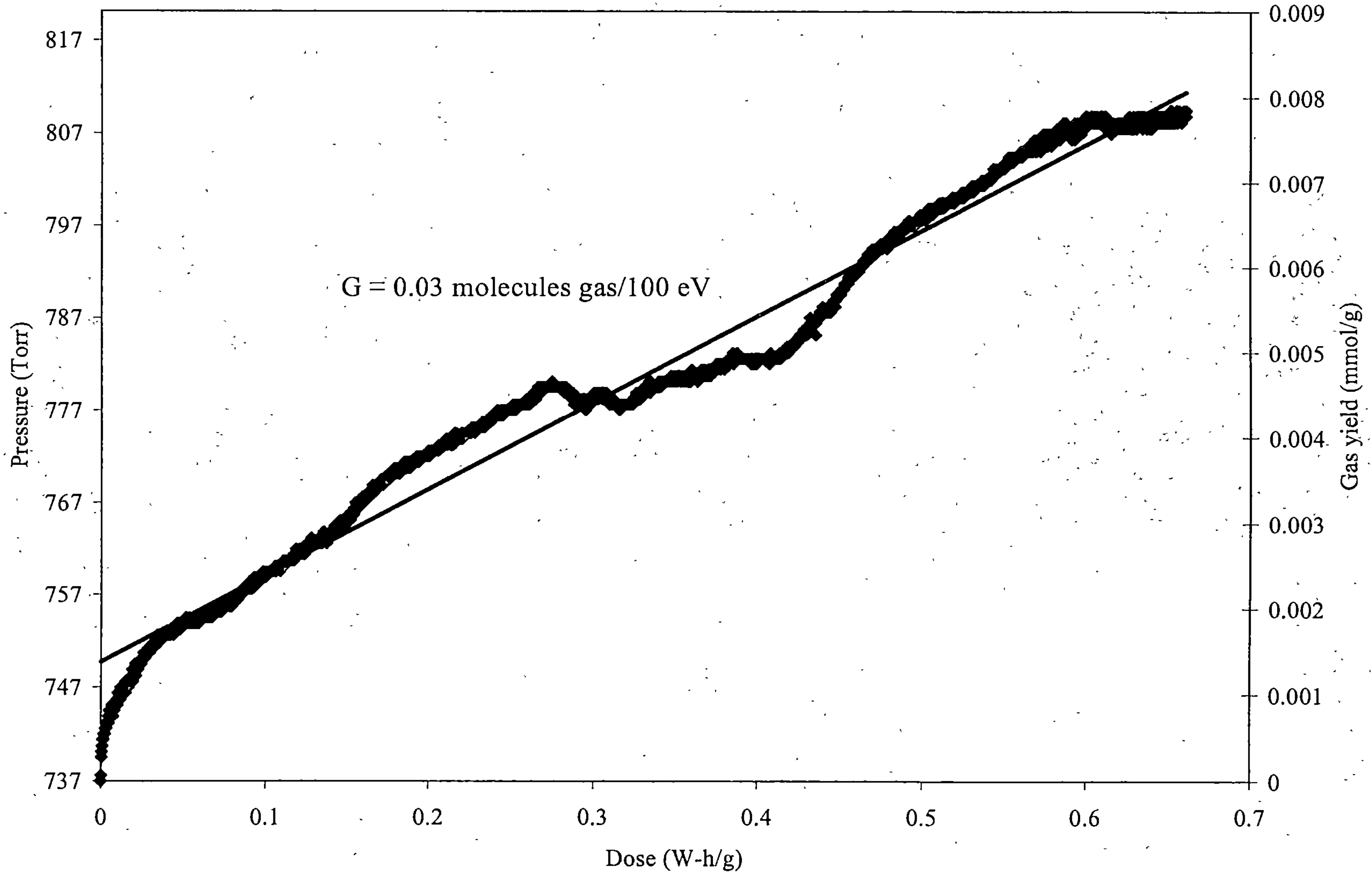

Fig. 4.5. Pressure and gas yield as a function of dose for sample S-13 (^{60}Co-irradiated $UO_2F_2 \cdot 0.4H_2O$ loaded in helium).

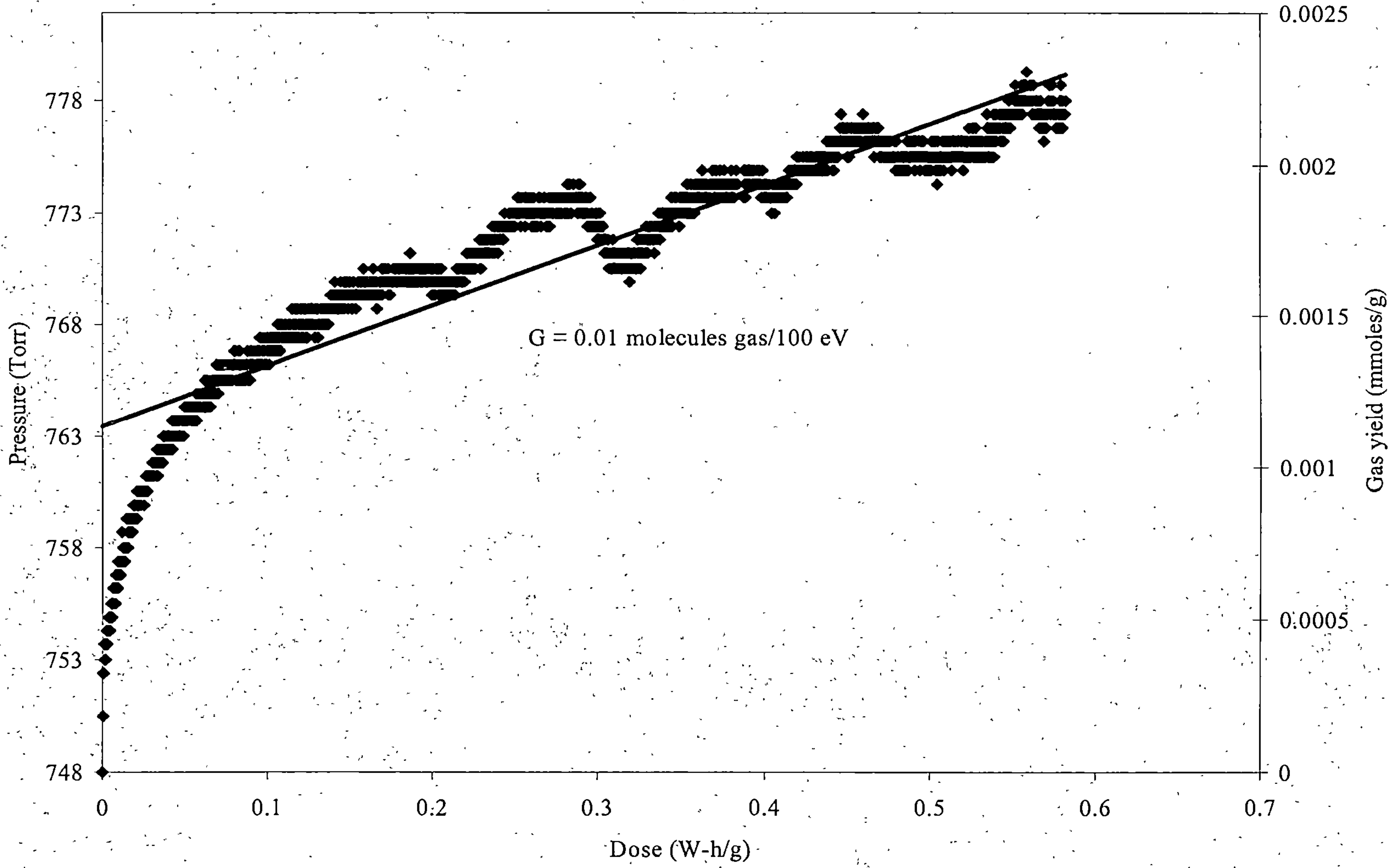

Fig. 4.6. Pressure and gas yield as a function of dose for sample S-16 (^{60}Co-irradiated, O_2-burned UO_2F_2 loaded in helium).

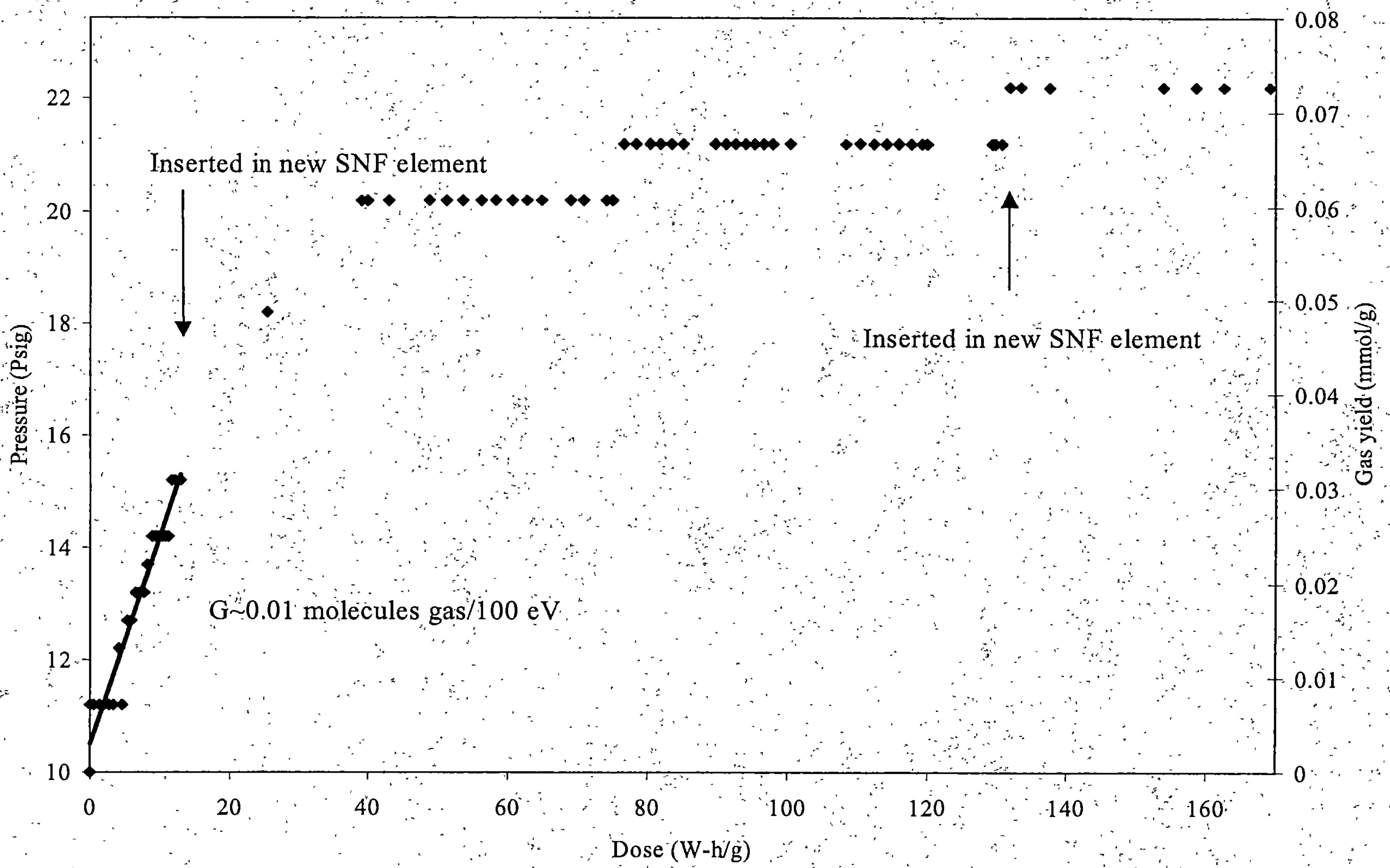

Fig. 4.7. Pressure and gas yield as a function of dose for sample HFIR-1 (HFIR SNF-irradiated UO_2F_2•$0.4H_2O$ loaded in helium).

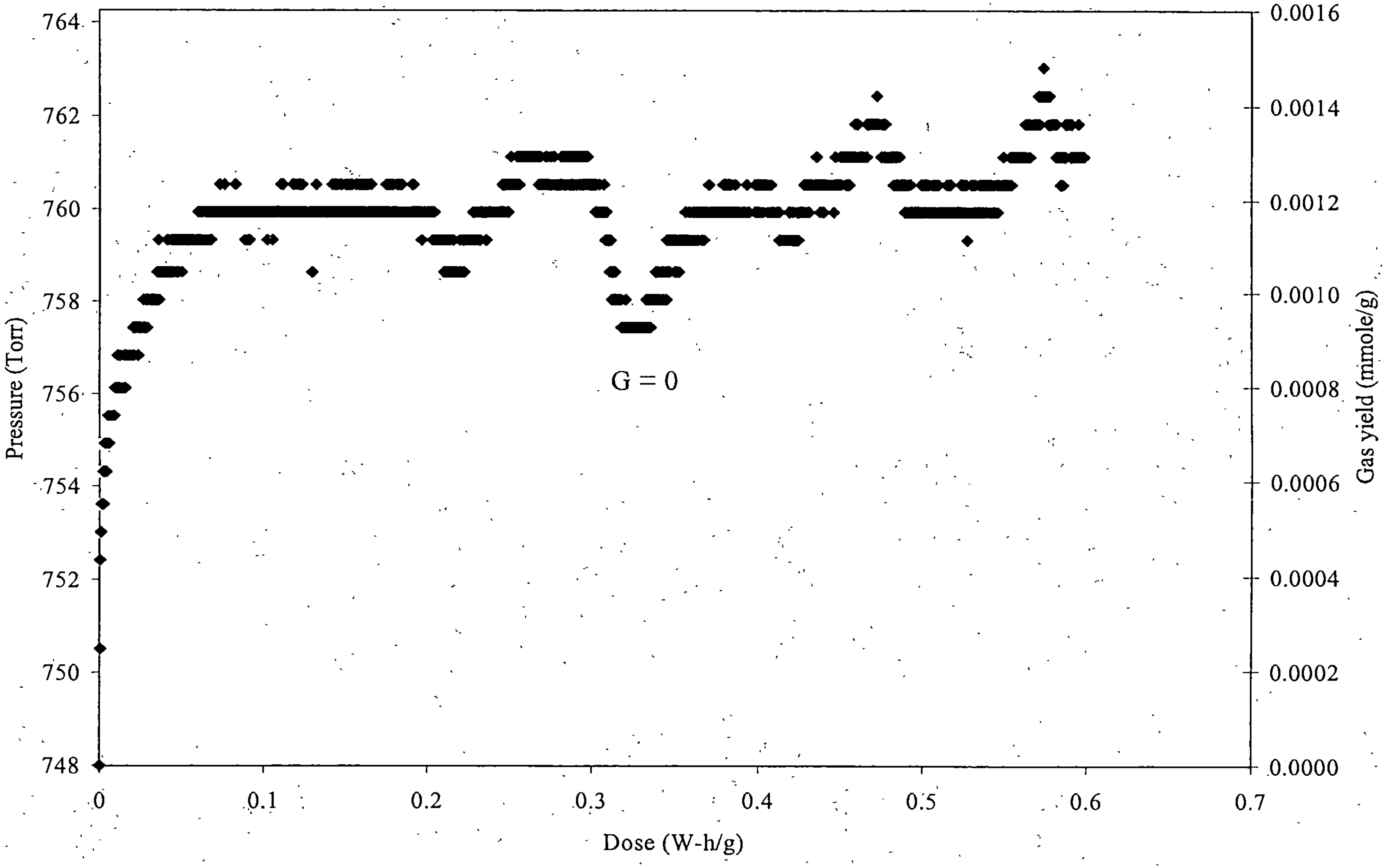

Fig. 4.8. Pressure and gas yield as a function of dose for sample S-17 [^{60}Co-irradiated converted U_3O_8 (with 1.4 wt % fluorine) loaded in helium].

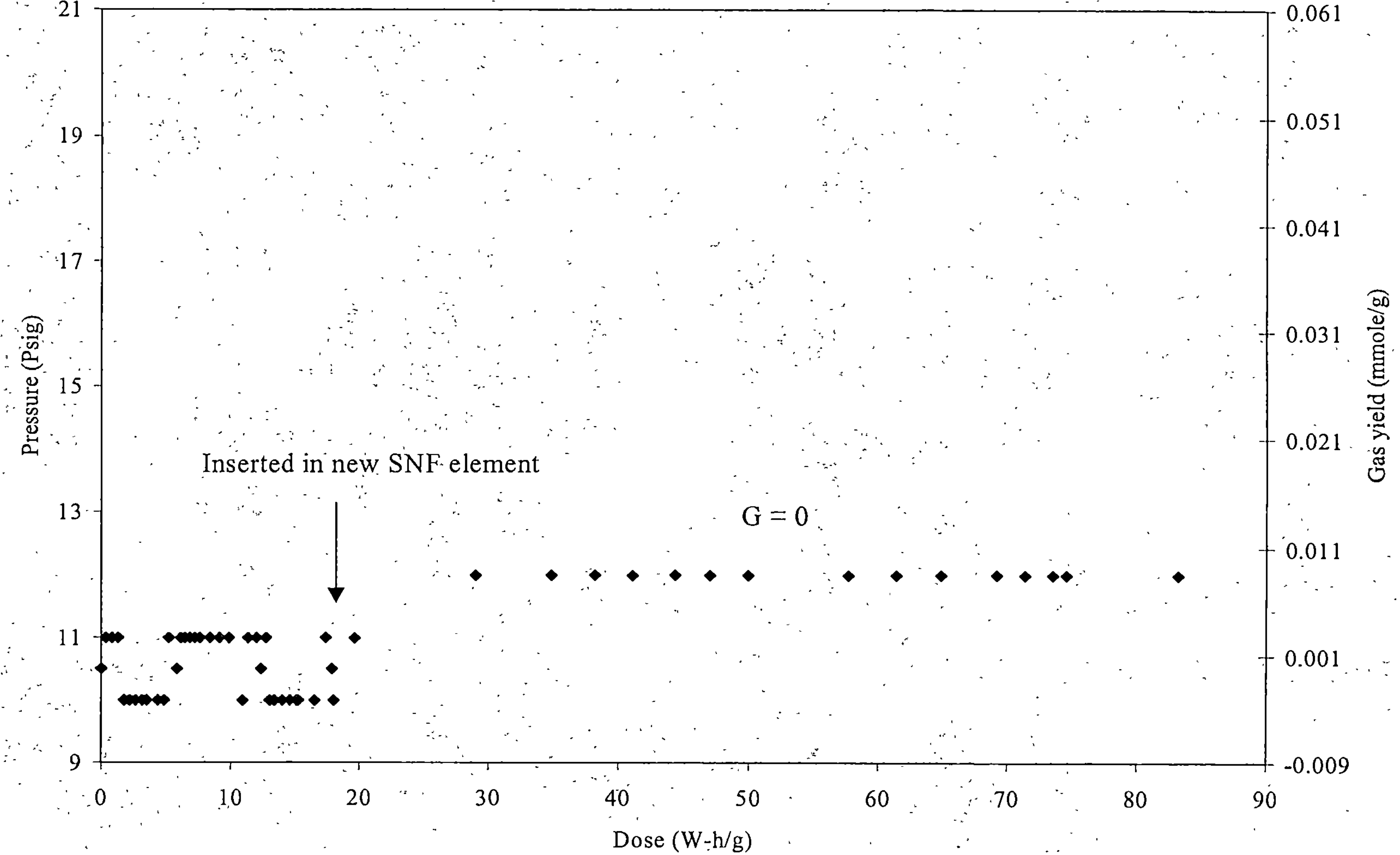

Fig. 4.9. Pressure and gas yield as a function of dose for sample HFIR-2 [HFIR SNF-irradiated, converted U_3O_8 (with 1.4 wt % fluorine) loaded in helium].

The dose (1 W-h/g = 3.6 × 10^8 rad) was computed from (a) the exposure rate for the position of the sample in the source and (b) the characteristics of the irradiated material, as described in Sects. 3.1.1 and 3.2.1, and in Appendix C.

The radiolytic yield of a species can be expressed by a *G-value*, which is defined as the number of molecules of a species produced (or destroyed) per 100 eV of energy deposited. The G-value for the gas produced, regardless of its composition, can be estimated from the slope of a line that is fit through the data presented in Figs. 4.1–4.9 (i.e., G(gas) = 2.68 × slope). For the HFIR SNF-irradiated sample, the G-value is estimated based on the linear region of the data, as shown in Fig. 4.7. G-values calculated from the irradiation experiments are shown in Table 4.3. Note that because the G-value is based on the pressure change in the container, both chemical and radiolytic reactions that contribute to the pressure change may be accounted for in the calculated G-value.

Figures 4.1 and 4.2 are for experiments S-1 and S-3, respectively. Both of these samples were $UO_2F_2 \bullet 1.7H_2O$, and both were loaded in air. These samples exhibited a pressure decrease at the beginning of the irradiation, followed by a steady (but small) pressure increase.

Figures 4.3–4.6 are for samples S-4, S-12, S-13, and S-16, respectively. Each of these samples was loaded in a helium atmosphere and placed in the ^{60}Co irradiator. None of these materials exhibited the initial pressure decrease observed for the air-loaded samples. Similarly, sample HFIR-1, which was loaded in helium and irradiated in HFIR SNF elements, also did not exhibit a pressure decrease (Fig. 4.7).

Table 4.3. **Estimated G(gas)-values for the irradiated samples**

Container	Material	Material source	Atmosphere	G(gas) (molecules gas/100 eV)
S-1	$UO_2F_2 \bullet 1.7H_2O$	ORNL	Air	0.01
S-3	$UO_2F_2 \bullet 1.7H_2O$	ORNL	Air	0.02
S-4	$UO_2F_2 \bullet 0.4H_2O$	ORNL	Helium	0.03
S-12	$UO_2F_2 \bullet 1.4H_2O$	ETTP	Helium	0.01
S-13	$UO_2F_2 \bullet 0.4H_2O$	ETTP	Helium	0.03
S-16	O_2-burned UO_2F_2	ORNL	Helium	0.01
S-17	Converted U_3O_8	ORNL	Helium	0
HFIR-1	$UO_2F_2 \bullet 0.4H_2O$	ORNL	Helium	0.01
HFIR-2	Converted U_3O_8	ORNL	Helium	0

The $UO_2F_2 \bullet xH_2O$ samples that were irradiated in the ^{60}Co source showed a slow, but steady, pressure increase. However, these samples did not reach a limiting value or pressure plateau. On the other hand, the $UO_2F_2 \bullet 0.4H_2O$ sample irradiated by HFIR SNF elements (Fig. 4.7) exhibited the classic results for radiolysis experiments (i.e., an initial linear increase in pressure followed by a plateau). However, there was no induction period (see Fig. 2.5).

The total dose to sample HFIR-1 was about 360 times the dose reached in the ^{60}Co source. Sample HFIR-1 was irradiated in three different SNF elements. The insertion of the experimental container into the second and third fuel elements is annotated on Fig. 4.7. After the sample was inserted into the second element, the gas yield began to approach a plateau. Upon insertion of the sample into the third element, the yield rose slightly to a new plateau.

Pressure data for sample S-17 are shown in Fig. 4.8. This experiment consisted of the ^{60}Co irradiation of converted U_3O_8 from the operation of the conversion prototype at ORNL. The sample was reported to contain about 1.4 wt % fluorine (Wilson 1997). The small pressure rise, as shown in Fig. 4.8, can be attributed entirely to the heating of the sample upon insertion into the irradiator. The pressure fluctuations, as shown on the relatively small scale of the graph, are the result of slight temperature variations. For this experiment, because no pressure increase resulting from radiolysis was observed, this material was assigned a G-value of zero.

Converted U_3O_8 (from the same stock as that used in S-17) was irradiated also in HFIR SNF elements (HFIR-2), and the results of pressure monitoring are shown in Fig. 4.9. The slight pressure rise seen in the data is attributed to the sample temperature increase and the resolution in the gage readings (i.e., operators read the gage to the nearest 0.5 psi). Overall, the pressure in this sample container was essentially unchanged, and a G-value of zero was again assigned to this material.

4.2 GAS ANALYSES

After each irradiation, gas samples were withdrawn from the containers, and the samples were analyzed by FTIR spectroscopy and MS. The FTIR provided an immediate identification of some of the gas constituents, but it could not be used to observe homonuclear diatomic molecules, such as H_2, F_2, and O_2. For the $UO_2F_2 \cdot xH_2O$ samples, the FTIR analysis showed the presence of CO_2 in the gas. A trace of HF was observed in some of the FTIR scans for samples loaded in air. However, it was later discovered that the fluorination of the FTIR gas cell (to passivate the cell before gas sampling) resulted in the production of the trace HF when the interior of the cell came into contact with moist air. No HF was seen for samples loaded in helium. Typical FTIR spectra for the gas samples are given in Appendix D.

Results of the MS analysis of the gas samples are presented in Tables 4.4–4.9. Table 4.4 gives the gas composition produced by radiolysis of samples loaded in air and irradiated with the ^{60}Co source (Marshall 1998a and 1998b); Table 4.5 gives the gas composition produced from samples loaded in helium and placed in the ^{60}Co irradiator (Marshall 1998b, 1999a, and 1999b); Table 4.6 gives the gas composition produced from a sample loaded in helium and placed in HFIR SNF elements (Marshall 1999c); and Table 4.7 gives the gas composition produced from converted U_3O_8 samples loaded in helium and placed in either the ^{60}Co source or HFIR SNF elements (Marshall 1999b and 1999d).

The results of the MS analysis for the blanks are shown in Tables 4.8 and 4.9. Table 4.8 is for the gas composition produced from the ^{60}Co irradiation of air (Marshall 1999e), while Table 4.9 gives the gas composition for samples loaded in either helium or air, and that were not irradiated (Marshall 1998b and 1999e).

Note that in each of the air-loaded samples, the MS analysis indicates the presence of some helium. After leak testing and volume measurement of a container, the container was backfilled with helium. When samples were loaded into these containers in air, not all of the helium was removed. Hence, helium appears in the gas analysis in these samples.

Table 4.4. Results of mass spectrometric analysis (vol %) of gas samples from materials loaded in air and irradiated in the ^{60}Co source

Component	S-1[a] ($UO_2F_2 \bullet 1.7H_2O$)	S-3[b] ($UO_2F_2 \bullet 1.7H_20$)
Initial atmosphere	Air	Air
N_2	57.18	66.3
He	20.99	20.7
H_2	5.76	5.07
CO_2	11.32	6.43
Ar	0.7	0.76
O_2	2.83	0.02
HF/Ar^{++}	<0.01	≤0.01
F_2	<0.01	<0.01
CH_4	<0.01	<0.01
CF_4		<0.01
CO		<0.01
NO		
H_2O	1.22	0.71

[a] Marshall 1998a.
[b] Marshall 1998b.

Table 4.5. Results of mass spectrometric analysis (vol %) of gas samples from materials loaded in helium and irradiated in the ^{60}Co source

Component	S-4[a] ($UO_2F_2 \bullet 0.4H_2O$)	S-12[b] ($UO_2F_2 \bullet 1.4H_2O$)	S-13[b] ($UO_2F_2 \bullet 0.4H_2O$)	S-16[c] (O_2-burned UO_2F_2)
Initial atmosphere	Helium	Helium	Helium	Helium
N_2	2.39	2.93	2.6	2.87
He	87.89	89.34	83.62	90.14
H_2	0.11	0.21	0.02	0.03
CO_2	9.31	2.45	3.36	2.17
Ar	0.02	0.27	0.25	0.36
O_2	0.09	4.73	10.11	4.25
HF/Ar^{++}	<0.01	0.03	0.03	0.07
F_2	<0.01	0.001	<0.001	0.0006
CH_4	0.13			0.01
CF_4	<0.01	0.002	<0.001	
CO	<0.01	<0.01	<0.01	<0.01
NO		0.002	0.002	0.001
H_2O	0.05	0.007	0.01	0.06

[a] Marshall 1998b.
[b] Marshall 1999a.
[c] Marshall 1999b.

Table 4.6. Results of mass spectrometric analysis (vol %) of gas samples from material loaded in helium and irradiated in HFIR SNF elements

Component	HFIR-1[a] ($UO_2F_2 \bullet 0.4H_2O$)	HFIR-1-Duplicate gas analysis[a] ($UO_2F_2 \bullet 0.4H_2O$)
Initial atmosphere	Helium	Helium
N_2	0.01	0.01
He	69.42	70.76
H_2	0.03	0.03
CO_2	29.86	28.54
Ar	0.57	0.55
O_2	<0.01	<0.01
HF/Ar^{++}	<0.01	<0.01
F_2	<0.01	<0.01
CH_4	<0.001	0.001
CF_4	<0.01	<0.01
CO	0.1	0.106
NO	<0.01	<0.01
H_2O	<0.01	0.01

[a] Marshall 1999c.

Table 4.7. Results of mass spectrometric analysis (vol %) of gas samples from materials loaded in helium and irradiated in either the ^{60}Co source (S-17) or HFIR SNF elements (HFIR-2)

Component	S-17[a] (Converted U_3O_8)	HFIR-2[b] (Converted U_3O_8)	HFIR-2-duplicate gas analysis[b] (Converted U_3O_8)
Initial atmosphere	Helium	Helium	Helium
N_2	2.18	2.03	2.05
He	96.21	96.11	96.09
H_2	0.02	0.004	0.004
CO_2	0.41	1.73	1.74
Ar	0.31	0.03	0.03
O_2	0.78	0.04	0.04
HF/Ar^{++}	0.06	0.005	0.005
F_2	<0.001	0.003	0.003
CH_4	0.0003	<0.001	<0.001
CF_4		<0.001	<0.001
CO	<0.01		
NO	<0.001		
H_2O	0.02	0.04	0.03

[a] Marshall 1999b.

[b] Marshall 1999d.

Table 4.8. Results of mass spectrometric analysis (vol %) of a gas sample from air irradiated in the ^{60}Co source[a]

Component	S-21 (air)
Initial atmosphere	Air
N_2	73.36
He	7.44
H_2	0.03
CO_2	0.19
Ar	0.97
O_2	17.11
HF/Ar^{++}	<0.001
F_2	
CH_4	0.01
CF_4	0.008
CO	
NO	
H_2O	0.46

[a] Marshall 1999e.

Table 4.9. Results of mass spectrometric analysis (vol %) of gas samples that were taken from materials loaded in air or helium and that were not irradiated

Component	S-8[a] ($UO_2F_2 \cdot 1.7H_2O$)	S-22[b] ($UO_2F_2 \cdot 2.3H_2O$)	S-20[b] ($UO_2F_2 \cdot 1.4H_2O$)
Initial atmosphere	Air	Air	Helium
N_2	80.93	16.53	4.6
He	8.26	10.2	94.33
H_2	8.43	72.8	0.14
CO_2	0.51	0.04	0.02
Ar	1.0	0.2	0.41
O_2	0.32	0.001	0.36
HF/Ar^{++}	<0.01	<0.001	<0.001
F_2	<0.01		
CH_4	0.03	0.002	0.005
CF_4	0.02	<0.01	
CO	<0.01		
NO			
H_2O	0.5	0.09	0.05

[a] Marshall 1998b.
[b] Marshall 1999e.

To evaluate the change in the atmosphere of the air-loaded samples, the standard composition (i.e., the U.S. standard atmosphere) for air is given in Table 4.10 for comparison (CRC 1992).

The gas analysis results for samples S-1 and S-3, both of which were $UO_2F_2 \bullet 1.7H_2O$ loaded in air and irradiated in the ^{60}Co source, are shown in Table 4.4. These two samples primarily showed the production of a small amount of H_2 and, surprisingly, CO_2. The amount of O_2 was depleted as compared to that which would be expected in the air-loaded samples (in spite of the presence of helium). No HF or F_2 was seen for either sample. The blank experiments, described later in this subsection, were

Table 4.10. U.S. standard atmosphere[a]

Component	Vol %
N_2	78.1
He	0.00052
H_2	0.00005
CO_2	0.031
Ar	0.93
O_2	20.9
CH_4	0.0002
Ne	0.0018
Kr	0.00011
Xe	0.000009

[a] CRC 1992.

performed to provide more insight into (a) the source of the H_2 and CO_2 and (b) into the depletion of the O_2.

To eliminate the complicating effects introduced by an air atmosphere, experiments were carried out on samples loaded in a helium atmosphere. Several different $UO_2F_2 \bullet xH_2O$ samples were irradiated with the ^{60}Co source, and gas analysis results for S-4, S-12, and S-13 are given in Table 4.5. Sample S-2 was also loaded in helium; however, because the sample container was found to be leaking during the experiment, the gas analysis results for S-2 were not meaningful. In samples S-4, S-12, and S-13, the majority of gas produced was either CO_2 or O_2. For sample S-4, the gas was primarily CO_2, and a trace amount of O_2. Samples S-12 and S-13 were from a different source of uranyl fluoride (from ETTP) than was S-4 (from ORNL). In the case of S-12 and S-13, most of the gas produced was O_2, along with a lesser amount of CO_2. Because only a very small amount of H_2 was found in the gas analysis for the three samples, radiolysis of the material does not appear to be a major source of H_2. A trace of F_2 was reported for one sample (S-12), but the amount reported was at the limit of detection for the mass spectrometer. Trace HF/Ar^{++} was reported for S-12 and S-13. However, in a mass spectrometer, argon produces an interference with HF because of Ar^{++}. The ratio of Ar^{++} to Ar is typically about 0.13, but this ratio is instrument-dependent. For samples S-12 and S-13, because of the ratio of the measured HF/Ar^{++} to the measured Ar, it is likely that the reported result is for Ar^{++} and not for HF. Furthermore, HF was not observed in the FTIR analysis of these gas samples.

Also given in Table 4.5 are the results of the gas analysis for sample S-16, which was irradiated in the ^{60}Co source. This sample contained UO_2F_2, which had been burned in O_2, removing some of the carbon from the sample and resulting in anhydrous UO_2F_2 (see Sect. 4.4). The uranyl fluoride used in this experiment was from the same stock used in S-4, so a comparison between S-4 and S-16 is warranted. Recall that for S-4 the majority of the gas produced was CO_2, with a lesser amount of O_2. Analysis of gas from sample S-16 showed that the majority of the gas produced was O_2, with a lesser amount of CO_2. Thus, it appears that the burning of the $UO_2F_2 \bullet 0.4H_2O$ in O_2 made less carbon (which is present as an impurity in the sample) available for interaction with either O_2 or oxygen radicals released from the UO_2F_2 sample. Trace F_2, again at the limit of detection, was reported for S-16. Trace HF/Ar^{++} was also reported for S-16, which again is attributed to Ar^{++} because (a) the ratio of the measured HF/Ar^{++} to the measured Ar is consistent with the calibrated Ar^{++} to Ar ratio for the instrument and (b) HF was not observed in the FTIR analysis of the gas sample.

Gas analysis results for HFIR-1, which was for $UO_2F_2 \bullet 0.4H_2O$ loaded in air and irradiated in HFIR SNF elements, are shown in Table 4.6. Two gas samples were taken and analyzed for HFIR-1. The material irradiated was from the same stock as that used in S-4 (Table 4.5). The analysis showed that the majority of gas produced was CO_2, with a trace of CO. No O_2 was reported. These results were consistent with those reported for S-4. Neither F_2 nor HF was reported for HFIR-1, which was irradiated until a plateau pressure was reached.

In Table 4.7, the gas analysis results for S-17 and HFIR-2 are shown. Each of these samples consisted of U_3O_8 from operation of the MSRE conversion prototype, and each were loaded in helium. The U_3O_8 contained 1.4 wt % fluorine. Sample S-17 was irradiated in the ^{60}Co source, while HFIR-2 was irradiated in HFIR SNF elements. Two gas samples were taken and analyzed for HFIR-2. No significant pressure rise was seen during either of these irradiations, and only a small amount of CO_2 or O_2 was found in each of the gas samples. A trace of F_2 was reported for HFIR-2. Trace HF was reported also for both S-17 and HFIR-2. However, HF was not observed in the FTIR spectra for these two samples, and the ratio of the HF/Ar^{++} value to the Ar value indicates that the measured result is actually Ar^{++} and not HF.

Table 4.8 gives the gas analysis results for a blank experiment (S-21), which consisted of ^{60}Co-irradiation of air. The composition is little changed from that expected for air. The amount of H_2 and CO_2 are somewhat higher than would be expected in air, but did not show the large increases seen in the irradiation experiments with $UO_2F_2 \bullet xH_2O$.

In Table 4.9, MS analysis results are given for several blanks of $UO_2F_2 \bullet xH_2O$ that were loaded in either air or in helium. These samples were not irradiated. Samples S-8 and S-22, which were both loaded in air, showed that H_2 was produced— a very large amount in the case of sample S-22. The O_2 is depleted, as compared to what would be expected in both samples. The amount of CO_2 is elevated, as compared to the expected value for air, but again this amount is small as compared to the amount measured in the irradiated UO_2F_2 samples. The H_2 production and O_2 depletion may have resulted from corrosion of the container. Sample S-20, which was loaded in helium, did not exhibit the large H_2 production seen for S-8 and S-22. A very small amount of O_2 and CO_2 was also reported for S-20.

4.3. SOLIDS ANALYSES

After irradiation, solid samples were taken from the irradiated materials. These samples were observed for physical changes, such as color change. Analyses were also performed on the samples including valence determination, XRD, and ATR. The sample containers were inspected for signs of corrosion. Metal sample coupons were also placed in the HFIR-2 container; these coupons were inspected after completion of the HFIR SNF irradiation. The results of these analyses and inspections are described in Sects. 4.3.1–4.3.5.

4.3.1 Sample Color

After irradiation, it was observed that the uranyl fluoride samples exhibited a color change from yellow to green. This change was most evident for the $UO_2F_2 \bullet 1.7H_2O$ samples, which were initially bright yellow—characteristic of hydrated uranyl fluoride. After irradiation, the samples were green. Because U(IV) fluoride is characteristically green, this color suggested a change in the uranium valence from VI to IV, which prompted further investigation of the uranium valence. Although not as strong, a change from yellow to green was observed also for the $UO_2F_2 \bullet 1.4H_2O$. Very subtle color changes were noticed in the drier uranyl fluoride samples (i.e., $UO_2F_2 \bullet 0.4H_2O$).

4.3.2 Uranium Valence

The color change observed in some of the uranyl fluoride samples after their irradiation suggested a possible change in the uranium valence from VI to IV. To explore this possibility, two methods were used to determine the uranium valence: Davies-Gray titration and XPS. The Davies-Gray titration provides a measure of the amount of U(IV) in the bulk sample, while XPS provides information on the valence state of the uranium at the surface of a sample.

4.3.2.1 Davies-Gray Titration

The amount of U(IV) in the uranyl fluoride samples was evaluated by Davies-Gray titration (Jarabek 1984), which was performed by the Materials Characterization Laboratory of Oak Ridge, Tennessee. The results of the titrations (Jarabek 1999a, 1999b, 1999c, 1999d, and 1999e) are summarized in Table 4.11, which shows the percentage of U(IV) before and after irradiation for several samples. Also shown is the ratio of the amount of U(IV) in the irradiated sample to that in the unirradiated sample. For each of the samples (except S-16), it is clear that the amount of U(IV) has increased after gamma irradiation—indicating a reduction of some of the uranium. An interesting trend evident in Table 4.11 is that the drier materials showed a larger increase in percentage of U(IV) than did the higher hydrates. The exception to this trend is the O_2-burned UO_2F_2 (S-16).

Table 4.11. Results of analysis of uranyl fluoride samples for U(IV)[a] before and after gamma irradiation

Experiment	Material	Dose (rad)	Percentage of U as U(IV)		Ratio of irradiated sample U(IV)% to unirradiated sample U(IV)%
			Before irradiation	After irradiation	
S-1	$UO_2F_2 \bullet 1.7H_2O$	1.7×10^8	0.204	0.474	2.32
S-3	$UO_2F_2 \bullet 1.7H_2O$	1.7×10^8	0.204	0.596	2.92
S-3[b]			0.204	0.339	1.66[b]
S-12	$UO_2F_2 \bullet 1.4H_2O$	2.4×10^8	0.388	1.270	3.27
S-2	$UO_2F_2 \bullet 0.4H_2O$	1.7×10^8	0.408	1.931	4.73
S-2[c]			0.408	1.654	4.05[c]
S-4	$UO_2F_2 \bullet 0.4H_2O$	1.7×10^8	0.408	1.964	4.81
S-13	$UO_2F_2 \bullet 0.4H_2O$	2.4×10^8	0.114	1.168	10.25
S-13[c]			0.114	1.064	9.33[c]
HFIR-1[d]	$UO_2F_2 \bullet 0.4H_2O$	6.1×10^{10}[e]	0.408	9.131	22.38
HFIR-1[c,d]			0.408	7.595	18.62
S-16	O_2-burned UO_2F_2	2.1×10^8	1.834	1.454	0.79
S-16[c]			1.834	1.235	0.67

[a] Analyzed by Davies-Gray titration (Jarabek 1984).

[b] After irradiation, this sample was heated to 200°C, first under vacuum and then under an air atmosphere. The sample was then analyzed for U(IV) content.

[c] Duplicate U(IV) analysis performed.

[d] Sample reached steady-state pressure plateau, at which point the damage is independent of dose.

[e] Dose based on 0.93-MeV average gamma energy.

One of the irradiated samples, S-3, was heated to 200°C, first in a vacuum and then in air. Subsequent chemical analysis of this material revealed a decrease in the U(IV) content, suggesting a back reaction of the material with air.

A comparison of the estimated moles of U(IV) produced and the moles of oxygen produced is given in Table 4.12. The number of moles of U(IV) produced were estimated from the data provided by the Davies-Gray analyses. Additionally, for the samples loaded in helium, the number of moles of oxygen produced (i.e., moles O_2 and moles CO_2) were estimated from the gas analyses given in Tables 4.5 and 4.6. This estimation was not performed for the samples initially loaded in air, because of the presence of O_2 and CO_2 at the beginning of the irradiations.

Table 4.12. Comparison of moles of U(IV) and O_2/CO_2 produced by gamma irradiation of $UO_2F_2 \bullet xH_2O$ samples

Container	Material	Moles U(IV) produced	Moles $O_2 + CO_2$	Moles $O_2 + CO_2$ / moles U(IV)
S-4	$UO_2F_2 \bullet 0.4H_2O$	7.30×10^{-4}	5.62×10^{-5}	0.0769
S-12	$UO_2F_2 \bullet 1.4H_2O$	2.71×10^{-4}	4.36×10^{-5}	0.161
S-13	$UO_2F_2 \bullet 0.4H_2O$	2.49×10^{-4}	8.85×10^{-5}	0.356
S-13[a]		2.24×10^{-4}	8.85×10^{-5}	0.395
HFIR-1	$UO_2F_2 \bullet 0.4H_2O$	8.15×10^{-3}	1.93×10^{-3}	0.237
HFIR-1[a]		6.71×10^{-3}	1.93×10^{-3}	0.287
S-16	O_2-burned UO_2F_2	-1.21×10^{-4}	3.78×10^{-5}	-0.312
S-16[a]		-1.91×10^{-4}	3.78×10^{-5}	-0.198

[a] Duplicate Davies-Gray analysis performed.

Associated with the formation of U(IV) should be the release of oxygen (from the uranyl group), appearing as O_2 or CO_2. The ratio of moles $O_2 + CO_2$ to moles U(IV) should be 0.5. In all cases, the ratio is less than 0.5—varying from about 0.08 up to 0.4 (Table 4.12). The ratio shows that some of the oxygen produced may have been trapped inside the uranyl fluoride matrix or otherwise scavenged. Note, in the case of S-16, that the moles of U(IV) produced are negative, because this sample experienced a net oxidation.

4.3.2.2 XPS

XPS provides an analysis of the valence of the atoms at the surface of a material. This analysis was performed by the Analytical Services Organization of the Y-12 Plant in Oak Ridge, Tennessee (Thompson 1998a, 1998b, 1999).

XPS analyses were performed for samples S-1, 2, 3, 4, 12, and 13. Thibaut et al. (1982) reported valence-band peak positions for a number of uranium halides and uranium oxyhalides. For U(IV), U(V), and U(VI), many of the peak positions are very similar. The exception is the peak labeled "A" by Thibaut et al. (1982). In the case of UF_4 and UF_5, this peak occurs at 2.8 and 2.7 eV, respectively. By comparison, the "A" peak does not exist for UO_2F_2. A very weak "A" peak was observed for samples S-1, 2, 3, and 4, indicating the presence of U(IV) or U(V) on the surface of the samples. The XPS valence spectrum for sample S-1 is shown in Fig. 4.10. This spectrum is similar to those obtained for the other samples. The weakness of the peak did not allow for the determination of its exact position; therefore one could not differentiate between the

ORNL DWG 99C-6901

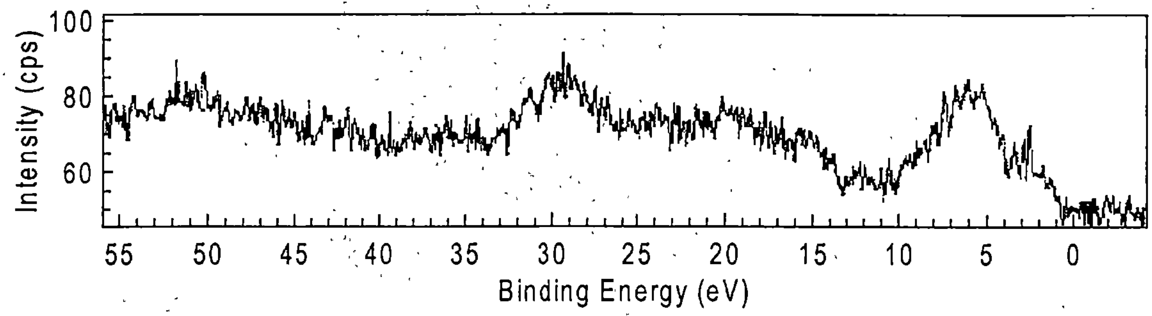

Fig. 4.10. XPS valence spectrum for sample S-1.

presence of U(IV) and U(V). The "A" peak was not observed for samples S-12 and 13.

Because of the weakness of the peaks that were obtained and the lack of quantitative results, XPS analyses were not performed for subsequent samples.

4.3.3 XRD

XRD analyses were performed on $UO_2F_2 \cdot xH_2O$ samples both before and after irradiations. After the irradiation, there was little, if any change in the XRD spectra. The irradiated material retained its crystalline structure. Additionally, any structural changes produced by the irradiation may have been so small that they were not evident in the XRD spectra.

4.3.4 ATR

ATR analyses were performed before and after irradiation of $UO_2F_2 \cdot xH_2O$ samples. The ATR spectra were found to be unchanged after irradiation.

4.3.5 Metallographic Examination

Sample HFIR-2 contained converted U_3O_8 and stainless steel metal coupons (types 304, 304L, 316, and 316L), which were examined after they were irradiated in HFIR SNF elements. The surfaces of these coupons were compared with those of unexposed blanks, and no differences were seen. Sample containers S-3 and S-8 were examined also, revealing no differences from the unexposed material. However, examination (at 500X magnification) of sample container S-22 did reveal corrosion on the surface, as shown in Fig. 4.11. For comparison, a photograph of an unexposed blank is shown in Fig. 4.12. The material for this blank was from the same stock as that used in the fabrication of S-22. The photograph for S-22 indicates that corrosion has occurred; this finding is consistent with the observation of H_2 production for this sample.

4.4 BURNING $UO_2F_2 \bullet xH_2O$ IN O_2

Because irradiation of $UO_2F_2 \bullet xH_2O$ was shown to produce both CO_2 and O_2, it was desirable to remove as much carbon from the UO_2F_2 as possible to evaluate if the carbon impurities played a role in the production of CO_2. A sample of $UO_2F_2 \bullet 0.4H_2O$ was burned in O_2 using an apparatus described in Sect. 3.1.4 and schematically depicted in Fig. 3.6. Uranyl fluoride decomposes to UF_6 and U_3O_8 at temperatures above 700°C (Ferris and Baird 1960), so the burning was conducted in the temperature range 500–550°C.

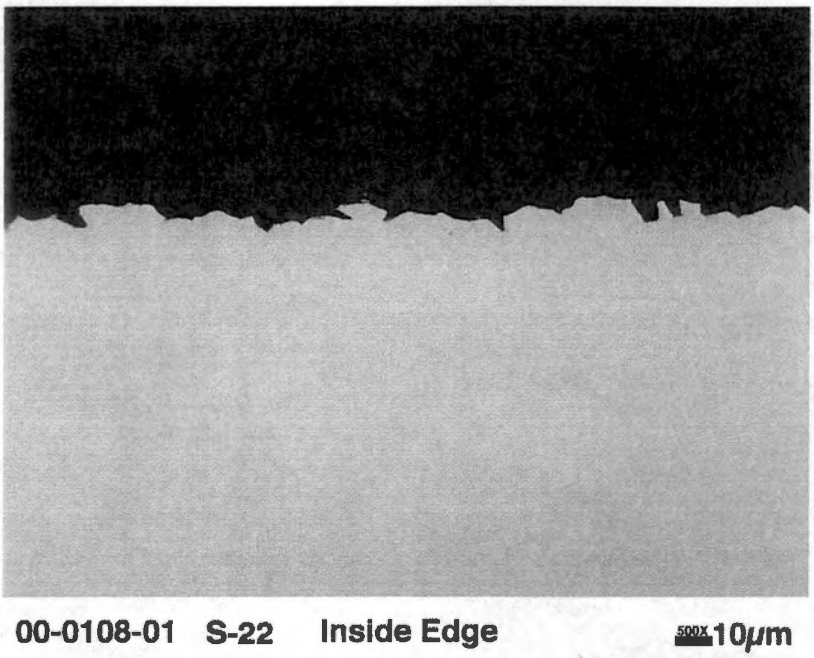

Fig. 4.11. Photograph from metallographic examination of the type 304L stainless steel container for sample S-22.

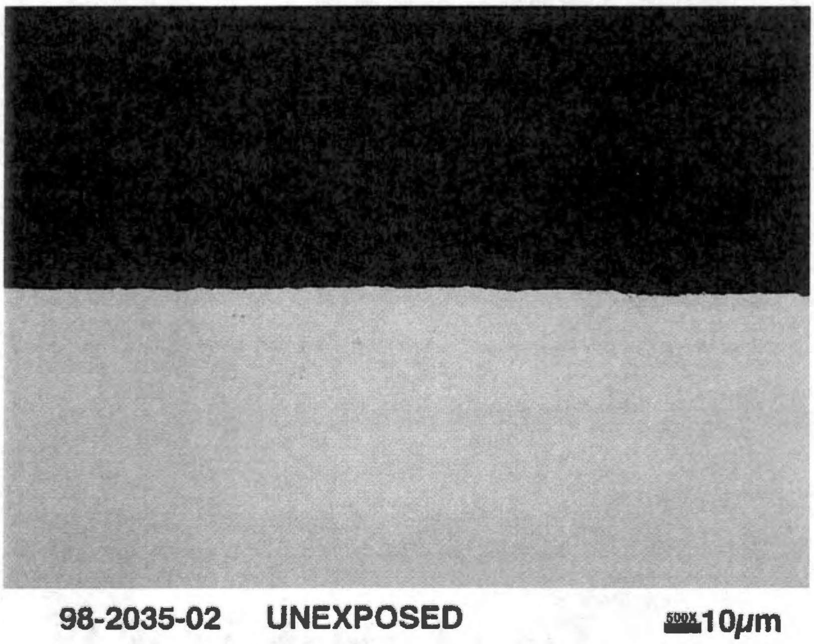

Fig. 4.12. Photograph from metallographic examination of unexposed type 304L stainless steel tubing.

A 10-g sample of UO_2F_2•$0.4H_2O$ was burned in O_2 at pressures from 450–650 Torr. The off-gas from the burning was periodically monitored with an FTIR, which showed that CO_2 was produced. Burning continued until no CO_2 was observed in the FTIR spectrum. After the sample cooled, it was removed from the silica tube in an inert-atmosphere glove box to maintain the material in a dry environment. An ATR analysis, performed on the O_2-burned UO_2F_2, indicated that the material was anhydrous UO_2F_2. A more detailed description of the ATR spectrum for this material is given in Appendix D.

Davies-Gray analysis of the sample following its burning indicated a small increase in the amount of U(IV) (Jarabek 1999d). This result was consistent with the observation of a very small amount of fine black powder specks on the alumina sample boat (and presumably in the sample itself) after completion of O_2 burning. These data indicate that even at the lower temperatures (500–550°C) a small amount of UO_2F_2 decomposed to U_3O_8. A second batch of O_2-burned UO_2F_2 was prepared by the same method, and Davies-Gray titration (Jarabek 1999e) confirmed the production of a small amount of U(IV).

5. DISCUSSION

Radiolysis experiments were performed to demonstrate the effects of large radiation doses on U_3O_8 and halide impurity components. In this section, the results of the experiments are summarized and interpreted with respect to the radiolysis of $UO_2F_2{\bullet}xH_2O$ and residual fluoride compounds in U_3O_8. $UO_2F_2{\bullet}\,xH_2O$ is an intermediate compound produced during the conversion of UF_6 to U_3O_8, and this compound represents the maximum fluoride content that could be present in the stored oxide. Irradiation of the U_3O_8 provided data on material similar to that which will be placed into storage.

First, the results for the gas yield, gas composition, and valence change are individually discussed. These discussions are then summarized to provide a clearer overall picture regarding the radiolysis of UO_2F_2 and residual fluoride compounds in U_3O_8.

5.1 GAS YIELD

For all of the $UO_2F_2{\bullet}xH_2O$ samples, pressure was seen to increase during gamma irradiation by either the ^{60}Co source or HFIR SNF elements. In all cases, the total pressure increase was small, with a maximum increase of less than 1 atm reached for the HFIR SNF element irradiation. G-values were calculated based on the gas yield (regardless of composition) and the dose. Note, however, that the G-value is calculated from the pressure change in the container and that both chemical and radiolytic reactions may contribute to the gas produced. This idea will be explored further in the discussion of the gas compositions (Sect. 5.2).

The calculated G-values were relatively consistent for different types and sources of samples, atmospheres, and radiation sources—ranging from 0.01 to 0.03 molecules of gas produced per 100 eV absorbed in the sample. Although not a conclusive trend, it was observed for the ^{60}Co irradiations that the lower hydrates (i.e., $UO_2F_2{\bullet}0.4H_2O$) have higher G-values than do the higher hydrates (i.e., $UO_2F_2{\bullet}1.4H_2O$ and $UO_2F_2{\bullet}1.7H_2O$). The radiolysis of the waters of hydration on the sample probably plays a role in suppressing the radiolytic gas yield from the higher hydrates. For example, the radiolytic products of water can react with the radiolytic products from the irradiation of $UO_2F_2{\bullet}xH_2O$, thereby lowering the overall gas production. The exception to this observation is for the ^{60}Co-irradiation of the O_2-burned UO_2F_2 samples. This sample, which was anhydrous UO_2F_2, exhibited a G-value of about 0.01 molecules of gas produced per 100 eV, similar to the yields for the higher hydrates.

In the case of the HFIR SNF irradiation of $UO_2F_2{\bullet}0.4H_2O$, the calculated G-value was 0.01 molecules of gas produced per 100 eV, again similar to the yields for the higher hydrates of $UO_2F_2{\bullet}xH_2O$ that were irradiated in the ^{60}Co source. The G-value for HFIR-1 was calculated from the linear region of the gas yield curve (Fig. 4.7) and was based on a dose of about 4.7×10^9 rad (13 W-h/g). By contrast, the G-values for the ^{60}Co irradiation of the same material were based on a total dose of about 1.7×10^8 rad (0.47 W-h/g). The slightly lower G-value for the HFIR irradiation may be the result of a decrease in the gas yield as the approach to a plateau (or saturation) begins. This type of effect was reported by Allen and Ghormley (1947) and Henning, Lees and Matheson (1953), as described in Sect. 2.3.3. Allen and Ghormley found that the production rate of NO_2^- from electron-irradiated $Ba(NO_3)_2$ crystals decreased with increasing dose. Similarly, Henning, Lees, and Matheson (1953) reported that the G-values for the production of O_2 from nuclear reactor irradiation of $NaNO_3$ decreased with higher total doses.

The ^{60}Co irradiations provide insight into the early, low integrated dose behavior of $UO_2F_2 \bullet xH_2O$ under gamma irradiation. The HFIR SNF irradiations, on the other hand, provide information on ultimate effects at high doses. For HFIR SNF irradiation, data of higher resolution (i.e., more frequently recorded data points at the earlier, lower doses) may reveal the initially higher gas yield. (Note that data for HFIR SNF irradiations were recorded about every 12 h and that, during a 12 h period, the dose to the sample by a HFIR SNF element would be greater than the dose achieved in a 40–50-d irradiation in the ORNL ^{60}Co source.)

The irradiation of $UO_2F_2 \bullet xH_2O$ samples with the ^{60}Co source showed a steady pressure increase and no sign of a plateau being approached. To evaluate if such a plateau could be reached, higher total doses were needed; hence, HFIR SNF elements were used. These elements produced dose rates up to 1,000 times those in the ^{60}Co source (depending on the time since discharge of the element from the reactor). The total dose in the HFIR SNF elements was about 360 times higher than that which was achieved in the ^{60}Co source. Indeed, by using the higher dose rate and higher total dose, a pressure (or, equivalently, a gas yield) plateau for a $UO_2F_2 \bullet 0.4H_2O$ sample was observed (Fig. 4.7). After the sample was inserted into the first fuel element, it was moved to a fresher element on two occasions. When the sample was inserted into the second element, the gas yield began to approach a plateau. After inserting the sample into the third element, the yield rose slightly to a new plateau. This rise is the result of the higher dose rate and hence, a higher radiolytic production rate. The pressure then rises as a new limiting value is reached.

After the plateau is reached, the system is at steady state for that dose rate. During irradiation, some of the radiolytic products recombine with the damaged sites in the sample. At steady state, the radiolytic production rate equals the recombination rate. Upon insertion of the sample into a higher dose rate field, the radiolytic production increases, with the net result being that more gas is released from the sample as a higher steady state is established.

The pressure plateau is a measure of the limiting matrix damage to the $UO_2F_2{\bullet}xH_2O$. This value is estimated to be about 7 to 9% based on the Davies-Gray titrations performed after the irradiation (Table 4.11). In contrast, the damage limit for the LiF-BeF_2 salt measured by Toth and Felker (1990) was about 2% at the same dose rate. The larger amount of damage, at saturation, in the $UO_2F_2{\bullet}xH_2O$ indicates that the covalently bonded uranyl group is more susceptible to radiation damage than is the ionically bonded fluorine.

Unlike the results reported for irradiated MSRE-type fuel salts (Sect. 2.3.2), an induction period was not observed for either the ^{60}Co or HFIR SNF irradiation of $UO_2F_2{\bullet}xH_2O$. The production of gas was observed to occur immediately upon inserting the samples into the radiation source. The induction period has been interpreted as gas being trapped in the crystal matrix before diffusing out to the gas space. Induction, then is a diffusion-related phenomenon and, therefore, is particle-size dependent. For the $UO_2F_2 \cdot xH_2O$, it appears that the gas is immediately released with little, if any concentration buildup before release.

The pressure curves for the samples loaded in air (S-1 and S-3) both showed an initial decrease in the pressure, followed by a pressure increase (see Figs. 4.1 and 4.2). Such a pressure decrease has been observed for other materials that were irradiated in a closed, air-filled container— namely, gamma radiolysis of uranium oxide samples that had sorbed water on them (Icenhour, Toth, and Luo 2000) and alpha radiolysis of sorbed water on plutonium oxides (Mason et al. 1999). The pressure decrease can be attributed to the radiolysis of moist air (see Sect. 2.4.2.1.2), which produces nitrogen oxides (Mason et al. 1999 and Livingston 1999) that are subsequently sorbed onto the UO_2F_2. Alternatively, the pressure decrease may result from O_2 depletion during localized corrosion of the sample container. Eventually, the gas production mechanism from the radiolysis of the $UO_2F_2 \cdot xH_2O$ dominates the O_2-depletion reaction, and the steady increase in pressure is observed.

Converted U_3O_8 samples were irradiated with gamma rays to directly study the types of materials that will be placed into long-term storage. Unlike the gamma-irradiated $UO_2F_2 \cdot xH_2O$ samples, the irradiation of the converted U_3O_8, which had a fluorine content of about 1.4 wt %, did not show a pressure increase. Each of the U_3O_8 samples (after irradiation up to 2.2×10^8 rad for the ^{60}Co source and 3.0×10^{10} rad for the

HFIR SNF elements, respectively) were assigned G-values of zero molecules of gas produced per 100 eV.

5.2 GAS COMPOSITION

The gas analysis results from the irradiated $UO_2F_2{\bullet}xH_2O$ samples showed that O_2 and CO_2 were produced. Additionally, for the air-loaded samples, a significant amount of H_2 was measured. Prior to these irradiation experiments, programmatic concerns were that either F_2 or HF would be produced during gamma irradiation. However, the gas analyses clearly reveal that F_2 and HF are not produced.

The results of the gas analyses are discussed in the following subsections. The discussion is divided into two parts, based on the initial sample atmosphere. Results from samples loaded in air are discussed in Sect. 5.2.1, while results from samples loaded in helium are discussed in Sect. 5.2.2.

5.2.1 Samples Loaded in Air

Gas analyses of the irradiated $UO_2F_2{\bullet}xH_2O$ samples loaded in air showed that H_2 and CO_2 were produced. The initial presence of air in the sample gas complicates the evaluation of which gases were produced by radiolysis. Additionally, corrosion may have been responsible for the H_2 generation. However, some insight into the evaluation of which gases were produced by radiolysis can be gained by comparing the final gas composition to an inert component of the air, namely argon that acts as an internal standard. In Table 5.1 the ratios of the volume percent of the gases O_2, CO_2, N_2, and H_2

Table 5.1. Comparison of gas composition relative to argon for a standard air composition, nonirradiated blanks, and irradiated samples

Ratio	Standard air composition[a]	Nonirradiated blanks		Irradiated samples		
		S-8	S-22	Air blank (S-21)	S-1	S-3
O_2:Ar	22.47	0.32	0.005	17.64	4.04	0.03
CO_2:Ar	0.03	0.51	0.20	0.20	16.17	8.46
N_2:Ar	83.98	80.93	82.65	75.63	81.69	87.24
H_2:Ar	0.00005	8.43	364.0	0.03	8.23	6.67

[a] CRC 1992.

relative to the volume percent of Ar are provided for a standard air composition, the nonirradiated blanks (S-8 and S-22), and for the irradiated samples (the air blank, S-1, and S-3).

In Table 5.1, a comparison of the standard air composition with that for the irradiated air blank (S-21) shows a slight depletion of the O_2 and a slight elevation of CO_2 and H_2 levels. However, there were no overall large changes caused by irradiation. On the other hand, for the nonirradiated blanks, S-8 and S-22, and for the irradiated samples, S-1 and S-3, the amount of O_2 is clearly depleted. The CO_2 in the nonirradiated blanks is slightly increased, while the CO_2 level is significantly increased in the irradiated samples S-1 and S-3. Finally, the amount of H_2 in both the nonirradiated blanks and the irradiated samples (except for S-21, the air blank) shows a significant increase over the expected value. In each of the samples, the amount of N_2 is close to the expected value.

From examination of Table 5.1, it appears that the CO_2 production is a result of irradiation of the $UO_2F_2{\bullet}xH_2O$ samples. It is proposed that the gamma irradiation of the UO_2F_2 releases O radicals, which may form O_2 or which may react with carbon impurities to form CO_2. This mechanism is discussed further with respect to the irradiated samples that were loaded in helium (Sect. 5.2.2).

Hydrogen production is common to both the nonirradiated and the irradiated samples (except for the irradiated air blank). Therefore, the hydrogen may have resulted from a chemical, rather than a radiolytic, reaction. The likely reaction resulting in hydrogen production is corrosion.

Uranyl fluoride solutions are acidic and have been shown to corrode metals (Lane, MacPherson, and Maslan 1958). The corrosion rates of several alloys, including type 304L stainless steel, were measured by Lane, MacPherson, and Maslan (1958). The alloys were exposed to 0.17 *M* UO_2F_2 at 250°C in both static and flowing systems. Myers (1990) reports that the solubility of UO_2F_2 in water is about 5.2 *M* at 25°C. For the corrosion tests with the UO_2F_2 solution at the elevated temperature, corrosion rates of 0.1 to 0.33 mm (4 to 13 mil)/year were reported. It was found in these experiments for static systems that, after about 100 h of exposure, a protective layer formed on the metal surface and that the corrosion rate was then reduced to less than 0.0025 mm/year (0.1 mil/year). On the other hand, for flowing systems, if the flow rate is high enough, the corrosion continues at the higher rate—presumably because the protective layer is not allowed to form; instead it is swept away in the flow.

The blank, nonirradiated samples of $UO_2F_2 \cdot xH_2O$ consisted of $UO_2F_2 \cdot 1.7H_2O$ loaded in air (S-8), $UO_2F_2 \cdot 2.3H_2O$ loaded in air (S-22), and $UO_2F_2 \cdot 1.4H_2O$ loaded in helium (S-20). For the samples loaded in air, gas analysis showed that H_2 was produced and that O_2 was depleted. For the helium-loaded sample, a small amount of H_2 was found. The H_2 production is the result of corrosion of the stainless steel container. Additionally, similar to other corrosion phenomena, the presence of O_2 in the sample atmosphere may enhance the corrosion rate (Flinn and Trojan 1981). The corrosion of the sample container S-22 is clearly evident from examination of Fig. 4.11. The corrosion seen on the container wall is consistent with the fact that a large amount of H_2 was produced inside this container. Metallographic examination of container S-8 did not show significant changes from the unexposed material. However, a much smaller amount of H_2 was produced inside this container.

Both of the air-loaded samples were prepared in a humid environment to maximize the water-loading of the sample. It is possible that very small amounts of condensed water could form on the sample, resulting in locally high concentrations of acidic UO_2F_2 solution in contact with the container walls. Corrosion of the walls would result in H_2 production. For sample S-22, based on the container pressure, it is estimated that about 7×10^{-4} moles of H_2 were formed. Only a small amount of corrosion would be required to produce this small volume of gas. (Pressure data were not available for sample S-8.) The rate of pressure increase for S-22 was not seen to plateau, as would be expected based on the uranyl fluoride solution experiments. The amount of corrosion may have been so small relative to the available surface area that a passive layer, adequate to noticeably retard the corrosion rate, was not formed. Finally, the lower hydrate sample (S-8) exhibited a lower total production of H_2 than did the higher hydrate (S-22). In this case, there is less acidic liquid phase in contact with the container walls and, hence, lower H_2 production.

The reduced O_2 content in both the blanks and the irradiated samples may have resulted from corrosion. However, in the case of the irradiated samples, another mechanism may have contributed to the O_2 depletion. The radiolysis of moist air produces nitrogen oxides (see Sect. 2.4.2.1.2) that may sorb onto solid surfaces. Recent work at ORNL with gamma-irradiation of uranium oxides loaded in air (Icenhour, Toth, and Luo 2000) and at Los Alamos National Laboratory (LANL) for alpha-irradiation of plutonium oxides loaded in air (Mason et al. 1999) have shown a pressure decrease during irradiation. This decrease has been attributed to the radiolytic production of nitrogen oxides, which sorb onto the uranium or plutonium oxide (Livingston 1999, Mason et al. 1999). Neither uranium oxide nor plutonium oxide form acidic solutions, such as those described for UO_2F_2. Therefore, in those systems, it is not likely that the O_2 was consumed in corrosion. On the other hand, the N_2:Ar ratios in each of the samples in Table 5.1 are consistent with those expected from the standard air composition. It is not clear whether any N_2 has been depleted; therefore, there is no conclusive evidence for the nitrogen-oxide-production mechanism. In any event, the exact fate of the O_2 in the irradiated samples is not known. The O_2 may have been consumed during corrosion, during NO_x production, or by some combination of both of these mechanisms. Furthermore, it is proposed that the radiolysis of UO_2F_2 results in the release of

O radicals, forming either O_2 or CO_2. This radiolytic source of O_2 may have also been depleted by the proposed mechanisms—corrosion and/or production of nitrogen oxides.

Finally, because it appears that the H_2 produced in samples S-1 and S-3 is only from corrosion and not from some radiolytic reaction, the G(gas)-values calculated for these experiments may be too high. Recalling that the G(gas)-value was based on the total pressure increase for a sample, it is necessary to remove the H_2 component from the calculation to obtain a better estimate of the G(gas)-value resulting from radiolytic production. From the gas compositions reported for S-1 and S-3, it is estimated that the true G(gas)-value is about 60–70% of the value given in Sect. 3—hence, G(gas) ~ 0.007 molecules gas per 100 eV for S-1 and G(gas) ~ 0.012 molecules gas per 100 eV for S-3.

5.2.2 Samples Loaded in Helium

To remove the complication of the initial presence of O_2 in the cover gas, similar runs were made with samples loaded in helium. For the gamma irradiation of these $UO_2F_2 \bullet xH_2O$ samples, the gases produced were either O_2 or CO_2. A trace of H_2 was reported for each of these samples. However, the amount of H_2 is close to that for the nonirradiated blank of $UO_2F_2 \bullet 1.4H_2O$, which was loaded in helium. Thus, the H_2 may have resulted from an extremely small amount of corrosion of the sample container by the $UO_2F_2 \bullet xH_2O$.

It appears that O_2 is released during the irradiation of the $UO_2F_2 \bullet xH_2O$ samples and that some of the O_2 reacts with carbon impurities in the samples to produce CO_2. The observation regarding the O_2 release is consistent with the experimental results for the mixed-bonding crystals, as described in Sect. 2.3.3. In those crystals, the covalent portion of the crystal was damaged (releasing O_2 or N_2). A similar effect is seen in gamma-irradiated $UO_2F_2{\bullet}xH_2O$.

To confirm the hypothesis regarding the carbon, a sample of $UO_2F_2{\bullet}0.4H_2O$ was burned in O_2 to remove some of the carbon. FTIR analysis of the off-gas during burning revealed that CO_2 was produced. ATR analysis of the sample after burning showed that the material was anhydrous UO_2F_2. Irradiation of the *unburned* $UO_2F_2{\bullet}0.4H_2O$ (both by the ^{60}Co source and HFIR SNF elements) resulted in the production of CO_2 and a small amount of O_2. By comparison, after the ^{60}Co irradiation of the *O_2-burned* UO_2F_2, the gas composition was primarily O_2 and a lesser amount of CO_2. Removal of some of the carbon from the UO_2F_2 sample by burning in oxygen resulted in less carbon being available for reaction and, therefore, more O_2 being produced. Hence, it is clear that O_2 is the primary gas released by gamma irradiation of $UO_2F_2{\bullet}xH_2O$ and that some of the O_2 (or O radicals) reacts with carbon impurities to form CO_2.

The irradiation of the converted U_3O_8 samples, which were loaded in helium, did not show a pressure rise. The gas analyses for these samples revealed that only a very small amount of CO_2 and O_2 were present. These gases may have been produced from the samples, but the amount was so small that it did not contribute to any discernable pressure increase. Because of the high dose given to the U_3O_8 sample in the HFIR SNF elements, *it is clear that large amounts of gas will not be produced by gamma radiolysis of this material.*

5.3 VALENCE CHANGE

The color change of the $UO_2F_2 \bullet xH_2O$ from yellow to green, especially evident in the higher hydrates, indicated that some of the uranium may have been reduced from U(VI) to U(IV). This observation was confirmed by the Davies-Gray analysis of samples before and after irradiation. The analysis presented herein assumes that the uranium is present as U(IV) and not U(V) even though in the dissolution of the uranium sample for the Davies-Gray titration, any U(V) that is present will disproportionate to U(IV) and U(VI). This assumption is consistent with the observed color change of the $UO_2F_2 \bullet xH_2O$ from yellow to green— typical of U(IV).

In general (except for sample S-16), after irradiation, the amount of U(IV) in each of the $UO_2F_2 \bullet xH_2O$ samples was found to increase (Table 4.11). This increase indicates a reduction of some of the U(VI) to U(IV), which could be accomplished by the release of oxygen from the UO_2F_2, as indicated by

$$UO_2F_2 + h\nu \rightarrow UOF_2 + O \,. \tag{5.1}$$

The results of the Davies-Gray analyses (Table 4.11) showed an interesting trend. The lower hydrates (i.e., $x \sim 0.4$) had a larger increase in percentage of U(IV) than did the higher hydrates. The exception to this trend, which is discussed later in this subsection, is sample S-16 (the O_2-burned UO_2F_2). It appears that the oxidizing species, produced by the radiolysis of the water of hydration or moist air, oxidize the uranium, thereby limiting the U(IV) production. Such reactions are indicated by:

$$UOF_2 + OH \rightarrow UO_2F_2 + H \quad \text{and} \tag{5.2}$$

$$UOF_2 + NO_x \rightarrow UO_2F_2 + NO_{x-1} \qquad (5.3)$$

This observation, regarding the amount of U(IV) production relative to the degree of hydration of the UO_2F_2, is consistent with the experimental evidence described in Sects. 2.4.2.1.1 and 2.4.2.1.2. In these sections, the oxidation of UO_2 by oxidizing species (e.g., OH and NO_x) produced by the radiolysis of sorbed water or moist air was discussed. Similar mechanisms may be occurring for the irradiation of $UO_2F_2 \bullet xH_2O$.

One of the irradiated samples, S-3, was heated to 200°C, first in vacuum and then in air. Subsequent chemical analysis of this material revealed a decrease in the U(IV) content, suggesting a back reaction of the reduced uranium with oxygen during the air-heating phase.

With respect to valence change, sample S-16 did not exhibit the same behavior as did the other irradiated $UO_2F_2 \bullet xH_2O$ samples. S-16 was prepared by heating $UO_2F_2 \bullet 0.4H_2O$ in an O_2 atmosphere at 500–550°C. Davies-Gray analysis of the heated sample revealed that a small amount of U(IV) had been produced. This observation is consistent with the fact that UO_2F_2 disproportionates to UF_6 and U_3O_8 upon heating. Ferris and Baird (1960) reported that UO_2F_2 was stable in a dry atmosphere below 700°C. However, because a hydrate of UO_2F_2 was heated in a closed system, there was moisture in the system. Indeed, moisture was observed to condense at the cool ends of the silica tube during the heat treatment. Additionally, after treatment, black specks were observed on the sample container. These specks were likely U_3O_8 and, hence, it appears that a small amount of UO_2F_2 disproportionated to U_3O_8 and UF_6.

Most of the $UO_2F_2 \bullet xH_2O$ exhibited an increase in the amount of U(IV) after irradiation. However, sample S-16 showed that the U(IV) content decreased, *indicating a net oxidation in the sample.* Similar to the $UO_2F_2 \bullet xH_2O$ samples, this sample also released O_2 and CO_2 upon irradiation. Irradiation of the UO_2F_2 releases O_2 from the sample, resulting in a *reduction* of the uranium from U(VI) to U(IV). However, subsequent *oxidation* of uranium by this source of oxygen would not explain the net oxidation of the sample. Another source of oxygen must be available, and it appears that the source may be in the U_3O_8 produced by the O_2-burning of the $UO_2F_2 \bullet 0.4H_2O$.

Kraus (1944) and Katz and Rabinowitch (1951) reported that superoxides of uranium (i.e., O:U molar ratio > 3) are formed when uranium oxides are heated in O_2. Kraus thermally decomposed $(NH_4)_2\ U_2O_7$ in O_2 at temperatures from 350 to 550°C. During the heating of the sample, NH_3 and H_2O evolved in the temperature range of 250 to 350°C. Above 350°C, Kraus reported that little or no NH_3 evolved. Analysis of the samples showed that a superoxide had been formed, with O:U ratios ranging from 3.14 to 3.38, depending on the heating time and temperature. When the sample was dissolved in water, oxygen was released.

The heat treatment of the $UO_2F_2 \bullet 0.4H_2O$ is similar to that performed by Kraus (1944). The $UO_2F_2 \bullet xH_2O$ was heated to 550°C in an O_2 atmosphere. Thermal decomposition of the sample appears to have formed a small amount of U_3O_8. Under these conditions, the U_3O_8 can take additional oxygen into the crystalline lattice, which would be released during dissolution of the sample for Davies-Gray titration.

It is proposed then, that the O_2-burned UO_2F_2 sample (S-16) contained a mixture of UO_2F_2 and a small amount of a superoxide of uranium (namely, U_3O_8 with excess O_2 in the matrix). Upon irradiation of this material, the UO_2F_2 is radiolyzed, releasing O_2. Radiation also causes a release of oxygen from the uranium superoxide. This "excess" oxygen is also available to oxidize uranium. Hence, oxygen (or CO_2) is released from the sample (a uranium reduction), but uranium is also oxidized by some of the released oxygen—the net effect being a slight oxidation of the sample.

In Sect. 4.3.2.1, a comparison was made of the number of moles of U(IV) produced and the number of moles of O_2 (either as O_2 or CO_2) produced (Table 4.12). If all the U(IV) production resulted in O_2 (or CO_2), then for every mole of U(IV), there would be 0.5 mol of O_2. The ratio of moles of O_2 and CO_2 to the moles of U(IV) varied from 0.08 to 0.4. These ratios indicate that some of the O_2 produced was either trapped in the UO_2F_2 matrix or otherwise scavenged (i.e., through corrosion or other reactions). However, insufficient evidence exists to firmly establish the fate of the oxygen that is not manifested in the gas as either O_2 or CO_2.

Finally, the U(IV) production in the irradiated $UO_2F_2{\bullet}xH_2O$ samples provides a measure of the radiation damage to the UO_2F_2 matrix. *Damage*, in this case, is defined as the percentage of U(IV) produced. Based on the change in the percentage of U(IV) in the samples (Table 4.11), the ^{60}Co irradiations produced damages ranging from 0.3 to 1.5%. However, the quantity of most interest is the maximum damage limit to the $UO_2F_2{\bullet}xH_2O$. This quantity was measured by performance of the HFIR SNF irradiations, which reached a limiting pressure plateau. The Davies-Gray analysis for this material revealed a damage of about 7–9%. Because a limiting pressure (or steady state) was reached, this U(IV) production corresponds to the damage limit for the $UO_2F_2 \cdot xH_2O$ at the maximum SNF element dose rate (~10^8 rad/h).

5.4 SUMMARY

The results of the observed pressure increases, gas compositions, and valence changes, when considered in total, give a clear picture of the radiolytic effects on the $UO_2F_2 \cdot xH_2O$. The results of the gamma irradiation experiments have shown that gamma radiation interacts with the uranyl (UO_2^{2+}) group of the UO_2F_2, releasing O radicals and resulting in uranium reduction to U(IV).

Intuitively, it might be expected that F_2 (or HF in the presence of H_2O) would be released by the irradiation of UO_2F_2. Because the uranium-oxygen bond energies (in the UO_2^{2+}) are greater than those of metal fluorides (Denning 1992, Cottrell 1958), one might expect that the fluorine bonds would be more easily broken than the oxygen bonds. Additionally, this intuitive expectation comes from the experience with the radiolysis of the MSRE fluoride salts. In these ionic materials, fluorine was released upon gamma-irradiation. On the other hand, UO_2F_2 is better characterized as a crystal with mixed bonding, because it consists of uranyl and fluorine ions, but at the same time, contains the covalently bonded uranyl group. Therefore, expectations of radiation effects on UO_2F_2 would be better based on crystals that have mixed bonding. In Sect. 2.3.3, the effects of radiation on crystals with mixed bonding were described. In the case of irradiated $Ba(NO_3)_2$, $NaNO_3$, KNO_3, and $KClO_3$, it was reported that O_2 was released from these crystals (usually during heating or dissolution of the crystal). The irradiation of NaN_3 resulted in the production of N_2. The authors of these experiments attributed the production of O_2 or N_2 to an ionization-excitation mechanism in which O or N radicals are formed. For these experiments, it is not believed that either the oxygen or the nitrogen were directly displaced from the matrix by the incident radiation.

Similarly, for the gamma-irradiated UO_2F_2, the UO_2^{2+} group may be excited or ionized by the incident radiation, resulting in the release of an O radical. Alternatively, electrons, produced in ionization, may cause displacement of oxygen from the matrix, or, possibly, the gamma radiation does directly displace oxygen from the matrix. Of course, other potential mechanisms involving complicated radiochemical reactions may explain the production of the oxygen. More detailed, solid-state radiation experiments would be required to unravel the exact mechanism or mechanisms resulting in O_2 production. Regardless of the underlying mechanism, however, it is clear that the gamma irradiation of UO_2F_2 produces O_2. This observation is consistent with the experimental results found for other crystals that have mixed bonding. The fluorine component of the UO_2F_2 has been shown to be insensitive to gamma irradiation. The ionic nature of the fluorine in the crystal may enhance its ability to withstand radiation damage, whereas the covalently bonded oxygen is released during irradiation. Additionally, this observation is consistent with the generalization provided by Billington and Crawford (1961)—"structural alterations are less pronounced the greater the ionic character of the bonding" (Sect. 2.3.1).

The radiolytic effects of gamma irradiation of $UO_2F_2 \bullet xH_2O$ are summarized in the following paragraphs. Gamma radiation interacts with the UO_2F_2, releasing O radicals and reducing the uranium to U(IV), as indicated in the following equation:

$$UO_2F_2 + h\nu \rightarrow UOF_2 + O \qquad (5.4)$$

The O radicals react with each other to produce O_2 or react with carbon impurities in the sample to produce CO_2:

$$O + O \rightarrow O_2 \ , \qquad (5.5)$$

$$O + C \rightarrow CO \ , \text{ and} \qquad (5.6)$$

$$CO + O \rightarrow CO_2 \ . \qquad (5.7)$$

Some of the O_2 may be trapped in the UO_2F_2 matrix or otherwise consumed. The UO_2F_2 consists of stacked layers, with UO_2^{2+} ions normal to each layer (with a double-bonded oxygen above and below each plane) and fluorine atoms surrounding the uranium in its equatorial plane. This relatively open structure allows for the oxygen to be readily released from the matrix and explains the lack of an induction period seen in other materials. The released O_2 (or O_2 in the form of CO_2) causes a pressure increase in the irradiation container. This increase can be used to estimate the gas yield. Hence, the G(gas) values reported in Sect 4.1 (and modified in Sect. 5.2.1 to account for H_2 production by corrosion) are actually $G(O_2)$-values. The $G(O_2)$-values for the gamma irradiation of $UO_2F_2 \bullet xH_2O$ varied from 0.007 up to 0.03 molecules of O_2 per 100 eV, depending on the amount of hydration and the atmosphere over the sample. The amount of reduction in a given sample may be related to the amount of hydration of the sample. Back reactions with oxidizing species produced from the radiolysis of water or moist air may lower the reduction rate of uranium [e.g., Eqs. (5.2) and (5.3)].

During irradiation, back reactions may occur, such as

$$UOF_2 + O \rightarrow UO_2F_2 \quad \text{or} \tag{5.8}$$

$$UOF_2 + 1/2O_2 \rightarrow UO_2F_2. \tag{5.9}$$

At some point, a steady state is reached for a given dose rate in which the forward reaction [Eq. (5.4)] rate equals the back reaction [Eqs. (5.8) or (5.9)] rate. A change in the dose rate would result in a change in the steady-state level (as demonstrated for the HFIR SNF irradiations). At this steady state, the maximum damage limit to the UO_2F_2 matrix is realized; this limit is about of 7 to 9% of U(IV) produced for the high dose rates available with HFIR SNF elements (~10^8 rad/h). Hence, the radiation damage reaches a saturation point, similar to other crystalline solids described in Sect. 2. Additionally, the damage limit to the ionic LiF-BeF_2 crystals has been shown to be about 2% at the same dose rate as that used for the $UO_2F_2 \bullet 0.4H_2O$ sample. The higher limit for the UO_2F_2 is further evidence that the covalently bonded UO_2^{2+} group is more susceptible to radiation damage than is the ionically bonded fluorine.

6. CONCLUSIONS AND RECOMMENDATIONS

Conclusions from this dissertation are discussed in Sect. 6.1, while recommendations for further work are outlined in Sect. 6.2.

6.1 CONCLUSIONS

The objective of this effort was to evaluate radiolytic effects on residual fluoride impurities in uranium oxides and on the oxide, itself. This objective was approached through study of relevant literature and through performance of radiolysis experiments to demonstrate radiolytic effects on U_3O_8 and fluoride impurities. Background information concerning the interaction of radiation with crystalline solids was provided. This background discussion was focused on radiolytic effects based on the type of bonding—covalent, ionic, and mixed-bonding crystals. The mixed-bonding crystals, containing both covalent and ionic components, proved to be the best model for the impurities (i.e., the $UO_2F_2{\bullet}xH_2O$) studied in the radiolysis experiments. The effects of radiation on uranium oxides was also reviewed. This review was divided into two major areas—chemical (i.e., oxidation) and structural changes.

The radiolysis experiments were focused primarily on the gamma irradiation of $UO_2F_2{\bullet}xH_2O$ because (a) it is an intermediate compound formed during the conversion of UF_6 to U_3O_8, (b) it is the most probable form of the residual fluoride in the U_3O_8, and (c) it represents the maximum fluoride content of a material that could be placed into storage (i.e., resulting from the partial conversion of UF_6 to U_3O_8).

Gamma irradiation of various $UO_2F_2 \cdot xH_2O$ compounds that were loaded in different atmospheres (either air or helium) resulted in the production of O_2 or CO_2. Some H_2 was produced also (particularly in the samples loaded in air), but the H_2 was found to be the result of corrosion and not radiolytic reactions. Neither F_2 nor HF was produced by the irradiations.

The pressure in the sample containers was shown to rise very slowly during irradiations in the ^{60}Co source. Irradiation at higher dose rates and to higher total doses, using HFIR SNF elements, showed that a limiting-pressure plateau was reached. The total pressure rise in the HFIR SNF irradiations, like all of the experiments performed with the ^{60}Co source, was less than 1 atm.

Analysis of solid samples following irradiation showed that some of the uranium had been reduced from U(VI) to U(IV). This result, combined with the O_2 and CO_2 release from the samples, led to the conclusion that O_2 was released from the UO_2F_2 by gamma irradiation. It was demonstrated that the CO_2 was produced by interaction of the released oxygen with carbon impurities in the sample.

The pressure rise in the sample containers, as a function of dose to the sample, was used to estimate the maximum $G(O_2)$-values for the gamma irradiation of $UO_2F_2 \cdot xH_2O$. The G-value goes to zero as a plateau (i.e., saturation) is approached. The maximum $G(O_2)$-values ranged from 0.007 to 0.03 molecules of O_2 produced per 100 eV. Apparently, there is some dependence of the $G(O_2)$-values on the degree of hydration of the UO_2F, and on the initial atmosphere over the sample. The radiolysis of either the waters of hydration or moist air may produce oxidizing species that limit the amount of uranium reduction.

A saturation damage limit for the $UO_2F_2 \cdot xH_2O$ was demonstrated using the HFIR SNF elements. At saturation, the rate of radiolytic production (i.e., the uranium reduction) equals the recombination rate (i.e., the uranium oxidation). Damage was measured in terms of the percentage of U(IV) production and was found to be about 7–9% in $UO_2F_2 \cdot xH_2O$. This limit is for the highest dose rate available in the HFIR SNF elements (~10^8 rad/h) and should be a bounding value. In contrast, the damage limit to the ionic LiF-BeF_2 salt has been demonstrated by Toth and Felker (1990) to be about 2%. Hence, under the same gamma dose rate, the covalently bonded oxygen is more susceptible to radiation damage than is the ionically bonded fluorine.

A comparison of the amount of U(IV) produced with the amounts of O_2 and CO_2 produced demonstrated that not all of the oxygen was released as gas. Some of the oxygen may have remained trapped in the crystal structure of the $UO_2F_2 \cdot xH_2O$ or may have been otherwise scavenged.

Samples of U_3O_8, which were produced in the ORNL conversion prototype and that contained about 1.4 wt.% fluorine, were irradiated in the ^{60}Co source and in HFIR SNF elements. These samples showed no pressure rise, and neither F_2 nor HF was produced. This material is representative of that which may be placed into long-term storage.

Based on this work, the following conclusions can be made about uranium oxides that are converted from UF_6. Recall that for long-term storage of converted uranium oxides, the production of corrosive gases or overpressurization of storage containers are of concern. However, for gamma radiolysis, the residual fluoride content is not limiting. As demonstrated by the experiments, radiolysis of $UO_2F_2 \bullet xH_2O$ produces only O_2 and CO_2—not F_2 nor HF. Also, it has been demonstrated that a limiting pressure, which is less than 1 atm, is reached by the gamma radiolysis of $UO_2F_2 \bullet xH_2O$. Therefore, with respect to gamma radiolysis, even $UO_2F_2 \bullet xH_2O$ would not present a long-term storage problem. Of course, because $UO_2F_2 \bullet xH_2O$ is highly soluble and because it can cause corrosion, this material itself would not be suitable for long-term storage. Based on this experimental evidence, gamma radiolysis of converted U_3O_8 that contains residual fluorine impurities will not produce deleterious products or pressures. Certainly the product quality produced by the ORNL conversion prototype (< 1.4 wt % fluorine) will be acceptable for long-term storage.

6.2 RECOMMENDATIONS

During the course of this work, a number of areas for further investigation were identified. These areas are briefly outlined in this subsection.

6.2.1 Alpha Radiolysis Experiments

The radiolysis experiments conducted for this work demonstrated the effects of gamma radiation on $UO_2F_2 \bullet xH_2O$. Uranium-233 and ^{232}U have a high alpha activity in addition to a high gamma dose rate (see Fig. 1.1). Alpha particles cause higher density ionization tracks than do gamma rays. These higher density tracks may cause different effects in the solid. Note that alpha radiolysis experiments performed by Toth (1990) on MSRE-type salts showed no pressure rise after 18 months, while gamma irradiation of the same type of material resulted in production of F_2 (Toth and Felker 1990, Williams, Del Cul, and Toth 1996). On the other hand, alpha radiolysis experiments on water sorbed on plutonium oxides loaded in air (Mason et al. 1999, Livingston 1999) have shown results similar to those from experiments conducted with gamma radiolysis of water sorbed on uranium oxides loaded in air (Icenhour, Toth, and Luo 2000). Therefore, alpha radiolysis experiments will be needed to help complete the understanding of the radiolysis of UO_2F_2 and associated fluoride impurities in U_3O_8. Such experiments could be conducted by doping UO_2F_2 samples with high specific activity alpha emitters, such as ^{238}Pu or ^{244}Cm. Similar to the gamma radiolysis experiments, pressure could be monitored and gas samples periodically taken to understand the radiolytic yield.

6.2.2 Underlying O_2 Production Mechanism

The radiolysis experiments for $UO_2F_2{\bullet}xH_2O$ identified that O_2 was produced and that some of the uranium was reduced from U(VI) to U(IV). However, more detailed solid-state radiolysis experiments, using sophisticated, surface-analysis techniques, are required to increase our understanding of the underlying mechanism for oxygen production and migration. Such a fundamental understanding could be used in the development of a model for the irradiation of $UO_2F_2{\bullet}xH_2O$. Irradiation experiments, coupled with techniques such as electron spin resonance, may help to identify the species of oxygen produced by the interaction of the radiation with the $UO_2F_2{\bullet}xH_2O$. Such understanding may also help to understand the fate of the oxygen that is not manifested as O_2 in the gas space. Such oxygen may remain trapped in the crystal matrix or is otherwise consumed.

Insight into the fate of the O_2 might also be gained by correlating the O_2 yield with powder size. Additional evidence of trapped O_2 might be provided if it is found that the higher surface area powders have a larger O_2 yield than do the lower surface area powders.

6.2.3 Higher Resolution Pressure Data in HFIR SNF Irradiations

The use of an analogue pressure gage (read only twice daily) limited the resolution of the data available during the HFIR SNF irradiation. However, it was the simplicity of the design that allowed its installation into HFIR SNF elements. Higher-resolution data could be obtained by the use of a pressure transducer, which would allow continuous data logging.

6.2.4 Radiolysis of other Fluorides and Oxyfluorides

To broaden the understanding of the radiolysis of fluorides and oxyfluorides, studies could be performed on other materials (e.g., plutonium oxyfluorides, zirconium oxyfluorides, and uranium tetrafluoride). These studies could provide information on the influence of the bonding characteristics and other factors on radiolytic effects.

6.2.5 O_2 Depletion in Air-Loaded Samples

Gas samples from containers loaded with $UO_2F_2 \cdot xH_2O$ in air, both irradiated and unirradiated, showed that O_2 was depleted. In the case of the unirradiated samples, O_2 was likely depleted by corrosion. However, in the case of the irradiated samples, O_2 may have been depleted by an additional mechanism—namely, radiolysis of moist air forming nitrogen oxides that sorb onto the surface of the $UO_2F_2 \cdot xH_2O$. This mechanism has been used to explain pressure decreases that were observed in radiolysis experiments for other types of materials (Mason et al. 1999, Livingston 1999). Further experimentation would be required to confirm this mechanism in the case of the $UO_2F_2 \cdot xH_2O$. Analysis of sample surfaces for nitrogen oxides might reveal their presence.

6.2.6 Effect of Radiation on H_2 Production

It was found that H_2 was produced by localized corrosion of the stainless steel container by the $UO_2F_2 \cdot xH_2O$. What is not clear, however, is what role that radiation may play in retarding the H_2 production. It is possible that radiolytically produced species may react with the corrosion-produced H_2 and limit the total amount of H_2 produced. It is not clear from the experiments performed on the $UO_2F_2 \cdot xH_2O$ whether radiation resulted in more or less H_2 production. Experiments could be performed that explore the relationship of the H_2 production and radiation.

REFERENCES

REFERENCES

Allen, A. O., and J. A. Ghormley, 1947. "Decomposition of Solid Barium Nitrate by Fast Electrons," *J. Chem. Phys.* **15**(4), 208–209.

Allen, A. O., et al., 1952. "Decomposition of Water and Aqueous Solutions under Mixed Fast Neutron and Gamma Radiation," *J. Phys. Chem.* **56**, 575–586.

Anderson, J. S., L. E. J. Roberts, and E. A. Harper, 1955. "The Oxidation of Uranium Dioxide," *J. Chem. Soc.* 3946–3959.

Armstrong, D. P., et al., 1991. "An FT-IR Study of the Atmospheric Hydrolysis of Uranium Hexafluoride," *Applied Spectroscopy* **45**(6), 1008–1016.

ASTM C753–94, December 1994. *Standard Specification for Nuclear-grade, Sinterable Uranium Dioxide Powder*, American Society for Testing and Materials, Philadelphia.

ASTM C776–94, December 1994. *Standard Specification for Sintered Uranium Dioxide Pellets*, American Society for Testing and Materials, Philadelphia.

ASTM E666-91, 1991, *Standard Practice for Calculating Absorbed Dose from Gamma and X Radiation*, American Society for Testing and Materials, Philadelphia, Pennsylvania.

Atoji, M., and M. J. McDermott, 1970. "The Crystal Structure of Anhydrous UO_2F_2," *Acta Cryst.* **B26**, 1540–1544.

Baran, V., 1993. *Uranium (VI) - Oxigen Chemistry, Uranyl Hydroxo Complexes, Uranates and Oxides*, Hadronic Press, Inc., Palm Harbor, Florida.

Barr, J. T., and C. A. Horton, 1952. "Some New Uranium Complexes," *J. Amer. Chem. Soc.* **74**, 4430–4435.

Belle, J., 1961. *Uranium Dioxide: Properties and Nuclear Applications*, U.S. Atomic Energy Commission, Washington, D.C.

Billington, D. S., and J. H. Crawford, 1961. *Radiation Damage in Solids*, Princeton University Press, Princeton, New Jersey.

Brady, J. E., and G. E. Humiston, 1982. *General Chemistry, Principles and Structure*, John Wiley and Sons, New York.

Cagle, G. W., June 25, 1997. Lockheed Martin Energy Systems, Inc., Y-12 Plant, Oak Ridge, Tennessee, personal communication to A. S. Icenhour, Lockheed Martin Energy Research Corp., Oak Ridge National Laboratory, Oak Ridge, Tennessee.

Campbell, T. K., E. R. Gilbert, G. D. White, G. F. Piepel, and B. J. Wrona, 1989. "Oxidation Behavior of Nonirradiated UO_2," *Nucl. Technol.* **85**, 160–171.

Compere, E. L., et al. October 1975. *Fission Product Behavior in the Molten Salt Reactor Experiment*, ORNL-4865, Union Carbide Corp., Oak Ridge National Laboratory, Oak Ridge, Tennessee.

Cottrell, T. L., 1958. *The Strengths of Chemical Bonds*, Butterworths Scientific Publications, London.

Crawford, J. H., and M. C. Wittels, 1956. "A Review of Investigations of Radiation Effects in Covalent and Ionic Crystals," pp. 654–665 in *Proc. International Conference on Peaceful Uses of Atomic Energy*, United Nations.

CRC 1992. *CRC Handbook of Chemistry and Physics*, 73rd Ed., D. R. Lide, ed.,CRC Press, Boca Raton, Florida.

Davies, W., and W. Gray, 1964. "A Rapid and Specific Titrimetric Method for the Precise Determination of Uranium using Iron (II) Sulfate as Reductant," *Talanta* **11**, 1203.

Del Cul, G. D., A. S. Icenhour, and L. M. Toth, November 18, 1997. *Conversion of Uranium-Containing Materials Retrieved from the Molten Salt Reactor Experiment (MSRE) into Stable Oxides for Final Storage/Disposition*, ORNL/CF-97/41, Lockheed Martin Energy Research Corp., Oak Ridge National Laboratory, Oak Ridge, Tennessee.

Denning, R. G., 1992. "Electronic Structure and Bonding in Actinyl Ions," pp. 215–276 in *Complexes, Clusters, and Crystal Chemistry*, Springer-Verlag, New York.

Dillow, T. A., April 16, 1998. Lockheed Martin Energy Research Corp., Oak Ridge National Laboratory, Oak Ridge, Tennessee, personal communication regarding historical exposure rate measurements for the J. L. Shepherd ^{60}Co source to A. S. Icenhour, Lockheed Martin Energy Research Corp, Oak Ridge National Laboratory, Oak Ridge, Tennessee.

Dominey, D. A., 1968. "Oxidation of UO_2 by Oxygen at 66°C and 80°C," *J. Inorg. Nucl. Chem.* **30**, 1757–1760.

Eberle, A. R., and M. W. Lerner, June 1971. "Titrimetric Determination of Total Uranium and Uranium IV in Uranium Dioxide," New Brunswick Laboratory Progress Report No. 258, New Brunswick, New Jersey.

Einzinger, R. E., S. C. Marschman, and H. C. Buchanan, 1991. "Spent-Fuel Dry-Bath Oxidation Testing," *Nucl. Technol.* **94**, 383–393.

Estermann, I., W. J. Leivo, and O. Stern, 1949. "Change in Density of Potassium Chloride Crystals upon Irradiation with X-rays," *Phys. Rev.* **75**(4), 627–633.

Ferris, L. M., and F. G. Baird, 1960. "Decomposition of Uranyl Fluoride between 700° and 950°C," *J. Electrochem. Soc.* **107**, 305–308.

Flinn, R. A., and P. K. Trojan, 1981. *Engineering Materials and Their Applications*, 2nd ed., Houghton Mifflin Company, Boston.

Forsberg, C. W., December 1996. "Depleted Uranium Oxides and Silicates as Spent Nuclear Fuel WP Fill Materials," *Proc. Materials Research Society 1996 Fall Meeting: Symposium II, Scientific Basis for Nuclear Waste Management XX, Materials Research Society*, Pittsburgh, Pennsylvania.

Forsberg, C. W., et al., November 26, 1997. *Strategy for the Future Use and Disposition of Uranium-233: Disposition Options*, ORNL/MD/LTR-63, Lockheed Martin Energy Research Corp., Oak Ridge National Laboratory, Oak Ridge, Tennessee (Draft).

Forsberg, C. W., 1997. Lockheed Martin Energy Research Corp., Oak Ridge National Laboratory, Oak Ridge, Tennessee, private communication to A. S. Icenhour, Lockheed Martin Energy Research Corp., Oak Ridge National Laboratory, Oak Ridge, Tennessee.

Gilman, J. J., and W. G. Johnston, 1958. "Dislocations, Point-Defect Clusters, and Cavities in Neutron Irradiated LiF Crystals," *J. App. Phys.* **26**(6), 877–887.

Gittus, J., 1978. *Irradiation Effects in Crystalline Solids*, Applied Science Publishers Ltd., London.

Harteck, P., and S. Dondes, 1956. "Producing Chemicals with Reactor Radiations," *Nucleonics* **14**(7), 22–25.

Haubenreich, P. N., September 30, 1970. *Fluorine Production and Recombination in Frozen MSR Salts after Reactor Operation*, ORNL/TM-3144, Union Carbide Corp.–Nuclear Division, Oak Ridge National Laboratory, Oak Ridge, Tennessee.

Heal, H. G., 1953. "The Decomposition of Crystalline Sodium Azide by X Rays," *Can. J. Chem.* **31**(12), 1153–1163.

Henning, G., R. Lees, and M. S. Matheson, 1953. "The Decomposition of Nitrate Crystals by Ionizing Radiations," *J. Chem. Phys.* **21**(4), 664–668.

Hobbs, R. W., May 1995. " Irradiation History for MSRE Experiment Cell 1," Oak Ridge National Laboratory, Oak Ridge, Tennessee, unpublished.

Hubbell, J. H., 1982. "Photon Mass Attenuation and Energy-absorption Coefficients from 1 keV to 20 MeV," *Int. J. Appl. Radiat. Isot.* **33**, 1269–1290.

Icenhour, A. S., L. M. Toth, and H. Luo, 2000. *Radiation Studies on Uranium Oxides and Oxyfluorides for the Uranium-233 Storage Standard I. Interim Report*, ORNL/TM-1999/250, Oak Ridge National Laboratory, Oak Ridge Tennessee, in preparation.

Jarabek, R. J., April 2, 1984. *Transport Measurement of* UF_5 *using a Precision Analysis for* U^{+4}, K/PS-5017, Martin Marietta Energy Systems, Oak Ridge Gaseous Diffusion Plant, Oak Ridge, Tennessee.

Jarabek, R. J., May 6, 1999a. Materials and Chemistry Laboratory, Inc., Oak Ridge, Tennessee, correspondence regarding Davies-Gray titration results to A. S. Icenhour, Lockheed Martin Energy Research, Oak Ridge National Laboratory, Oak Ridge, Tennessee.

Jarabek, R. J., May 12, 1999b. Materials and Chemistry Laboratory, Inc., Oak Ridge, Tennessee, correspondence regarding Davies-Gray titration results to A. S. Icenhour, Lockheed Martin Energy Research, Oak Ridge National Laboratory, Oak Ridge, Tennessee.

Jarabek, R. J., September 23, 1999c. Materials and Chemistry Laboratory, Inc., Oak Ridge, Tennessee, correspondence regarding Davies-Gray titration results to A. S. Icenhour, Lockheed Martin Energy Research, Oak Ridge National Laboratory, Oak Ridge, Tennessee.

Jarabek, R. J., October 1, 1999d. Materials and Chemistry Laboratory, Inc., Oak Ridge, Tennessee, correspondence regarding Davies-Gray titration results to A. S. Icenhour, Lockheed Martin Energy Research, Oak Ridge National Laboratory, Oak Ridge, Tennessee.

Jarabek, R. J., October 14, 1999e. Materials and Chemistry Laboratory, Inc., Oak Ridge, Tennessee, correspondence regarding Davies-Gray titration results to A. S. Icenhour, Lockheed Martin Energy Research, Oak Ridge National Laboratory, Oak Ridge, Tennessee.

Jones, A. R., 1959. "Radiation-Induced Reactions in the N_2-O_2-H_2O System," *Radiat. Res.* **10**, 655–663.

Katz, J. J., and Eugene Rabinowitch, 1951. *The Chemistry of Uranium, Part I The Element, Its Binary and Related Compounds*, McGraw-Hill Book Company, Inc., New York.

Katz, J. J., 1986. *The Chemistry of the Actinide Elements, Second Edition, Volume 1*, eds. J. J. Katz, G. T. Seaborg, and L. R. Morss, Chapman and Hall Ltd., New York.

Kohring, M. W., August 7, 1986. *Gamma Flux Measurements on Spent High Flux Isotope Reactor (HFIR) Fuel Assemblies*, ORNL/CF-86/256, Oak Ridge National Laboratory, Oak Ridge, Tennessee.

Kohring, M. W., September 4, 1987. Correspondence to R.E. Jones, "Spent HFIR Fuel Assembly Dose Rates," Oak Ridge National Laboratory, Oak Ridge, Tennessee.

Kraus, C. A., July 29, 1944. "A Note on the Preparation of a Superoxide of U from $(NH_4)_2\ U_2O_7$," U.S. Manhattan Engineer District, Oak Ridge, Tennessee (unpublished).

Lamarsh, J. R., 1966. *Introduction to Nuclear Reactor Theory*, Addison-Wesley Publishing Company, Reading, Massachusetts.

Lane, J. A., H. G. MacPherson, and F. Maslan, 1958. *Fluid Fuel Reactors*, Addison-Wesley Publishing Company, Inc., Reading, Massachusetts.

Livingston, R. R., August 1999. *Gas Generation Test Support for Transportation and Storage of Plutonium Residue Materials, Part 1: Rocky Flats Sand, Slag, and Crucible Residues*, WSRC-TR-99-00223, Rev. 0, Westinghouse Savannah River Co., Savannah River Site, Aiken, South Carolina.

Lustman, B., 1961. "Irradiation Effects in Uranium Dioxide," pp. 431–666 in *Uranium Dioxide: Properties and Nuclear Applications*, ed. J. Belle, U. S. Atomic Energy Commission, Washington, D.C.

Marshall, J. L., June 11, 1998a. Lockheed Martin Energy Systems, Y-12 Plant, Oak Ridge, Tennessee, personal communication regarding mass spectrometer analysis results for sample S-1 to A. S. Icenhour, Lockheed Martin Energy Research Corp., Oak Ridge National Laboratory, Oak Ridge, Tennessee.

Marshall, J. L., October 8, 1998b. Lockheed Martin Energy Systems, Y-12 Plant, Oak Ridge, Tennessee, personal communication regarding mass spectrometer analysis results for samples S-3, S-4, and S-8 to A. S. Icenhour, Lockheed Martin Energy Research Corp., Oak Ridge National Laboratory, Oak Ridge, Tennessee.

Marshall, J. L., April 28, 1999a. Lockheed Martin Energy Systems, Y-12 Plant, Oak Ridge, Tennessee, personal communication regarding mass spectrometer analysis results for samples S-12 and S-13 to A. S. Icenhour, Lockheed Martin Energy Research Corp., Oak Ridge National Laboratory, Oak Ridge, Tennessee.

Marshall, J. L., August 23, 1999b. Lockheed Martin Energy Systems, Y-12 Plant, Oak Ridge, Tennessee, personal communication regarding mass spectrometer analysis results for samples S-16 and S-17 to A. S. Icenhour, Lockheed Martin Energy Research Corp., Oak Ridge National Laboratory, Oak Ridge, Tennessee.

Marshall, J. L., September 9, 1999c. Lockheed Martin Energy Systems, Y-12 Plant, Oak Ridge, Tennessee, personal communication regarding mass spectrometer analysis results for sample HFIR-1 to A. S. Icenhour, Lockheed Martin Energy Research Corp., Oak Ridge National Laboratory, Oak Ridge, Tennessee.

Marshall, J. L., November 10, 1999d. Lockheed Martin Energy Systems, Y-12 Plant, Oak Ridge, Tennessee, personal communication regarding mass spectrometer analysis results for sample HFIR-2 to A. S. Icenhour, Lockheed Martin Energy Research Corp., Oak Ridge National Laboratory, Oak Ridge, Tennessee.

Marshall, J. L., December 15, 1999e. Lockheed Martin Energy Systems, Y-12 Plant, Oak Ridge, Tennessee, personal communication regarding mass spectrometer analysis results for samples S-20, S-21, and S-22 to A. S. Icenhour, Lockheed Martin Energy Research Corp., Oak Ridge National Laboratory, Oak Ridge, Tennessee.

Mason. R., et al., 1999. *Materials Identification and Surveillance: June 1999 Characterization Status Report*, LA-UR-99-3053, Los Alamos National Laboratory, Los Alamos, New Mexico.

Matzke, Hj., 1982. "Radiation Damage in Crystalline Insulators, Oxides and Ceramic Nuclear Fuels," *Radiat. Eff.* **64**, 3–33.

McEachern, R. J., and P. Taylor, 1998. "A Review of the Oxidation of Uranium Dioxide at Temperatures below 400°C," *J. Nucl. Mater.* **254**, 87–121.

Myers, W. L., 1990. *A Literature Review on the Chemical and Physical Properties of Uranyl Fluoride (UO_2F_2)*, LA-11896-MS, Los Alamos National Laboratory, Los Alamos, New Mexico.

Nakae, N., A. Harada, and T. Kirihara, 1978. "Irradiation Induced Lattice Defects in UO_2," *Nucl. Mater.* **71**, 314–319.

National Research Council, 1997. *Evaluation of the U.S. Department of Energy's Alternatives for the Removal and Disposition of Molten Salt Reactor Experiment Fluoride Salts*, National Academy of Sciences, National Academy Press, Washington, D.C.

Nelson, C. M., R. L. Sproull, and R. S. Caswell, 1953. "Conductivity Changes in KCl Produced by γ and n Irradiation," *Phys. Rev.* **90**, 364.

Nelson, C. M., and J. H. Crawford, Jr., 1958. "Optical and Spin Resonance Absorption in Irradiated Quartz and Fused Silica. I. Optical Absorption," *Bull. Am. Phys. Soc. (II)*, **3**, 136.

Nyquist, R. A., and R. O. Kagel, 1997. *The Handbook of Infrared and Raman Spectra of Inorganic Compounds and Organic Salts, Volume 4, Infrared Spectra of Inorganic Compounds*, Academic Press, Inc., New York.

Pabst, A., 1952. "The Metamict State," *The American Mineralogist, Journal of the Mineralogical Society of America* **37**, 137–157.

Pease, R. S., 1954. "X-ray Examination of Irradiation Effects in Boron Compounds," *Acta Cryst.* **7**, 663.

Pearson, W. B., 1958. *Structure Reports for 1958, Volume 22*, International Union of Crystallography, Netherlands.

Pike Technologies 1999. *Comprehensive Catalog of FTIR Accessories and Supplies*, Madison, Wisconsin.

Primak, W., and L. H. Fuchs, 1955. "Nitrogen Fixation in a Nuclear Reactor," *Nucleonics* **13**(2), 38–41.

Rosenwasser, H., R. W. Dreyfus, and P. W. Levy, 1956. "Radiation-Induced Coloring of Sodium Azide," *J. Chem. Phys.* **24**(2), 184–190.

Saraceno, A. J., April 15, 1988. *Fluorine Overpressurization in the Five-Inch Cylinders*, POEF-T-3474, Martin Marietta Energy Systems, Inc., Portsmouth Gaseous Diffusion Plant, Piketon, Ohio.

Savage, H. C., E. L. Compere, and J. M. Baker, January 31, 1964. pp. 16–37 in "Gamma Irradiation of a Simulated MSRE Fuel Salt in the Solid Phase," *Reactor Chemistry Division Annual Progress Report*, ORNL-3591, Union Carbide Corp.–Nuclear Division, Oak Ridge National Laboratory, Oak Ridge, Tennessee.

Shepherd, December 9, 1977. Manufacturer's data on exposure rate profile in ORNL ^{60}Co source, J. L. Shepherd and Associates, Glendale, California.

Shimanouchi, T., 1972. *Tables of Molecular Vibrational Frequencies, Consolidated Volume I*, NSRDS-NBS 39, U.S. Department of Commerce, National Bureau of Standards, Washington, D.C.

Sibilia, J. P., 1988. *A Guide to Materials Characterization and Chemical Analysis*, VCH Publishers Inc., New York.

Stevens, D. K., W. J. Sturm, and R. H. Silsbee, 1958. "Magnetic Susceptibility of Neutron-Irradiated Quartz," *J. Appl. Phys.* **29**(1), 66–68.

Storm, E., and H. I. Israel, 1970. *Nuclear Data Tables*, **A7**, 565.

Sugier, H., and A. Duda, 1976. "The Gamma-Radiolysis of Polycrystalline Zinc Oxide," *Radiochem. Radioanal. Lett.* **27**(5–6), 359–366.

Sunder, S. D. W. Shoesmith, H. Christensen, M. G. Bailey, and N. H. Miller, 1989. "Electrochemical and X-Ray Photoelectron Spectroscopic Studies of UO_2 Fuel Oxidation by Specific Radicals Formed during Radiolysis of Groundwater," *Mater. Res. Soc. Symp. Proc.* **127**, 317–324.

Sunder, S., D. W. Shoesmith, H. Christensen, N. H. Miller, and M. G. Bailey, 1990. "Oxidation of UO_2 Fuel by Radicals Formed During Radiolysis of Water," *Mater. Res. Soc. Symp. Proc.* **176**, 457–464.

Sunder, S. and N. H. Miller, 1996. "Oxidation of CANDU Uranium Oxide Fuel by Air in Gamma Radiation at 150°C," *J. Nucl. Mater.* **231**, 121–131.

Taylor, J. C., 1976. "Systematic Features in the Structural Chemistry of the Uranium Halides, Oxyhalides and Related Transition Metal and Lanthanide Halides," *Coordination Chem. Rev.* **20**, 197–273.

Taylor, P., D. D. Wood, A. M. Duclos, and D. G. Owen, 1989. "Formation of Uranium Trioxide Hydrates on UO_2 Fuel in Air-Steam Mixtures Near 200°C," *J. Nucl. Mater.* **168**, 70–75.

Thibaut, E., J. Boutique, J. J. Verbist, J. Levet, and H. Noël, 1982. "Electronic Structure of Uranium Halides and Oxyhalides in the Solid State. An X-ray Photoelectron Spectral Study of Bonding Ionicity," *J. Am. Chem. Soc.* **104**, 5266-5273.

Thompson, K. A., July 29, 1998a. Lockheed Martin Energy Systems, Y-12 Plant, Oak Ridge, Tennessee, personal communication regarding XPS analysis results for S-1 and S-2 to A. S. Icenhour, Lockheed Martin Energy Research Corp., Oak Ridge National Laboratory, Oak Ridge, Tennessee.

Thompson, K. A., October, 30, 1998b. Lockheed Martin Energy Systems, Y-12 Plant, Oak Ridge, Tennessee, personal communication regarding XPS analysis results for S-3 and S-4 to A. S. Icenhour, Lockheed Martin Energy Research Corp., Oak Ridge National Laboratory, Oak Ridge, Tennessee.

Thompson, K. A., May 7, 1999. Lockheed Martin Energy Systems, Y-12 Plant, Oak Ridge, Tennessee, personal communication regarding XPS analysis results for S-12 and S-13 to A. S. Icenhour, Lockheed Martin Energy Research Corp., Oak Ridge National Laboratory, Oak Ridge, Tennessee.

Toth, L. M., and L. K. Felker, 1990. "Fluorine Generation by Gamma Radiolysis of a Fluoride Salt Mixture," *Radiat. Eff. Def. Solids* **112**, 201–210.

Toth, L. M., 1990. Unpublished data.

Turner, J. E., 1986. *Atoms, Radiation, and Radiation Protection*, Pergamon Press, New York.

U.S. Department of Energy, February 1993. "Safety Notice," Office of Nuclear Safety, DOE/NS-0013, Washington, D.C.

Vaughan, W. H., W. J. Leivo, and R. Smoluchowski, 1953. "Mechanical Properties of Proton Irradiated Alkali Halides," *Phys. Rev.* **91**, 245.

Wasywich, K. M., W. H. Hocking, D. W. Shoesmith, and P. Taylor, 1993. "Differences in Oxidation Behavior of Used CANDU Fuel During Prolonged Storage in Moisture-Saturated Air and Dry Air at 150°C," *Nucl. Technol.* **104**, 309–329.

Weber, W. J., et al., June 1998. "Radiation Effects in Crystalline Ceramics for the Immobilization of High-level Nuclear Waste and Plutonium," *J. Mater. Res.* **13**(6), 1434–1484.

Wertz, J. E., P. Auzins, R. A. Weeks, and R. H. Silsbee, 1957. "Electron Spin Resonance of *F* Centers in Magnesium Oxide; Confirmation of the Spin of Magnesium-25," *Phys. Rev.* **107**(6), 1535–1537.

Westervelt, D. R., 1953. "Thermal Annealing of Radiation-Induced Hardness Changes in Alkali Halides," *Acta Met.* **1**, 755–758.

Williams, D. F., G. D. Del Cul, and L. M. Toth, January 1996. *A Descriptive Model of the Molten Salt Reactor Experiment After Shutdown: Review of FY 1995 Progress*, ORNL/TM-13142, Oak Ridge National Laboratory, Oak Ridge, Tennessee.

Williams, D. F., 1999. "Radiolysis Studies in Support of the Remediation of the Molten Salt Reactor Experiment," *Transactions of the American Nuclear Society*, **81**, 89–90.

Wilson, J. B., November 25, 1997. Lockheed Martin Energy Systems, Y-12 Plant, Oak Ridge, Tennessee, personal communication regarding mass spectroscopic analysis results to A. S. Icenhour, Lockheed Martin Energy Research Corp., Oak Ridge National Laboratory, Oak Ridge, Tennessee.

Wyckoff, R. W. G., 1964. *Crystal Structures, Second Edition, Volume 2, Inorganic Compounds* RX_n, R_nMX_2, R_nMX_3, Interscience Publishers, New York.

Wysocki, S., 1986. "Gamma-Radiolysis of Polycrystalline Magnesium Oxide," *J. Chem. Soc., Faraday Trans. 1*, **82**, 715–721.

Zachariasen, W. H., 1948. "Crystal Chemical Studies of the 5f-Series of Elements. III. A Study of the Disorder in the Crystal Structure of Anhydrous Uranyl Fluoride," *Acta Cryst.* **1**, 277–281.

APPENDIXES

Appendix A

DESCRIPTION OF THE MSRE PROJECT

Appendix A: DESCRIPTION OF THE MSRE PROJECT

The MSRE was operated at ORNL from 1965 to 1969 to test the concept of a high-temperature, homogeneous, fluid–fueled reactor. An overview of the MSRE system is shown in Fig. A.1. The reactor was fueled with a molten salt mixture of $LiF-BeF_2-ZrF_4-UF_4$ (with a composition of 64.5-30.4-4.9-0.14 mol % for a ^{233}U-fueled reactor and 64.1-30.0-5.0-0.81 mol % for a ^{235}U-fueled reactor), which melts at about 450°C and which served as both the fuel and the primary coolant (Compere et al. 1975). This fluid was circulated by a large impeller pump between the reactor core and the primary heat exchanger. A secondary coolant of $LiF-BeF_2$ (66–34 mol %), circulated by a similar impeller pump, transferred heat from the primary heat exchanger to an air-cooled radiator. About 4,350 kg (~2 m^3) of fuel salt constituted the fuel charge circulating in the fuel salt circuit. Originally, the MSRE was fueled with $^{235}UF_4$; however, after successful operation with this isotope, the ^{235}U was removed by fluorination of the tetrafluoride to the volatile hexafluoride, UF_6. Afterward, the fuel was reconstituted with $^{233}UF_4$ (containing 220 ppm ^{232}U, an impurity isotope) to demonstrate that the system could function equally well on the product of a ^{232}Th thermal breeding cycle. After the successful completion of this campaign, reactor operation was terminated December 12, 1969, when the fuel salt was drained from the reactor circuit and solidified in two drain tanks at a lower level of the facility. The fuel salt has remained in these tanks for the past 30 years.

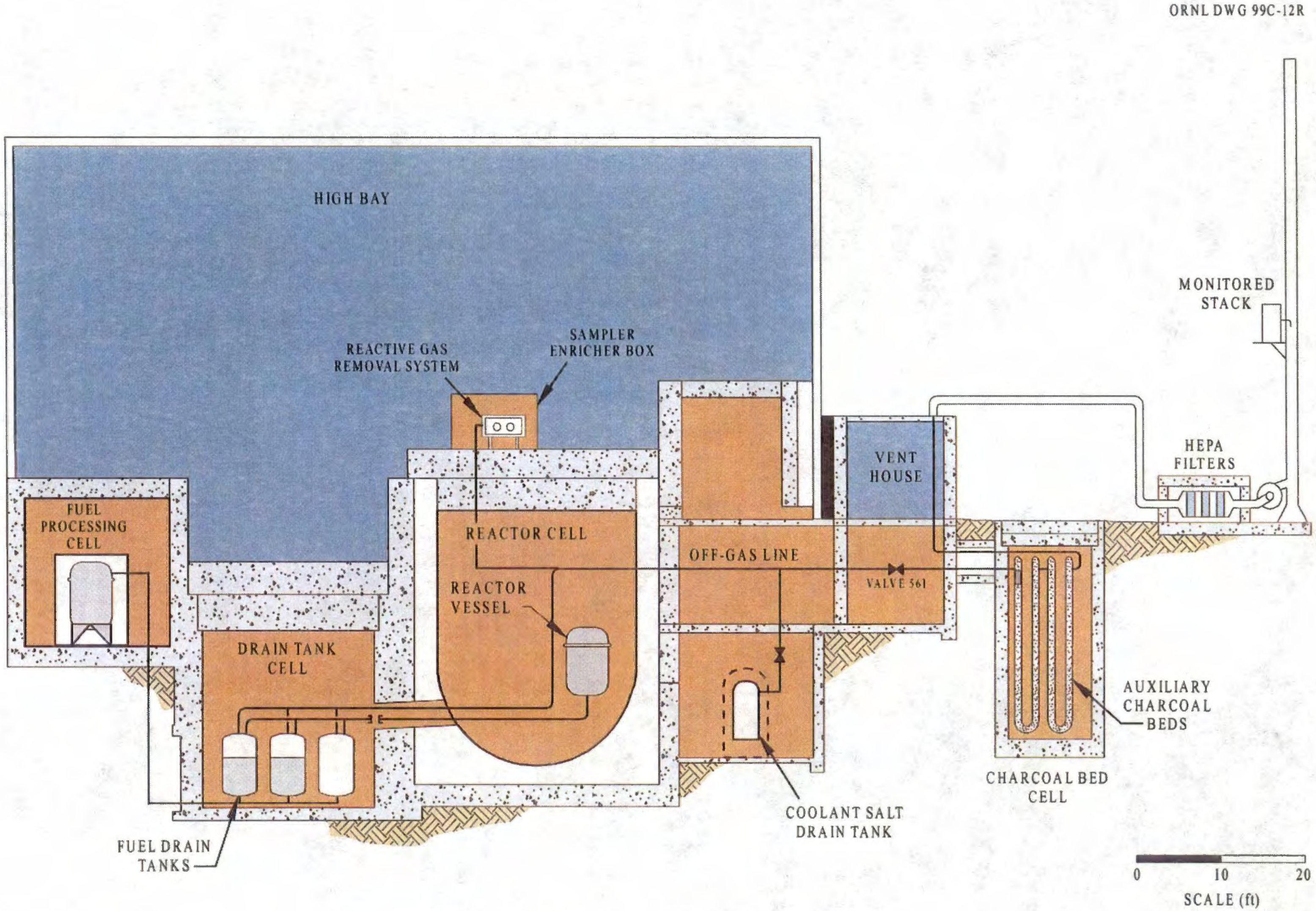

Fig. A.1. Overview of the MSRE system.

During the MSRE operation, no radiolysis of the fuel salt was ever observed. However, radiolysis of the fuel salt was recognized as a problem if the salt were solidified and held below 100°C, with the net effect that F_2 would be liberated from the frozen salt mixture and cause corrosion or overpressurization of the drain-tank containment system. The relevant radiolysis reactions are (Williams, Del Cul, and Toth 1996; Toth and Felker 1990):

$$\mathrm{LiF} + h\nu \rightarrow \mathrm{Li} + \mathrm{F} \tag{A.1}$$

and

$$\mathrm{BeF_2} + h\nu \rightarrow \mathrm{Be} + 2\mathrm{F}. \tag{A.2}$$

To prevent the accumulation of F_2, the frozen salt (which was normally at about 40°C because of the self-heating by fission product decay) was heated to 200°C annually. This frequency was selected because of the experimentally observed induction period before release of F_2 from the salt matrix (Savage, Compere, and Baker 1964). Hence, it was believed that any generated F_2 would be trapped in the matrix and that heating would lead to the recombination of the F_2 with the reduced metal sites left in the salt. The fluorine pressure in the drain tanks before and after annealing was not monitored; therefore, the effectiveness of this annual procedure was never established.

In the late 1980s, an increase in radioactivity in one of the gas-line protrusions into the North Electrical Services Area, a room adjacent to the drain-tank cell, was suspected as coming from UF_6. Because the annual annealing operation would drive this condensable gas from the drain tanks to cooler surfaces, such as the gas-line protrusion into the North Electrical Services Area, the annual annealing operation was postponed until a better understanding of the fuel-salt under long-term storage conditions was obtained.

In early 1994, two 1,000-mL gas samples were withdrawn (from a gas line in the Vent House connected to the drain tanks) and analyzed. Surprisingly, 350 Torr of F_2, 70 Torr of UF_6, and smaller amounts of other gases were found in both of the samples, confirming that the annual annealing operations had not been successful in recombining the fluorine with the fuel salt and, more importantly, that the temperature gradient created during the annealing operation had definitely (as was later shown – Williams, Del Cul, and Toth 1996) contributed to the formation and displacement of UF_6 from the fuel salt. The UF_6 was formed by the following reaction (Williams 1999):

$$UF_4 + F_2 \rightarrow UF_6 \tag{A.3}$$

Upon further investigation, it was found that the gas line from the drain tank also ran to large charcoal beds (U-tubes of 6-in. diam and 24-ft length), which could not be isolated because a shutoff valve had failed in the open position. Gamma scans and thermal analyses indicated that about 2.6 kg of the uranium from the drain tanks had been deposited at the charcoal-bed inlet. Because F_2 was also present with the UF_6, it was believed that the charcoal bed containing both carbon-fluorine reaction products (C_xF) and uranium presented both chemical and radiological hazards. The C_xF was an explosive compound that could result in major dispersion of the ^{233}U contained in the charcoal bed. On November 20, 1995, the shutoff valve was closed to prevent the further movement of uranium and fluorine onto the charcoal bed. Steps were taken to minimize (and ultimately eliminate) the possibility of explosive decomposition of the C_xF in the charcoal beds.

The ongoing remediation activities at the MSRE include the removal of the UF_6 from the off-gas system, the removal of the uranium-laden charcoal from the charcoal bed, and the removal of the ^{233}U remaining in the fuel and flush salts. The UF_6 from the off-gas system has been chemisorbed onto sodium fluoride (NaF) traps, forming a complex ($2NaF \bullet UF_6$), which can be revolatilized at higher temperatures. The uranium-laden charcoal has been pretreated with ammonia to prevent deflagration of C_xF compounds, which could occur if there were localized heating during the charcoal removal process. The uranium-laden portion of the charcoal bed will be removed into storage containers that can be used for further processing. The fuel salt in the drain tanks will be melted, and the ^{233}U will be removed by fluorination to UF_6. Similar to the approach taken for the off-gas system, the UF_6 ultimately will be trapped on NaF pellets. Because the products of these remediation actions (i.e., $2NaF \bullet UF_6$ and a uranium fluoride or oxyfluoride on charcoal) are not suitable for long-term storage, these materials must be converted to a more stable form (i.e., U_3O_8). Residual fluoride compounds (e.g., UO_2F_2) may be present (at some small concentration) in the converted uranium oxide. Based on the experience with radiolysis in the MSRE, it is then important to understand the radiolytic behavior of these residual compounds for the purposes of long-term storage of the uranium oxides.

Appendix B

DESCRIPTION OF THE CONVERSION PROCESS

Appendix B: DESCRIPTION OF THE CONVERSION PROCESS

A process, which is being developed at ORNL, will be used to remove the uranium from either the NaF traps or the charcoal as UF_6. The UF_6 is then converted to U_3O_8 (Del Cul, Icenhour, and Toth 1997). Because there is a large radiation field caused by the ^{232}U (an impurity isotope in the ^{233}U), the material must be remotely processed in a hot cell. The major design considerations for this process were:

- minimization of uranium losses
- minimization of secondary wastes and contamination
- simplicity and adaptability to small-scale hot-cell operation
- no moving parts for stirring, mixing, or transfers between vessels
- ability to meet minimal product purity requirements
- adaptability to a variety of feed materials (e.g., $2NaF \cdot UF_6$ complex, uranium-laden charcoal, and miscellaneous materials such as uranium deposits in metal pipes)

Laboratory tests of the process at one-fifth scale were successfully completed. Follow-on testing at full scale was completed using a prototype system, which was also used to develop operational procedures and to train personnel. A brief description of the conversion process is presented in the following paragraphs.

To remove the uranium from a NaF trap, the trap is heated to about 400°C, and the UF_6 is desorbed from the NaF pellets in a subatmospheric, closed-loop system (Fig. B.1) and condensed in a liquid-nitrogen-cooled vessel (i.e., the conversion vessel). A small volume of fluorine gas is continuously recirculated to act as (1) a carrier gas and (2) a fluorination agent to react with any oxyfluorides or lower fluorides that could be present in the NaF trap. Fourier Transform Infrared (FTIR) spectrometers that have in-line gas cells, located before and after the UF_6 conversion vessel, are used to monitor the uranium recovery. The recovery is complete when UF_6 is no longer detected by the FTIR.

The uranium-laden charcoal process is still being developed, but a conceptual flowsheet is shown in Fig. B.2. To remove the uranium from the charcoal, the charcoal container is first helium purged and heated to remove the NH_4F produced by the treatment of the C_xF with ammonia. Once the charcoal reaches approximately 600°C, the helium purge is replaced with F_2 to produce volatile C-F products. Above 500°C, charcoal completely burns with the F_2, producing UF_6, CF_4, and a small fraction of C_2F_6 and higher fluorocarbons. All the carbon is totally oxidized at this temperature; thus no fluorinated charcoal (i.e., C_xF) is formed. The UF_6 that is produced by the burning will be trapped on NaF pellets. The progress of the reaction can be monitored by FTIR gas analysis. As an alternative, the charcoal can be initially burned in oxygen, producing CO_2 and nonvolatile uranium oxide residue. The residue would then be fluorinated to remove the ^{233}U as UF_6 onto NaF pellets. Either process (i.e., F_2 or O_2 burning of the charcoal) results in the trapping of UF_6 on a NaF trap. The UF_6 can then be removed

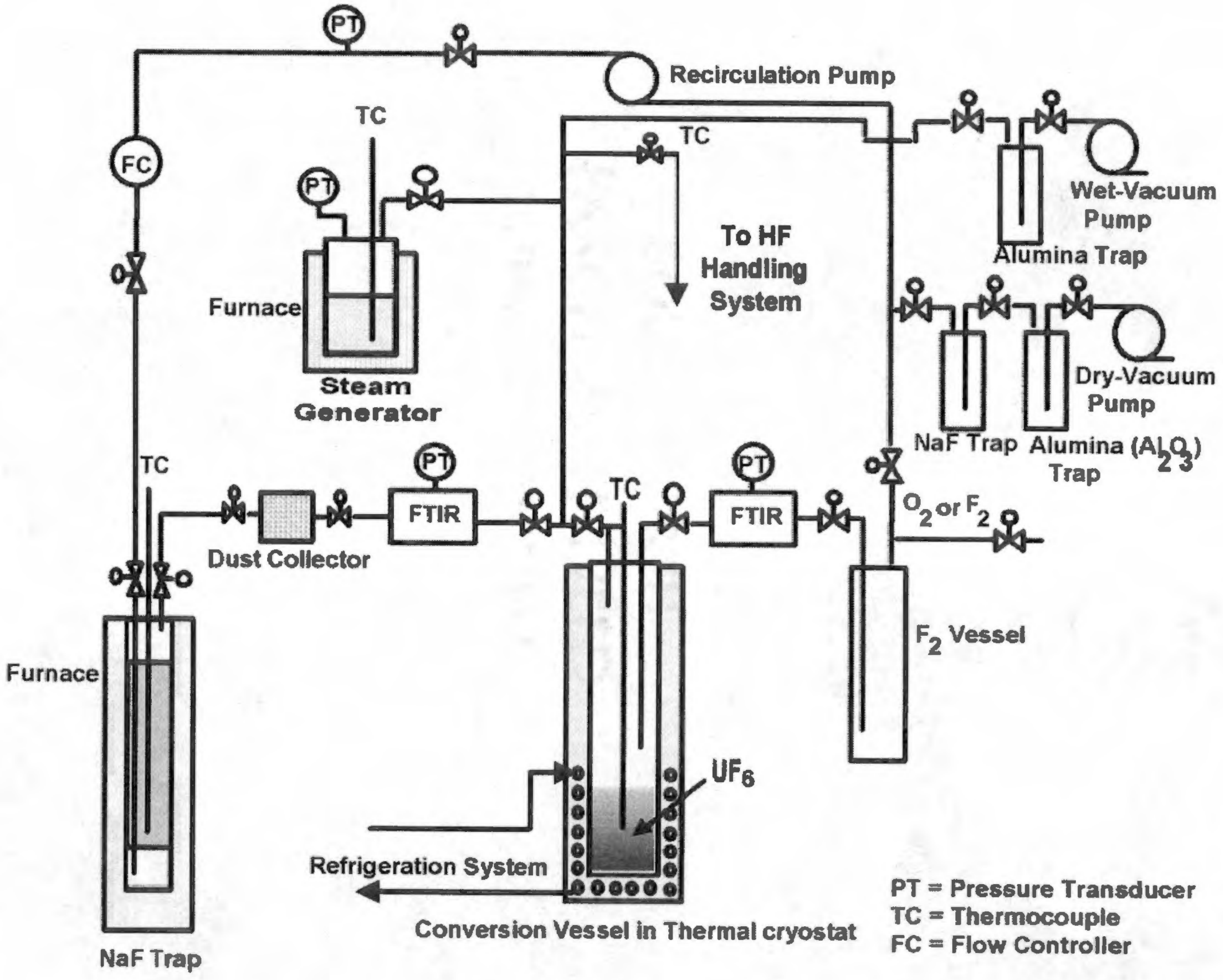

Fig. B.1. Diagram of uranium recovery and conversion process for NaF traps.

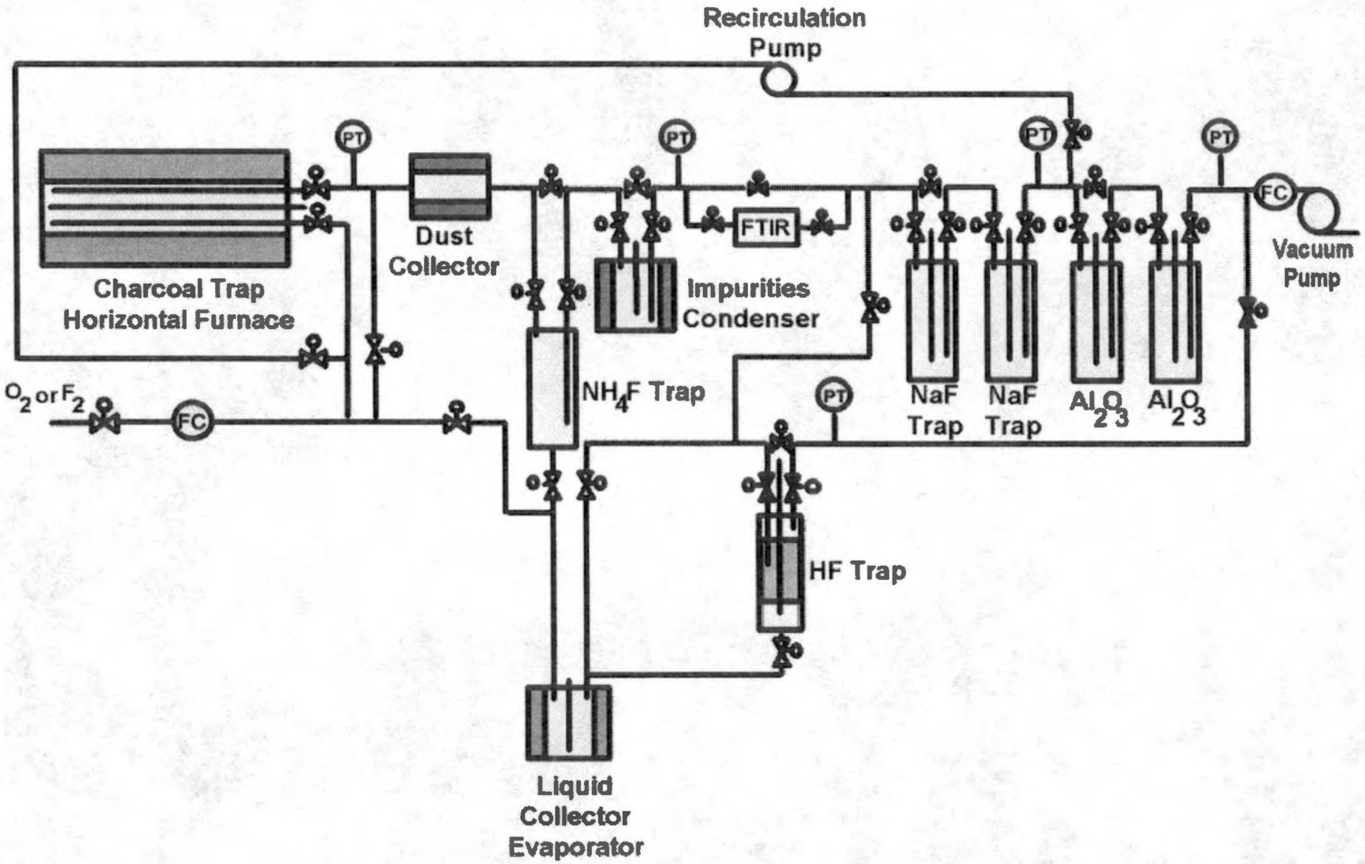

Fig. B.2. Uranium-laden charcoal recovery and trapping system.

from the trap and condensed as a frozen solid in a conversion vessel, as previously described.

The conversion of the frozen UF_6 into U_3O_8 (Fig. B.3) is conducted in the same vessel as that used to condense the UF_6, which is removed from the NaF trap (i.e., the conversion vessel). Initially, a slight excess of water vapor is condensed as ice on the top of the frozen UF_6. The vessel is allowed to warm, resulting in the formation of $UO_2F_2 \bullet xH_2O$ and HF. The resulting solid cake of material is then heated in 50°C steps and sequentially contacted with pressurized steam. The pressurized steam gradually reacts with the oxyfluoride-oxide mixture and forms HF and some U_3O_8. The HF and steam then are transported to and absorbed by a solid HF-trapping material (neutralizing the HF) at the completion of each step. When the temperature reaches 800°C, air is introduced, and the vessel is heated to about 950°C to complete the reaction to produce U_3O_8. At the end of the process, the conversion vessel is cooled to ambient temperature, lines are evacuated and filled with an inert gas, and the vessel is then disconnected, capped, overpacked, and removed from the hot cell and placed in storage.

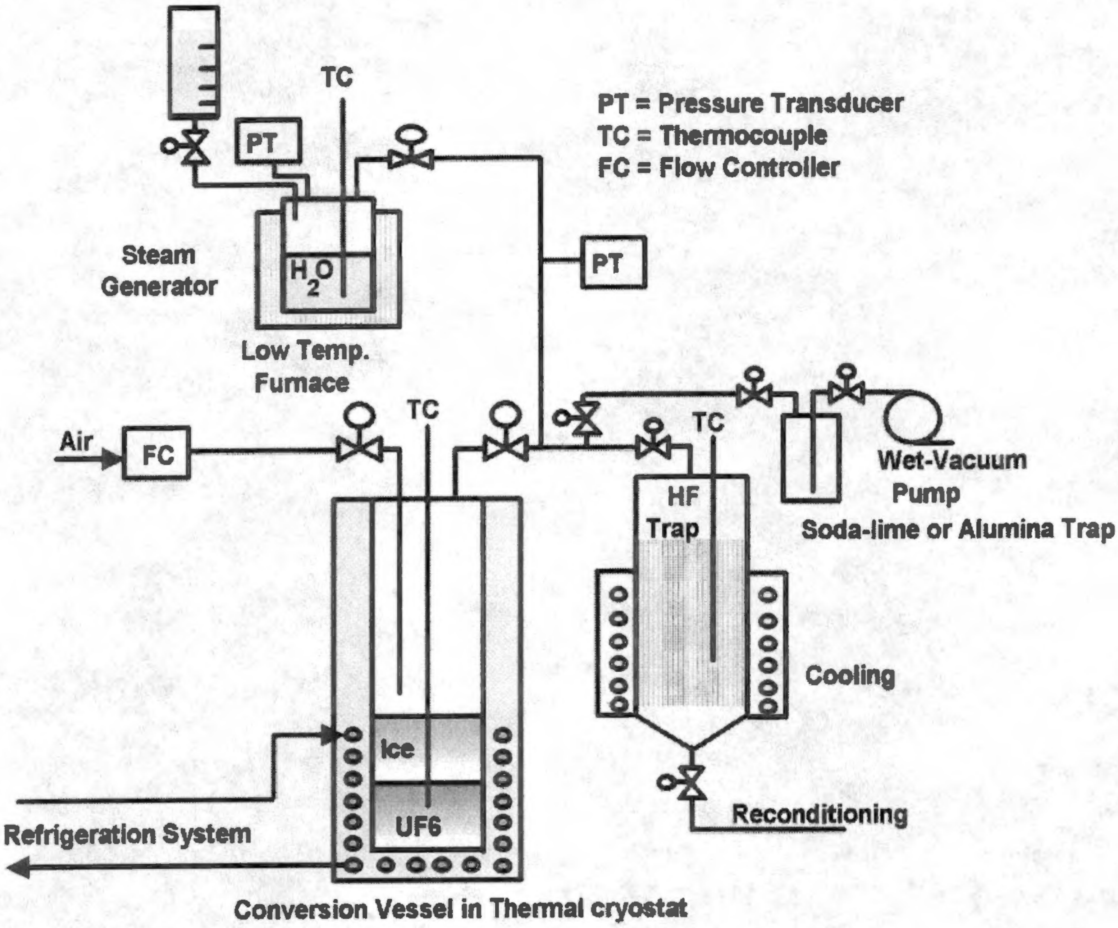

Fig. B.3. Steam hydrolysis system.

Appendix C

ESTIMATION OF ABSORBED DOSE FROM EXPOSURE

Appendix C: ESTIMATION OF ABSORBED DOSE FROM EXPOSURE

The exposure rate is reported for both the ^{60}Co source and the HFIR SNF elements that were used in the irradiation experiments. *Exposure* is a measure of the amount of charge produced in air per unit mass of air. However, in the case of radiolytic experiments, the quantity of interest is the absorbed dose, which is the energy absorbed by a material per unit mass. To compute the *absorbed dose*, the method presented in ASTM E66-91 is used (ASTM E666-91 1991). The following formula is used to convert exposure rate to dose rate:

$$\dot{D}_y = 8.69 \times 10^{-3} \frac{\left(\frac{\mu_{en}}{\rho}\right)_y}{\left(\frac{\mu_{en}}{\rho}\right)_{air}} \dot{X} \exp\left[-\left(\frac{\mu_{en}}{\rho}\right)_y x\right], \tag{C.1}$$

where

$\dot{D}_y$ = dose rate in material y at depth x (Gy/h),

$\frac{\mu_{en}}{\rho}$ = mass energy absorption coefficient (m^2/kg), and

$\dot{X}$ = exposure rate (R/h).

The value 8.69×10^{-3} converts roentgens to Gy in air.

For small samples, the sample thickness is neglected, and the equation reduces to

$$\dot{D}_y = 8.69 \times 10^{-3} \frac{\left(\frac{\mu_{en}}{\rho}\right)_y}{\left(\frac{\mu_{en}}{\rho}\right)_{air}} \dot{X} \; . \tag{C.2}$$

For samples that consist of mixtures of elements, the mass energy absorption coefficient is calculated by (Hubbell 1982)

$$\frac{\mu_{en}}{\rho} = \sum_i w_i \left(\frac{\mu_{en}}{\rho}\right)_i , \tag{C.3}$$

where

w_i = the proportion by weight of the ith element (dimensionless), and

$\left(\frac{\mu_{en}}{\rho}\right)_i$ = mass energy absorption coefficient for the ith element (m^2/kg).

Selected values of $\frac{\mu_{en}}{\rho}$ for several elements and energies are presented in Table C.1. These values were taken from Hubbell (1982).

Table C.1 Selected mass energy absorption coefficients[a]

Energy (MeV)	μ_{en}/ρ (10^{-3} m^2/kg)				
	U	O	F	H_2O	air
0.93	4.978	2.824	2.675	3.137	2.820
1	4.473	2.791	2.643	3.100	2.787
1.25	3.748	2.669	2.528	2.966	2.666
2	2.612	2.346	2.223	2.604	2.342

[a] Hubbell, J. H., 1982. "Photon Mass Attenuation and Energy-absorption Coefficients from 1 keV to 20 MeV," *Int. J. Appl. Radiat. Isot.* **33**, 1269–90.

To account for the slight attenuation of the photon flux by the irradiation containers, the computed dose rate was multiplied by the attenuation factor $e^{-\mu x}$, where μ is the attenuation coefficient (cm^{-1}) and x is the wall thickness of the container. For the ^{60}Co irradiations, the attenuation factors were calculated based on the average energy of the two emitted gammas (i.e., 1.25 MeV), while for the HFIR SNF irradiations, the attenuation factor was based on the average energy of 0.93 MeV. Selected attenuation coefficients are presented in Table C.2. For the ^{60}Co source, the dose rate, as a function of time after insertion of the sample into the source, is

$$\dot{D}(t) = \dot{D}_{\circ}\, e^{-\lambda t}, \tag{C.4}$$

where

$\dot{D}(t)$ = dose rate at time t (Gy/h),

$\dot{D}_\circ$ = initial dose rate (Gy/h),

λ = decay constant = ln2/half-life (year^{-1}), and

t = time since insertion (year).

Table C.2 Selected attenuation coefficients for materials used in irradiation containers

Energy (MeV)	μ (cm^{-1})	
	Ni[a]	Fe[b]
0.93	0.241	0.5004
1	0.238	0.4807
1.25	0.234	0.4362
2	0.220	0.3421

[a] Storm, E., and H. I. Israel, 1970. *Nuclear Data Tables,* **A7**, 565.

[b] Hubbell, J. H., 1982. "Photon Mass Attenuation and Energy-absorption Coefficients from 1 keV to 20 MeV," *Int. J. Appl. Radiat. Isot.*, **33**, 1269–1290.

The integrated dose at time t is given by integration of Eq. (C.4), resulting in

$$D(t) = \frac{\dot{D}_\circ}{\lambda}(1 - e^{-\lambda t}), \tag{C.5}$$

where

$D(t)$ = integrated dose at time t (Gy).

For the HFIR SNF element irradiations, exposure rate data, as a function of time, were provided. These data were fit to curves (e.g., Fig. C.1), which were integrated to determine the total exposure during an irradiation. This exposure was then converted to dose by using Eqs. (C.2) and (C.3). The attenuation of the gamma field by the walls of the sample container was accounted for by multiplying the computed dose by the attenuation factor, $e^{-\mu x}$.

The HFIR SNF element emits a spectrum of gamma-ray energies. Based on Williams, Del Cul, and Toth (1996), the average gamma energy (one day after SNF discharge from the reactor) is 0.93 MeV (see Table 3.2), and attenuation factors (and hence, dose) are calculated based on this energy. Additional calculations were performed using different energies for the gamma rays: 1 and 2 MeV. In each case, the computed G-value for the gas yield was the same; hence, the G-value computation was relatively insensitive to the gamma energy for the HFIR SNF irradiations.

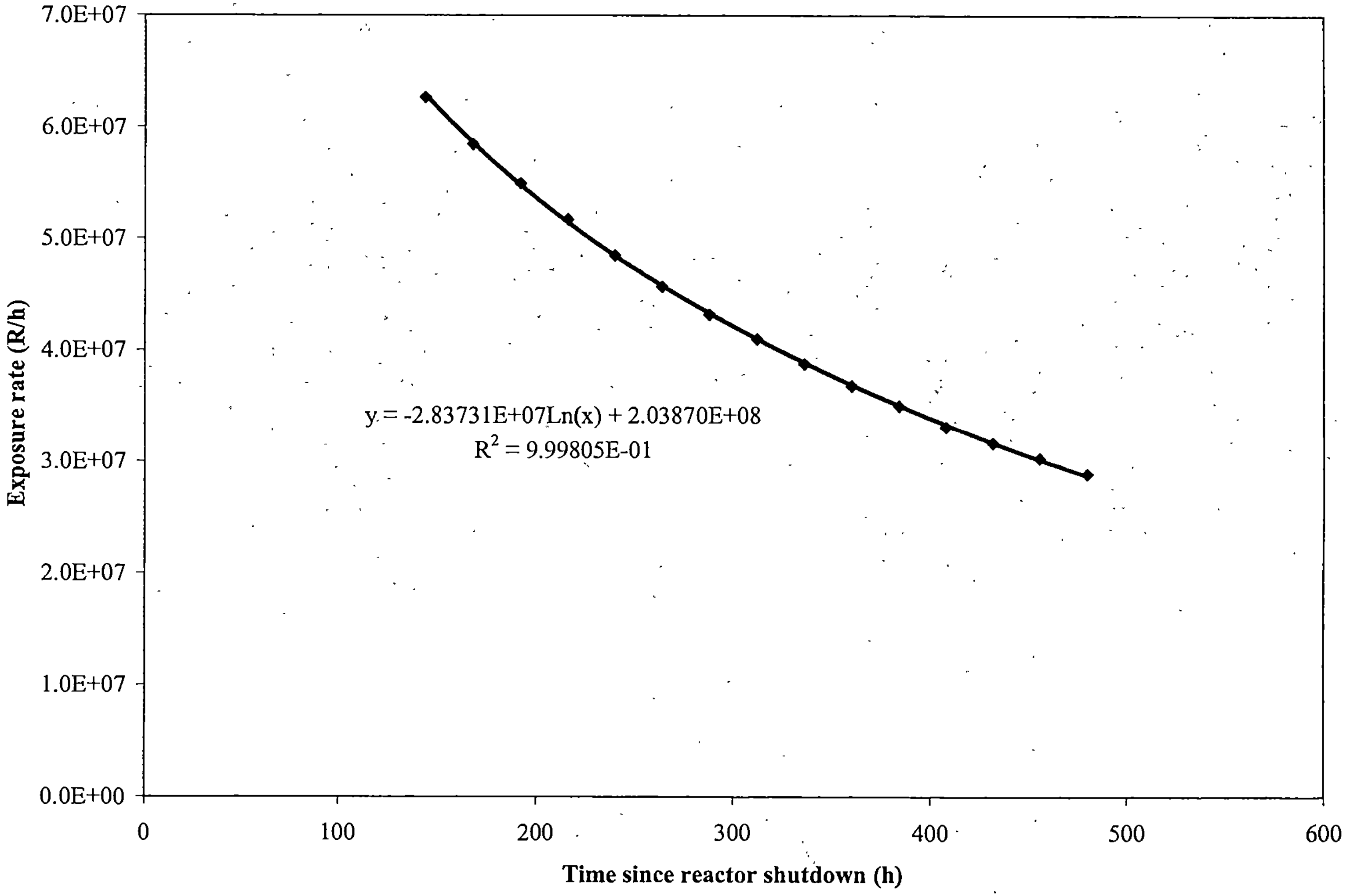

Fig. C.1. Exposure rate curve fit for HFIR SNF element from cycle 371.

Appendix D

INFRARED ANALYSES

Appendix D: INFRARED ANALYSES

Two types of infrared analyses were performed on samples for the radiolysis experiments. After irradiation experiments, gas samples were analyzed by FTIR spectroscopy. Solid samples of $UO_2F_2 \bullet xH_2O$ were analyzed both before and after irradiations by ATR. The principles of these techniques, FTIR spectroscopy and ATR, are described in Sects. 3.3.2.2 and 3.3.3.4, respectively. An analysis performed by either of these techniques results in an infrared absorption spectrum of the material, which can be used to identify the chemical compounds in the material and to provide information on their structure.

In this appendix, the results of selected FTIR and ATR analyses are described. Results of FTIR analyses are given in Sect. D.1, while results of ATR analyses are given in Sect. D.2.

D.1 FTIR ANALYSES

FTIR spectra for gas samples taken from S-3 ($UO_2F_2 \bullet 1.7H_2O$ loaded in air) and S-4 ($UO_2F_2 \bullet 0.4H_2O$ loaded in helium) are shown in Figs. D.1 and D.2, respectively. These spectra demonstrate the features that were typical of those seen in the FTIR analyses.

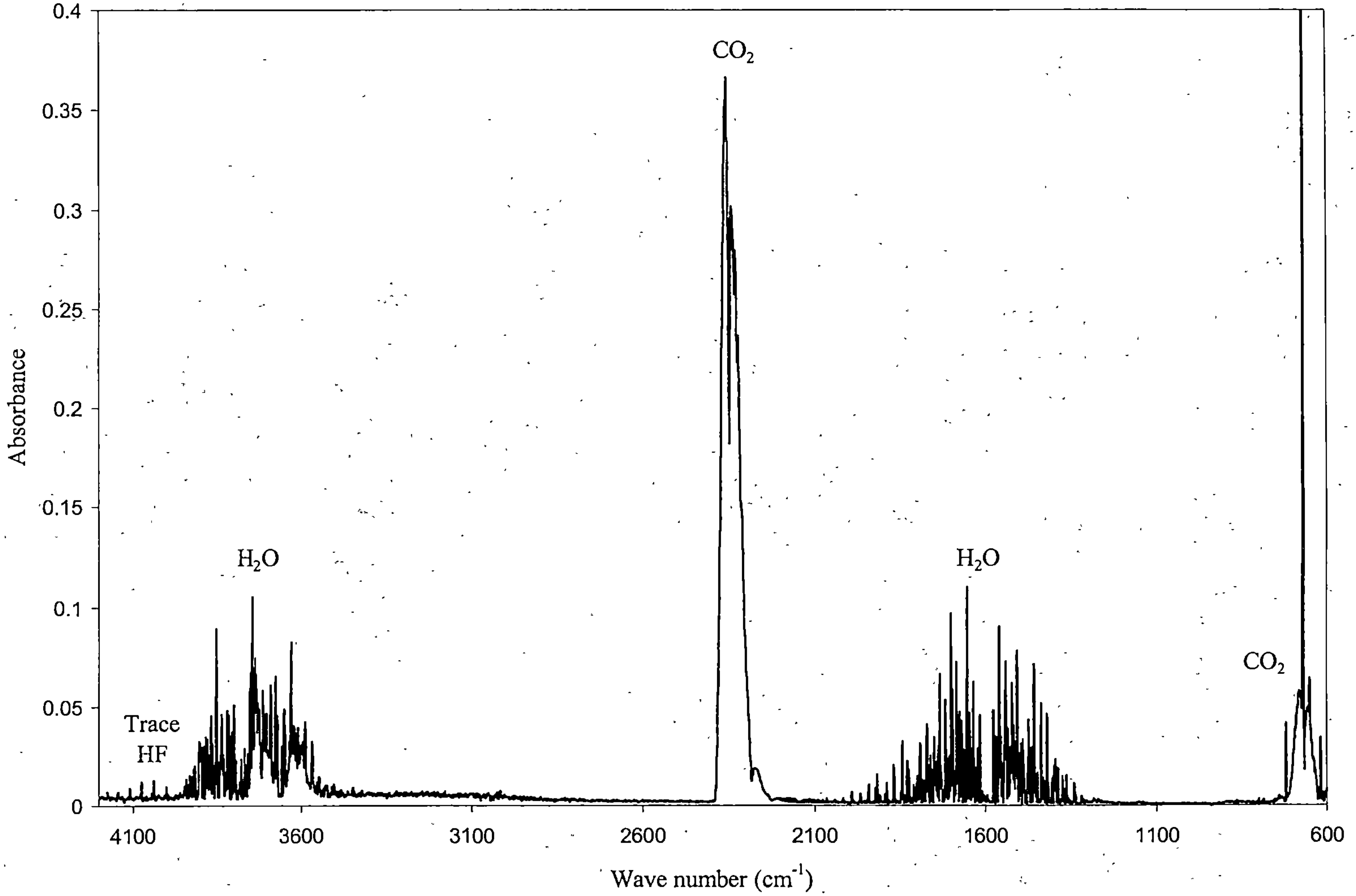

Fig. D.1. FTIR spectrum for a gas sample taken from S-3 (UO_2F_2•$1.7H_2O$ loaded in air).

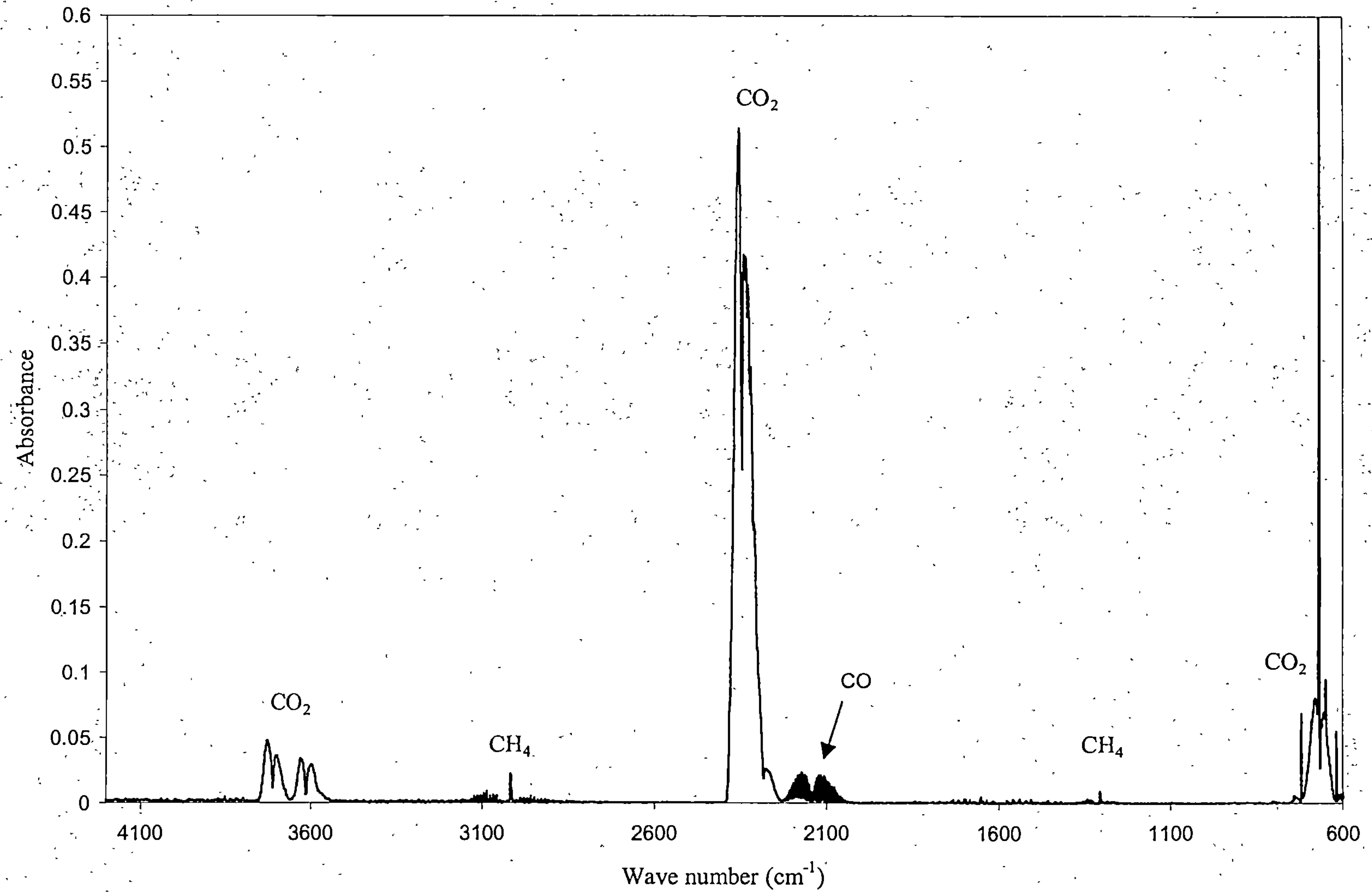

Fig. D.2. FTIR spectrum for a gas sample taken from S-4 ($UO_2F_2 \cdot 0.4H_2O$ loaded in helium).

The spectrum for sample S-3 (Fig. D.1) reveals the presence of H_2O, CO_2, and a trace of HF. The presence of the H_2O is not surprising because the sample was loaded in air. The CO_2 peaks indicate that a large amount of CO_2 was present, as was confirmed by MS analysis. Finally, regarding the trace HF, it was discovered that exposure of the FTIR gas cell to moist air after passivation with F_2 resulted in the production of HF. No HF was seen in the MS analysis for this sample; hence, the trace HF seen in Fig D.1 was not from the $UO_2F_2 \bullet 1.7H_2O$.

The spectrum for sample S-4 (Fig. D.2) shows the presence of CO_2, CO, and a trace of CH_4. (Note that in Fig. D.1, the CO_2 peaks at 3598, 3626, 3703, and 3730 cm^{-1} were obscured by the water peaks.) The small amount of CO was likely the result of reactions between carbon and oxygen radicals produced from radiolysis of the UO_2F_2. The trace CH_4 may have been an impurity in the sampling system.

Selected infrared frequency assignments for CO_2 and H_2O are shown in Table D.1 (Shimanouchi, 1972).

D.2 ATR ANALYSES

The fundamental infrared frequencies of the UO_2^{2+} group of $UO_2F_2 \bullet xH_2O$ are given in Table D.2 (Nyquist and Kagel 1997, Barr and Horton 1952, Armstrong et al., 1991). The asymmetric stretching frequency, ν_3, varies from about 925–1020 cm^{-1}, depending on the amount of hydration of the UO_2F_2. Nyquist and Kagel (1997) reported ν_3 bands at 925, 960, and 1010 cm^{-1} for "$UO_2F_2 \bullet xH_2O$." However, they did not report the value of x, so the amount of hydration is not known. Armstrong et al. (1991) state that ν_3

Table D.1. Assignment of selected infrared frequencies for CO_2 and H_2O[a]

Assignment	Description	Wave number (cm^{-1})
CO_2		
ν_1	Symmetric stretching	inactive
ν_2	Bending	667
ν_3	Asymmetric stretching	2349
H_2O		
ν_1	Symmetric stretching	3657
ν_2	Bending	1595
ν_3	Asymmetric stretching	3756

[a] Shimanouchi, T., 1972. *Tables of Molecular Vibrational Frequencies, Consolidated Volume I*, NSRDS-NBS 39, U.S. Department of Commerce, National Bureau of Standards, Washington, D.C.

Table D.2. Assignment of infrared frequencies for the uranyl (UO_2^{2+}) ion[a]

Assignment	Description	Wave number[a] (cm^{-1})
ν_1	Symmetric stretching	860
ν_2	Bending	210
ν_3	Asymmetric stretching	925–1020

[a] Sources: Nyquist, R. A., and R. O. Kagel, 1997. *The Handbook of Infrared and Raman Spectra of Inorganic Compounds and Organic Salts, Volume 4, Infrared Spectra of Inorganic Compounds*, Academic Press, Inc., New York. Barr, J. T., and Horton, C. A., 1952. "Some New Uranium Complexes," *J. Amer. Chem. Soc.* 74, 4430–4435 (1952). Armstrong D. P., et al., 1991. "An FT-IR Study of the Atmospheric Hydrolysis of Uranium Hexafluoride," *Applied Spectroscopy* 45(6), 1008–1016 (1991).

occurs at 1020 cm^{-1} for anhydrous UO_2F_2. Barr and Horton (1952) analyzed "anhydrous" UO_2F_2, and their spectrum shows ν_3 peaks at about 925, 962, and 1010 cm^{-1}. This spectrum indicates that the sample was actually a mixture of anhydrous and hydrated material. A weak combination band at $\nu_1 + \nu_3$, ranging from 1785–1880 cm^{-1}, is sometimes seen in the UO_2F_2 spectrum.

Armstrong et al. (1991) also described a band at 1620 cm^{-1}, which they attributed to a $UO_2F_2{\bullet}xH_2O{\bullet}y$HF complex. This peak is also seen at 1620 cm^{-1} in the spectrum by Nyquist and Kagel (1997). The spectrum for "anhydrous" UO_2F_2 by Barr and Horton (1958) shows the "complex" peak at about 1613 cm^{-1} —again indicating that this material may have been slightly hydrated.

A typical ATR spectrum for $UO_2F_2{\bullet}0.4H_2O$, which was one of the materials used in the radiolysis experiments, is shown in Fig. D.3. Similar spectra were obtained for the other materials used. This spectrum demonstrates the features typical of the hydrated UO_2F_2. Peaks for the asymmetric vibration, ν_3, are evident at both 1004 and 960 cm^{-1}, indicating that this material has a mixture of both anhydrous and hydrated components. The peak at 870 cm^{-1} is visible as a shoulder. At 1617 cm^{-1}, the band associated with the $UO_2F_2{\bullet}xH_2O{\bullet}y$HF complex is seen. The $\nu_1 + \nu_3$ peak is found at 1872 cm^{-1}. In the range 2600–3700 cm^{-1}, there is a broad band associated with OH stretching vibration. Finally, the two small peaks at 2333 and 2360 cm^{-1} are CO_2, indicating a small amount of CO_2 contamination in the analysis chamber.

Material from the same stock as that used in Fig. D.3 was burned in O_2 at 500–550°C to remove carbon impurities. The results of an ATR analysis of the

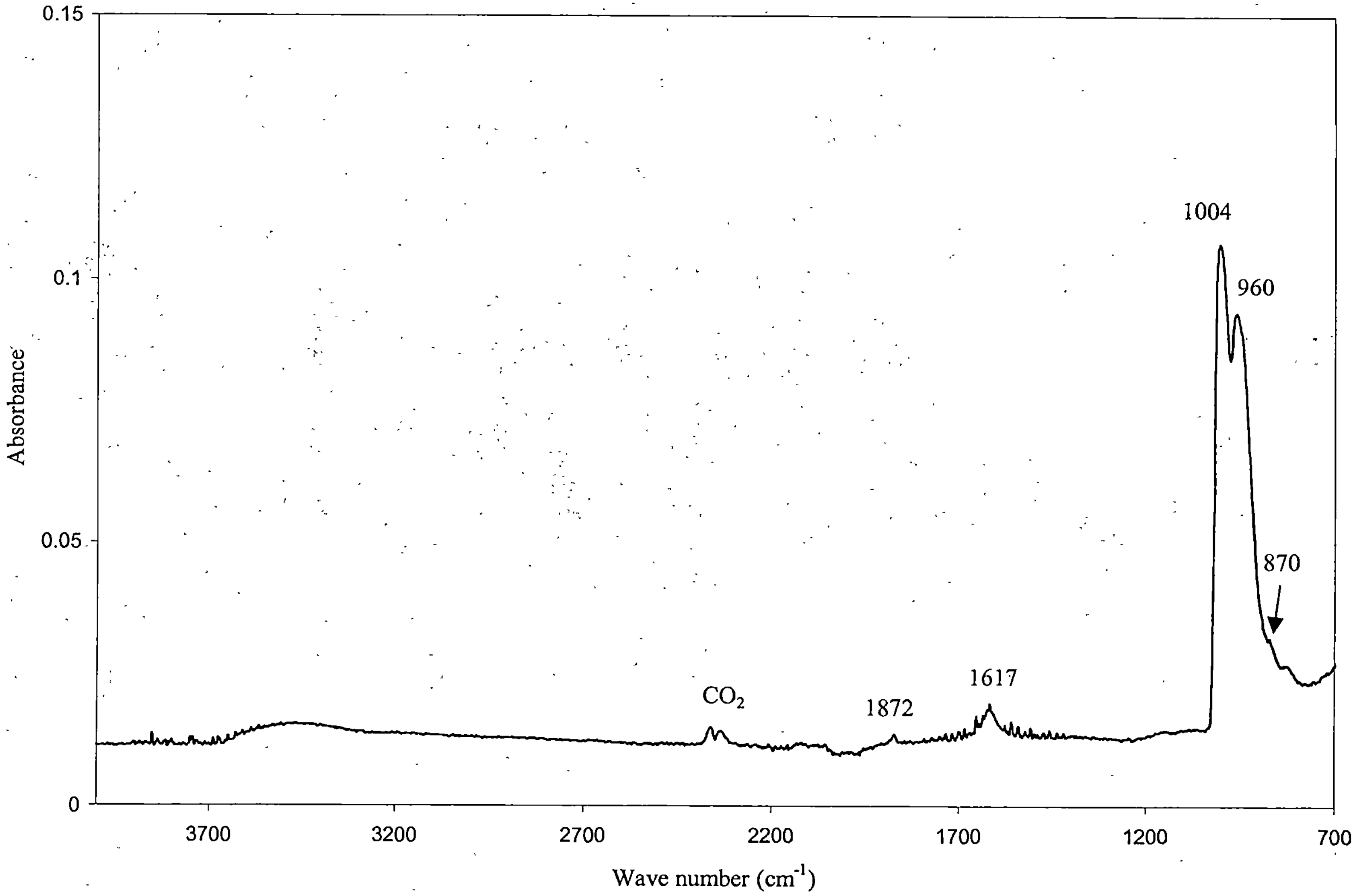

Fig. D.3. ATR spectrum for a sample of $UO_2F_2 \bullet 0.4H_2O$.

O_2-burned UO_2F_2 are shown in Fig. D.4. Interestingly, in comparison with Fig. D.3, the ν_3 peak has shifted toward the anhydrous peak at 1000 cm^{-1}. A peak at 862 cm^{-1} has become more prominent. Additionally, the peak at 1617 cm^{-1} and the OH stretching region have disappeared, indicating a removal of water from the sample. The $\nu_1 + \nu_3$ band is still seen at 1872 cm^{-1}.

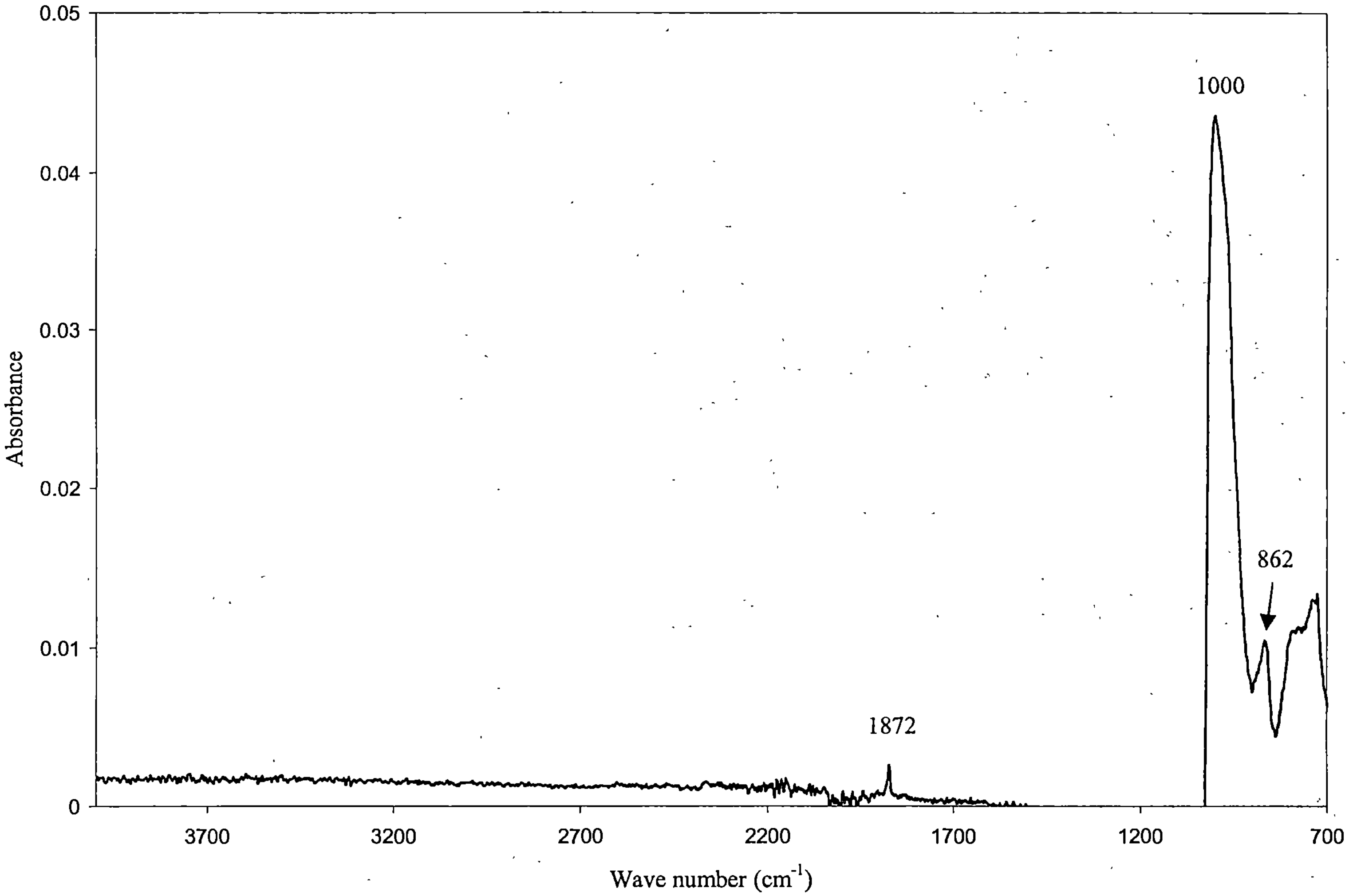

Fig. D.4. ATR spectrum for a sample of O_2-burned UO_2F_2.

VITA

Alan Scott Icenhour was born in Lenoir, North Carolina, where he graduated from Hibriten High School. He later graduated summa cum laude in May 1986 from North Carolina State University with a B.S. degree in nuclear engineering.

After his graduation from college, he next attended and graduated from Naval Officer Candidate School in Newport, Rhode Island, and was commissioned as an officer in the United States Navy. He then graduated from the Navy Nuclear Power School in Orlando, Florida; the D1G Nuclear Prototype in Balston Spa, New York; and Submarine Officer Basic School in New London, Connecticut. He reported on board USS Tecumseh (SSBN-628) in April 1988, where he served as a division officer and qualified in submarine warfare, while performing five strategic deterrent patrols. He left active duty in December 1990, but he is still a drilling reservist. He currently holds the rank of Lieutenant Commander, and he is the Executive Officer of the Trident Refit Facility, Kings Bay reserve unit.

In December 1990, he joined Oak Ridge National Laboratory, where he works in the Chemical Technology Division. His research has included source-term modeling for performance assessments of ORNL radioactive waste disposal facilities, analysis of disposition options for the ^{233}U disposition program, and analysis of low-level radioactive waste data for the Integrated Data Base Program. His recent efforts have been directed at the development, testing, and design of a ^{233}U-conversion process for deployment in a remote-operated hot cell, and at studies on radiolytic reactions in radioactive wastes and other materials. He received an M.S. degree in nuclear engineering from The University of Tennessee, Knoxville, in May 1995. He married his wife Teresa in May 1986. They have two daughters, Melissa and Abby.